Engineering Journal

American Institute of Steel Construction

First Quarter 2011 Volume 48, No. 1

Analysis and Design of Steel Slit Panel Frames (SSPFs) for Seismic Areas

GUSTAVO CORTES and JUDY LIU

ABSTRACT

The steel slit panel frame (SSPF) system is a new seismic force-resisting system (SFRS) intended for areas of high seismicity. The main components in an SSPF are steel beams and columns and steel slit panels (SSPs). SSPs are steel plates with rows of vertical slits cut at equidistant spaces. Links (small columns) are formed between the slits. When the panel is subjected to shear load, these links behave as beams in double curvature, reaching their plastic moment capacity at both ends. Beams are simply connected to the columns in the SSPF. The SSPs provide all the stiffness, strength and energy dissipation in the system. This paper presents the design of the SSP and the SSPF system. This paper also presents two prototype buildings that were designed for a site in Los Angeles, California. Finally, a simplified model developed for analyzing SSPs is presented.

Keywords: steel slit panels, seismic force-resisting system.

The steel slit panel frame (SSPF) system is a seismic force-resisting system (SFRS) intended for areas of high seismicity. The frame is composed of beams and columns, simply connected, and steel slit panels (SSPs) bolted between beams. An SSP is a steel plate with rows of slits cut from the plate so that small vertical flexural members, termed *links,* are created within the steel plate. When an SSP is subjected to shear deformations, the links behave as beams in double curvature, developing their plastic moment capacity at both ends and dissipating energy. Two edge stiffeners are welded to the main plate. These provide out-of-plane stability to the panel. Figure 1 shows a diagram of an SSP, highlighting its main attributes (e.g., the edge stiffeners, band zones, links and slits). The main parameters used for describing a panel are also shown in the figure. The configuration of the SSP is such that the system offers architectural flexibility (i.e., it can be placed within walls and around doors, windows and corridors) and offers retrofit possibilities.

This paper provides guidelines for the analysis and design of the SSPF system and includes prototype building design examples and a simplified model that may be used for analyzing the SSPs. These guidelines were created based on finite element analyses (FEAs) and experiments performed on the SSPs and on the SSPF (Cortes, 2009), as well as strength and stiffness equations developed for steel slit walls (Hitaka and Matsui, 2003) and adapted for the SSP (McCloskey, 2006; Cortes, 2009). In addition to the extensive parametric studies performed analytically, ten ⅓-scale tests were performed. These tests were divided in two series: the "panel-alone" series and the "panel frame" series. The first series of testing looked into the strength, the stiffness, the strain distributions and the failure modes of the panels. The second series of tests, the panel frame series, was intended to study the interaction of the panels with the frame. The equations for strength and stiffness were verified against the experimental data. Finite element analysis results suggested that the results from the ⅓-scale tests could be extrapolated to the full-sized panels (Cortes, 2009).

Ductile behavior is observed in the panels, with yielding in the links dominating the response to large drift levels. Figure 2 shows the load versus interstory drift plot for one of the panels tested, up to 4% drift (left) and until failure, at 7% drift (right). Global lateral-torsional buckling (LTB) occurred at the last cycle of 4% drift. LTB did not reduce the load carrying capacity of the panel. The strength degradation observed in Figure 2 was caused by cracks formed at the ends of the slits. At 3% drift, the upper and lower rows of links developed small cracks at the slit ends. At 7% drift the cracks had propagated enough to cause fracture of the links at the bottom in the lowest row. Tests of SSPFs (i.e., frames with SSPs) showed similar, ductile response; all panels were capable of reaching interstory drifts of at least 5% before failure.

Gustavo Cortes, Ph.D., P.E., post-doctorate researcher, Steel Structures Laboratory, Swiss Federal Institute of Technology, Lausanne, Switzerland. E-mail: gustavo.cortes@epfl.ch

Judy Liu, Ph.D., Associate Professor, School of Civil Engineering, Purdue University, West Lafayette, IN (corresponding author). E-mail: jliu@purdue.edu

DESIGN PROCESS

The design of an SSPF system requires two principal steps: (1) design of the steel slit panels (SSPs) to be used and (2) design of the steel slit panel frame (SSPF). The main equations and parameters for designing an SSP are provided in the next section. It is recommended that the engineer design a few different panels with different strength and stiffness capacities. This will provide different alternatives when designing the frame. In an SSPF, all beams and columns should remain elastic; inelastic deformation and any resulting damage should only occur at the panels (SSPs), which are intended to be easily replaceable. Beams are connected to the columns using simple shear connections (e.g., shear tabs, angles, etc.). Figure 3 shows a three-story SSPF with two panels at the exterior bays of each story.

Once the number of panels required to resist the design story shears in the frame is known, the frame should be analyzed and interstory drift checked. Interstory drifts that satisfy code requirements may be the final check, or the designer may further conduct a performance evaluation of the building according to ASCE 41 (2006); note that this study was conducted with the then-available pre-standard, FEMA 356 (2000). The last step is to design the bolted connections used to connect the panels to the beams and to the foundation. Design of an SSP, design of an SSPF, connection design, prototype building design and modeling using a simplified model are presented in the following sections.

STEEL SLIT PANEL DESIGN

The design of a steel slit panel includes choosing a configuration (i.e., link and edge stiffener dimensions) for which the links should develop their plastic moment capacity before any instability. Stiffness and strength can then be determined using equations based on mechanics principles. The first step is to determine the panel's overall geometry (e.g., its height, width and thickness). Because the panels are placed between beams, the height is obtained from the clear distance between beams. Part 9 of the AISC *Steel Construction Manual* (AISC, 2005d) recommends a clear distance of ½ in. between connecting members; thus, the total height of the panel, h, is the clear space between beams at the story where the panel will be placed, minus 1 in. (½ in. at each connection). The width of the panel, B, should be chosen to be near one-half of the panel's height to satisfy the 1:2 width-to-height ratio that characterizes the SSP system. As an initial estimate, ½-in. panels might be considered for buildings with three or fewer stories, or ¾ in. for taller buildings, up to ten stories. The thickness suggestion is based on FEA performed on buildings of one, three, six and ten stories located at a site in Los Angeles. Note that the SSPF system has only been studied for low- to mid-rise buildings with ten stories or less.

Once the global geometry of the panel has been defined, the next step is to define the geometry of the links and their pattern. Two or three rows of links should be used. The

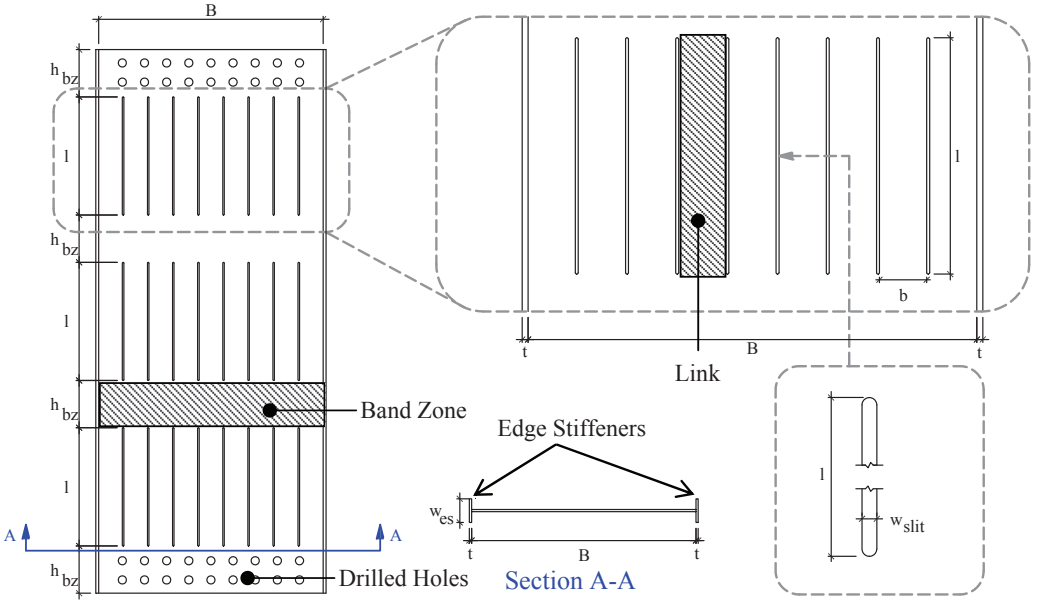

Fig. 1. Steel slit panel.

number of links, n, used in each row should be at least seven (McCloskey, 2006). The width of the slits will depend on the method used to make the cuts (e.g., plasma torch, water cutting, saw, etc.). If no information is known at the initial design, the designer may assume that for a ⅜-in.-thick panel, the width of the slit, w_{slit}, will be ⅛ in., for a ½-in.-thick plate the width will be 3/16 in., and for a ¾-in.-thick plate, the width will be ¼ in. These dimensions were observed in samples of steel where the slits were made using a plasma torch (McCloskey, 2006). The width of a link, b, may be determined from Equation 1.

$$b = \frac{B-(n-1)(w_{slit})}{n} \quad (1)$$

where

B = width of the panel (not including the edge stiffeners)
n = number of links
w_{slit} = width of the slits

There are three main parameters that need to be considered when designing an SSP: α, β and b/t. Typical values for these parameters were based on experimental observations on slit walls studied in Japan (Hitaka and Matsui, 2003). The slit walls are similar to the SSP but have an aspect ratio of 1:1 instead of 1:2 and are relied upon to resist only 25 to 30% of the lateral load in the system. Note that by 2003, three buildings, the tallest at 19 stories, had been built in Japan using a steel slit wall–moment frame dual system. Here, α is the link's aspect ratio given by l/b, where l is the length of the link. In addition, α ensures that a link is long enough so that flexure controls, rather than shear; α should be between 2.5 and 5.0. Defined as the fraction of the total height of the panel that is composed of links, β can be calculated as ml/h, where m is the number of rows. The recommended range for β is 0.65 to 0.85. This parameter ensures that the behavior of the panel is controlled by the links. The third parameter that needs to be checked is the width to thickness ratio of the link (b/t). This parameter controls premature out-of-plane deformations of the links. The recommended range for b/t is 10 to 15.

One pair of edge stiffeners is welded to the panel, one on each vertical edge. The two main purposes of the edge

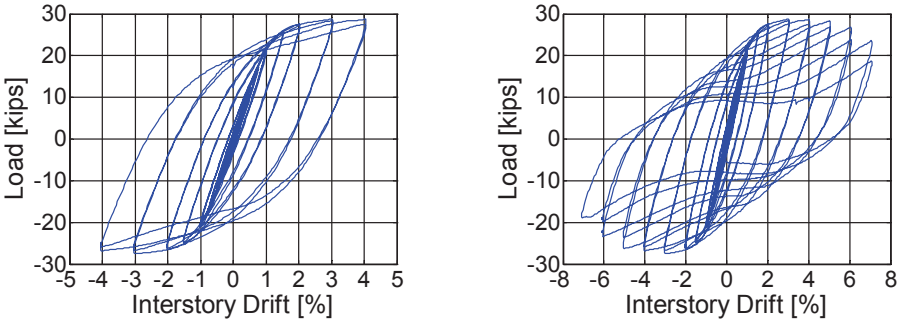

Fig. 2. Load vs. interstory drift plots; up to 4% (left); until failure at 7% (right) (Cortes, 2009).

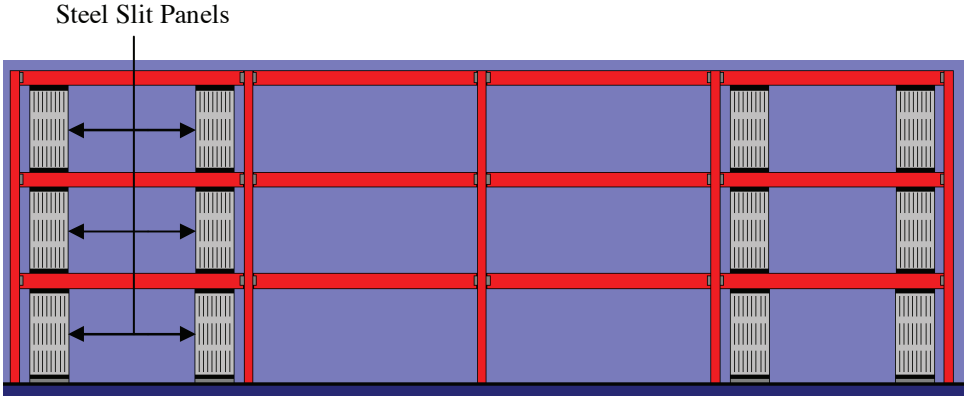

Fig. 3. Steel slit panel frame elevation.

stiffeners are (1) resisting the overturning moments and (2) providing resistance to out-of-plane deformations and buckling in the SSP. In addition to these main purposes, the edge stiffeners increase the lateral stiffness and the ultimate strength of the steel slit panel. The edge stiffeners are designed to take all of the overturning moment in the panel. The overturning moment is divided into two coupling forces, or boundary forces, which are determined from force diagrams based on the mechanics of the panel (see Figure 4). The boundary force, P_{bound}, is given by Equation 2.

$$P_{bound} = \frac{Q_{ult}\left(\frac{h}{2}\right) - nM_p}{B} \quad (2)$$

where

Q_{ult} = shear capacity of the panel, assuming full plastic moment capacity of the links (Equation 6 or 7)

M_p = plastic moment capacity of the link

The width of the edge stiffeners, w_{es}, is calculated from the assumption that the edge stiffeners undergo axial yielding when subjected to P_{bound}. It is practical to use edge stiffeners with a thickness equal to that used for the panel. If necessary (e.g., to increase the moment of inertia of the panel or the stiffness), the plate used for the edge stiffeners may be thicker; however, the equations given in this paper assume that the main plate and the edge stiffeners are made from the same plate thickness. Experimental tests have shown that the edge stiffeners undergo yielding at top and bottom. This yielding was caused by the high local bending demand caused by the lateral deformations of the panel rather than by the axial load demand. However, the same experiments demonstrated that sizing the edge stiffeners assuming compressive yielding resulted in an appropriate design. The edge stiffeners were capable of resisting the boundary element forces and prevented the panel from undergoing out-of-plane deformations until larger drift levels. The width of the edge stiffeners is calculated from Equation 3.

$$w_{es} = \frac{P_{bound}}{F_y t} \quad (3)$$

where

F_y = minimum specified yield strength of the panel

Once the edge stiffeners are sized, local buckling shall be checked (AISC, 2005a). Also, the width of the edge stiffeners should not interfere with partition walls or other nonstructural components of the building. The edge stiffeners are connected to the main plate using welds. Because the panel acts as a flexural member in double curvature, the design load at the edge stiffener (P_{bound}) acts on half the length (only half of the length is in compression at each stiffener). In other words, the length used for design of the weld should be $h/2$. The welding procedure should be carefully planned such that initial imperfections in the panels due to the heating-cooling process are minimized. Initial imperfections are not desired because these reduce the out-of-plane resistance of the panel. This was observed in most of the ⅓-scale panels tested. It is expected that for full-scale panels, the effect will not be as important as it was for the smaller ⅓-scale

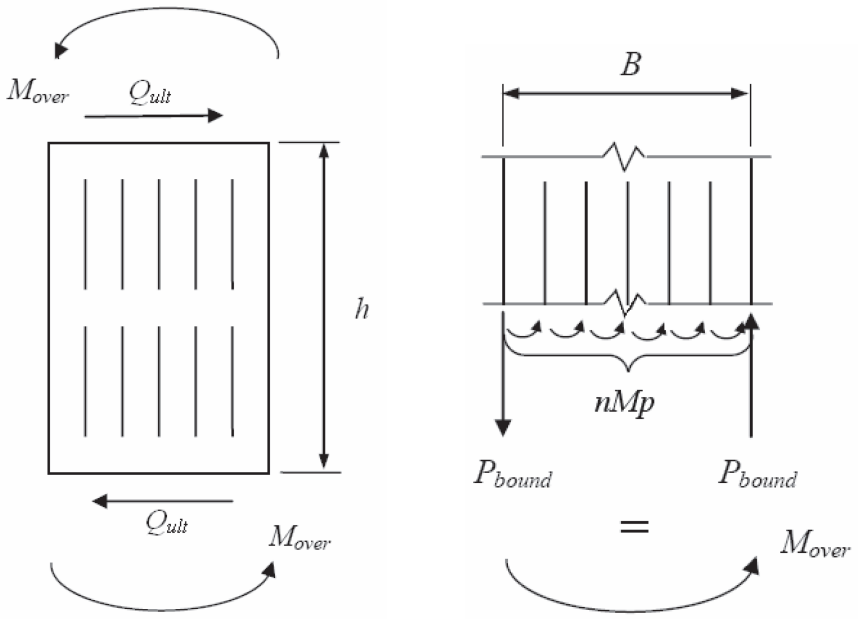

Fig. 4. SSP force equilibrium diagram (adapted from McCloskey, 2006).

specimens, because the panel thickness is greater. Nevertheless, caution is advised.

The stiffness of an SSP is determined from the contributions of the band zones (regions above, below, and between the links) and the links. Three terms are considered: (1) the shear stiffness of the band zones, (2) the shear stiffness of the links and (3) the flexural stiffness of the links. The equation, developed by Hitaka and Matsui (2003), is shown here:

$$K_{panel} = \frac{1}{\frac{k(h-ml)}{GBt} + \left(\frac{m}{n}\right)\left(\frac{kl}{Gbt}\right) + k(\alpha)\left(\frac{m}{n}\right)\left(\frac{l^3}{Etb^3}\right)} \quad (4)$$

where

k = shear deformation shape factor (1.2 for rectangular sections)
G = shear modulus
E = Young's modulus
$k(\alpha)$ = factor that considers the level of restraint of the links (given by Equation 5)

and other parameters are as previously defined.

$$k(\alpha) = \left(1+\alpha^{-1}\right)^3 \quad (5)$$

Here, $k(\alpha)$ was determined from experimental results (Hitaka and Matsui, 2003). Equation 4 assumes that the stiffness provided by one link is $12EI/l^3$, where I is the moment of inertia of the link; however, the stress concentrations around the slits reduce the level of restraint provided to the links. The $k(\alpha)$ factor reduces the stiffness provided by the links from $12EI/l^3$ to a value ranging from $4.4EI/l^3$ to $6.9EI/l^3$, depending on α; $4.4EI/l^3$ corresponds to an α of 2.5 (lower limit of α); $6.9EI/l^3$corresponds to an α of 5.0 (upper limit of α).

The ultimate strength of an SSP is obtained from the case when all the links in a row reach their plastic moment capacity. The equation is determined by adding the shear forces developed in the interior links and the shear forces developed in the two exterior links in a row. The two exterior links are treated differently than the interior links because these work together with the edge stiffeners to form a T-shaped link. As such, the equation for strength will depend on the location of the plastic neutral axis of these links. Two cases are possible: (1) when the plastic neutral axis occurs in the edge stiffener and (2) when the plastic neutral axis occurs in the link. Assuming that the thickness of the edge stiffeners and the panel is the same, one may determine the applicable case by comparing the width of the edge stiffener (w_{es}) to the width of the link (b). If w_{es} is greater than b, the plastic neutral axis will be inside the edge stiffener; otherwise, the plastic neutral axis will be in the link. Equation 6 is used for the first case ($w_{es} > b$); Equation 7 is used for the second case ($w_{es} \le b$). If $w_{es} = b$, both equations will provide the same result.

$$Q_{ult} = \frac{F_y t}{2l}\left[\left(b^2 n\right) + 2b^2\left(t-1\right) + 2w_{es}\left(2b+t\right)\right]$$
(for $w_{es} > b$) (6)

$$Q_{ult} = \frac{F_y t}{2l}\left[\left(b^2 n\right) + 4bw_{es} + 2w_{es}^2\right]$$
(for $w_{es} \le b$) (7)

Ideally, the panel should be designed to reach its ultimate strength (e.g., plastic moment capacity of all links in a row reached); however, other failure modes may control the design of the SSP. Because the SSP has an aspect ratio of 1:2, the parameters developed by Hitaka and Matsui (2003) for the 1:1 slit walls are not sufficient for preventing instabilities, particularly global instabilities. Three strength limit states should be checked: (1) global lateral-torsional buckling, (2) lateral-torsional buckling of all links in a row and (3) shear buckling of the panel. Global lateral-torsional buckling of the panel causes the panel to twist and, therefore, to behave in a different way than intended. At low drift levels, the edge stiffeners help the panel stay in plane; however, at higher drift levels, out-of-plane deformations will certainly occur. Global lateral-torsional buckling should be delayed to interstory drifts of at least 2 to 2.5%, corresponding to the drift limit for a design-basis earthquake (ASCE, 2005). Figure 5 shows an SSP undergoing global lateral-torsional buckling.

Fig. 5. Global lateral-torsional buckling of an SSP.

Equation 8 provides a prediction of the capacity associated with global lateral-torsional buckling. This equation was developed by Timoshenko and Gere (1961) for determining the lateral-torsional buckling capacity of a cantilevered beam with a narrow cross section loaded at the free end. Half of the height of the panel (more precisely, the distance from the centroid of the group of bolts to mid-height of the panel) is used for the length of the cantilever beam ($h_{LTB}/2$). This equation provided predictions within 6%, on average, compared to experimental results from SSPs tested that underwent LTB (Cortes, 2009).

$$Q_{LTB} = \left[\frac{4.013}{\left(\frac{h_{LTB}}{2}\right)^2}\right]\sqrt{EI_{panel}C} \tag{8}$$

where

I_{panel} = moment of inertia of the panel about its weak axis, neglecting the slits (assuming solid panel), including the edge stiffeners (i.e., $B + t$)
C = torsional constant (given by Equation 9)
h_{LTB} = height used for this calculation, shown in Figure 6.

$$C = \left(\frac{Gt^3}{3}\right)(2w_{es} + B - 2t) \tag{9}$$

In addition to global lateral-torsional buckling, lateral-torsional buckling of the links in a row should be checked. This limit state did not control any of the panels studied; however, it was observed in studies of the steel wall with slits performed in Japan (Hitaka and Matsui, 2003). To determine the capacity of the panel associated with lateral-torsional buckling of the links, the capacity of one link is determined based on Timoshenko and Gere (1961) and then multiplied by the number of links in a row, n. The final equation for capacity associated with lateral-torsional buckling of the links is given by Equation 10.

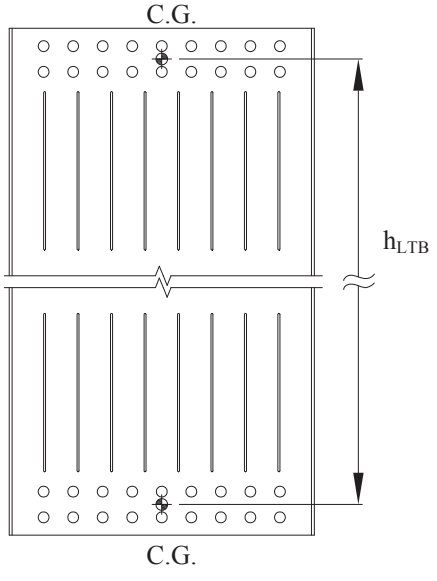

Fig. 6. Height used for calculating the global lateral-torsional buckling capacity.

$$Q_{LTB\ links} = n\left[\frac{4.013}{\left(\frac{l}{2}\right)^2}\right]\sqrt{EI_{link}c_{link}} \tag{10}$$

where

I_{link} = moment of inertia of the link about its weak axis ($bt^3/12$)
c_{link} = torsional constant given by Equation 11

$$c_{link} = GJ = \left(\frac{Gbt^3}{3}\right)\left[1 - 0.63\left(\frac{t}{b}\right)\right] \tag{11}$$

The last limit state that needs to be checked is shear buckling of the panel. The slits in the panel create a rather complex geometry; however, for the purpose of determining capacity, the panel is treated as a solid panel. Equation 12 is used for determining the shear buckling capacity of the panel.

$$Q_{scr} = k_v \frac{\pi^2 E}{12\left(1 - \nu^2\right)}\left(\frac{t^3}{B}\right) \tag{12}$$

where

ν = Poisson's ratio (taken as 0.3 for steel)
k_v = parameter that depends on the edge support conditions, the type of stress and the aspect ratio of the plate

Equation 12 is an equation developed by Timoshenko and Gere (1961) to obtain the elastic buckling unit stress in a plate, multiplied by the cross-sectional area of the panel (Bt) to obtain the result in strength units. For simplicity, the area of the edge stiffeners is neglected for this calculation.

Timoshenko and Gere (1961) provided the k_v values for different boundary conditions and aspect ratios of the plate. It is recommended to assume simply supported boundary conditions (McCloskey, 2006) for which k_v is approximated by Equation 13.

$$k_v = 5.34 + 4.0\left(\frac{B}{h}\right)^2 \tag{13}$$

The capacity of an SSP is given by Equation 6 or 7, which should be less than the minimum of the three other possible limit states discussed earlier. This is shown in Equation 14.

$$Q_{panel} = Q_{ult} (< Q_{GLTB}, Q_{LTB\ links}, Q_{scr}) \quad (14)$$

Equation 14 is used to enforce ductile and stable behavior of an SSP; Q_{panel} should be equal to Q_{ult}. This ensures that the SSP is able to reach its ultimate strength (Q_{ult}) without any other limit state occurring, which is when all the links are able to develop their plastic moment capacity at both ends. For all panels studied experimentally (Cortes, 2009), with the exception of the 3⁄16-in. panels, the Q_{ult} was the controlling limit state. For the 3⁄16-in. panels, the equation for global lateral-torsional buckling (Equation 8) controlled over the Q_{ult} equation, but Q_{GLTB} was about 91% of Q_{ult}. Even though the LTB limit state controlled for these panels, they still exhibited stable loops and no strength degradation until at least 4% interstory drift.

The preferred material for plates is the ASTM A36 (AISC, 2005b), with a minimum specified yield stress of 36 ksi. Although A572 steel may also be used for plates, it might be better to use A36, because the links should develop their plastic moment capacity before other instabilities occur. Steel with a higher yield capacity will increase the ultimate strength of the panel (Q_{ult}), but the capacity of the panel may now be controlled by the other limit states, which do not depend on the yield strength. Figure 7 shows a

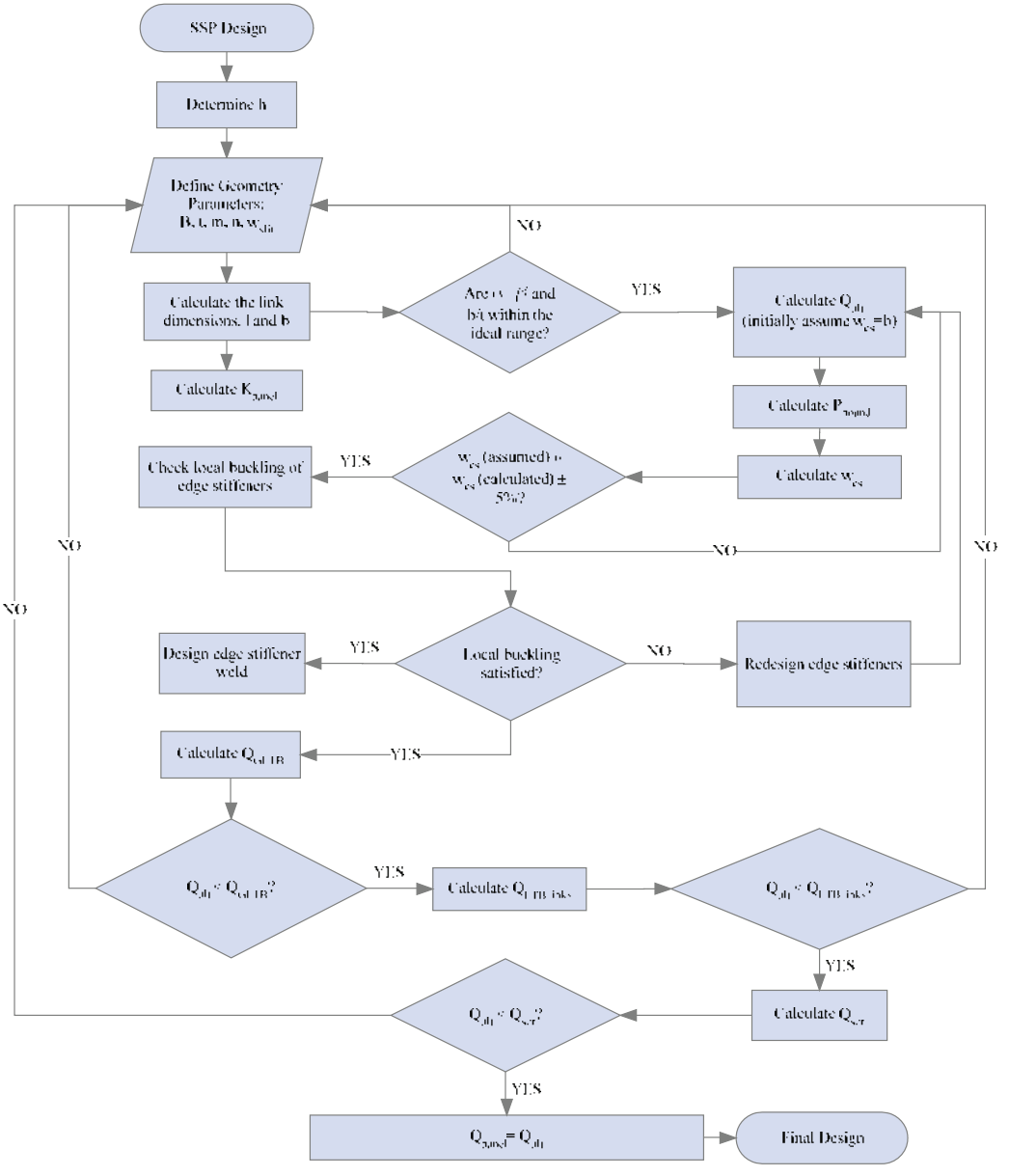

Fig. 7. SSP design flowchart.

flowchart that summarizes the steps required for the design of a steel slit panel.

STEEL SLIT PANEL FRAME

A steel slit panel frame (SSPF) is a frame that uses SSPs to resist the base shear and to provide the required stiffness. The SSPs are connected to the beams, using moment resisting connections (see Figure 14). In an SSPF, beams are pin connected to the columns and columns are pin connected to the foundation. An example of an SSPF is given in Figure 3. Design of an SSPF includes sizing of the frame elements (beams and columns) and determining the number of panels required for story shear demands and check of interstory drift limits, with consideration for the effects of the panel–frame interaction on the panel stiffness. Note that atypical load patterns develop in the beams when the frame is subjected to lateral loads. These loads, caused by the SSPs, need to be fully considered for the design of the beams.

One may determine the number of panels required by dividing the story shear by the capacity of the panel to be used (Equation 15).

$$\text{Number of panels}_{V_i} = \frac{V_i}{Q_{panel}} \tag{15}$$

where

V_i = story shear demand

Q_{panel} = capacity of the panel, determined from Equation 14

For determining the base shear demand, a response modification factor, R, of 5.5 is recommended. Once the SSPF has been designed for strength, the next step would be to verify that interstory drifts are within limits. When verifying drift limits using the linear elastic method, a C_d value of 4.5 should be considered. The R and C_d values were preliminarily established from engineering judgment, based on similar seismic systems, by the project oversight committee. This committee included practicing engineers, fabricators and researchers. While both the R and C_d correspond well to nonlinear analyses conducted as part of this study (Cortes, 2009), both should be verified following the FEMA P695 methodology (FEMA, 2009).

Because the SSPF system is relatively flexible, interstory drifts may dictate the number of panels required at each story. Thus, it may be more practical to initially estimate the number of panels required to satisfy interstory drift limits. The number of panels required to satisfy interstory drift limits may be obtained from Equation 16.

$$\text{Number of panels}_{Ki} = \frac{K_{ei}}{K_{eff}} \tag{16}$$

where

K_{ei} = elastic stiffness demand in story i (given by Equation 17)

K_{eff} = effective stiffness provided by the panels within the frame (from Equation 18)

$$K_{ei} = \left(\frac{C_d}{I}\right)\left(\frac{V_i}{\Delta_a}\right) \tag{17}$$

where

I = importance factor according to ASCE 7 (ASCE, 2005)

Δ_a = allowable displacement according to ASCE 7 (ASCE, 2005)

While the SSPs provide the stiffness in the frame, the

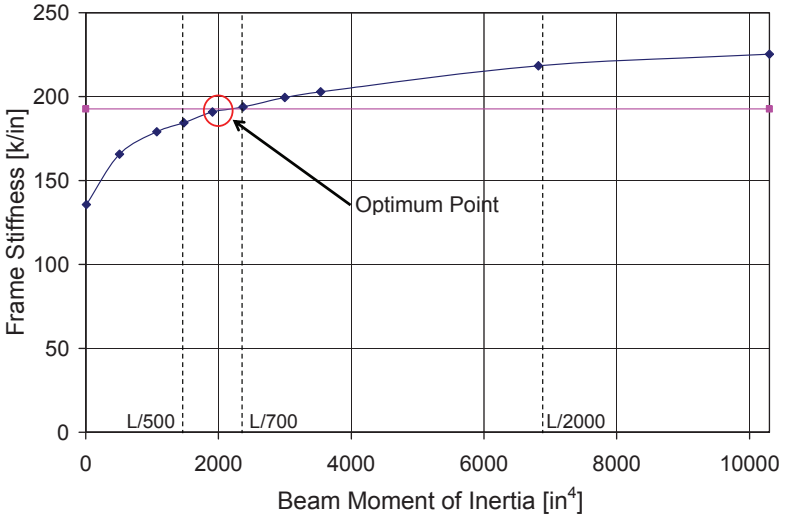

Fig. 8. Frame stiffness as a function of the beam's moment of inertia.

panel–frame interaction plays a major role in the stiffness provided by the SSPF. Here, K_{eff} is the panel stiffness as modified by the frame, and K_{panel} (Equation 4) estimates the stiffness of a panel subjected to relatively stiff boundary conditions. However, the actual boundary conditions provided by the beams depend on their flexural stiffness. Also, at stories above the first story, the rotation of the frame further reduces the stiffness provided by the panels. In addition, the number of bays in the SSPF plays a significant role in the effective stiffness provided by a panel. The effective stiffness provided by an SSP may be determined from Equation 18.

$$K_{eff} = [R_{bm} R_{Story}] R_{\#\,Bays} K_{panel} \quad (18)$$

Equation 18 considers the reduction in stiffness caused by the flexibility of the beam, R_{bm}, the story where the panel is placed, R_{story}, and the number of bays in the SSPF with panels, $R_{\#bays}$. These factors are multiplied by the stiffness of the panel, K_{panel} (Equation 4), to obtain the effective stiffness provided by the panel. The following paragraphs explain the factors used in Equation 18 (i.e., R_{bm}, R_{Story} and $R_{\#Bays}$).

The factor R_{bm} accounts for the flexibility of the beam in the frame. A beam with a low flexural stiffness will lower the effective stiffness provided by the panels it bounds. Meanwhile, a beam with a higher flexural stiffness will provide stiffer boundary conditions to the panels, and therefore, higher SSPF stiffness. Figure 8 shows a plot of frame stiffness for a one-story, one-bay frame, with column spacing equal to 30 ft, a story height of 13 ft, and a ½-in.-thick panel placed at the center of the bay and bounded by beams with different moments of inertia. Note that as the moment of inertia of the beam bounding the panel increases, the frame stiffness also increases. The horizontal line represents the stiffness predicted by Equation 4. The optimum point, also shown in the figure, represents the intersection of the stiffness predicted by Equation 4 and the actual stiffness obtained from the plot. For this frame, the optimum point was reached for beams that satisfy a deflection limit of nearly $L/700$ [deflection limit for a uniformly loaded simply supported beam, assuming no panel, subjected to service gravity loads ($D + L$)], where L is the beam span. Note that a beam should satisfy a deflection limit of $L/500$ to limit initial stresses due to gravity loading (McCloskey, 2006).

Finite element analysis (FEA) revealed that in frames with more than one story, the stiffness decreases as a function of the story in the building, decreasing from the bottom floor to the upper floor. This was confirmed by experimental results (Cortes, 2009). For example, Figure 9 shows the deflected shape of a three-story SSPF with a 30-ft bay and 13-ft stories. The story shear at the first story causes a rotation, θ_1. This initial rotation in the first story is passed to the second story. Thus, the total rotation at the second story is the rotation from the first story, θ_1, plus the rotation due to the shear demand on the second story, θ_2. This effect can be observed in Figure 10, which shows the story stiffness (normalized by K_{panel}) as a function of the beam's moment of inertia. The stiffness obtained by the first story is higher than that in the second story; the stiffness is further reduced at the third story. Note also that only the first story reached the optimum point; however, it requires a higher beam moment of inertia than the case with only one story. Figure 10 considers both the effect of the beam flexibility and the frame rotation.

In Equation 18, the reduction factor for the beam's flexural rigidity and the story where the panel is placed are inside of a bracket to indicate that these two factors may be obtained from one plot such as Figure 10 or Figure 11. Figure 11 shows a plot of the floor number versus story stiffness (panel stiffness, normalized by K_{panel}) for one-, two-, three-, four- and five-story frames. All frames studied had 30-ft bays, story heights of 13 ft, W24×84 beam sections, and ½-in. panels. In this plot, the abscissa represents the story stiffness and the ordinate represents the story number. The stiffness at the top floor of a frame having n number of stories is related to the stiffness at the top floor for a frame having $n - 1$ number of stories, $n - 2$, and so on. In other words, the stiffness of the upper story was compared for all frames. Then, the stiffness of the story below the upper story was compared for all frames, and so on. A similar pattern was observed for the stiffness in each of the floors, and a regression can be used to fit the values of all stories. The dashed line is a power regression used to fit all data points. The only floor where the average line has a large variation is at the first floor.

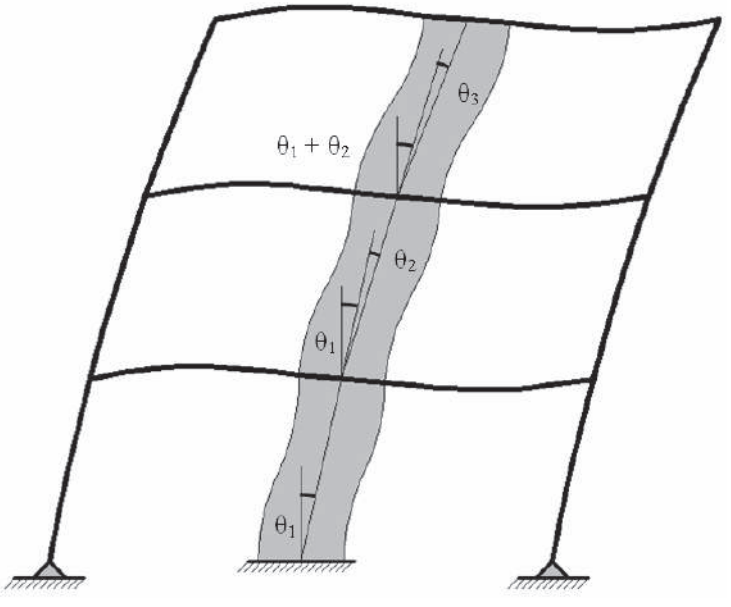

Fig. 9. Displaced shape of a three-story SSPF.

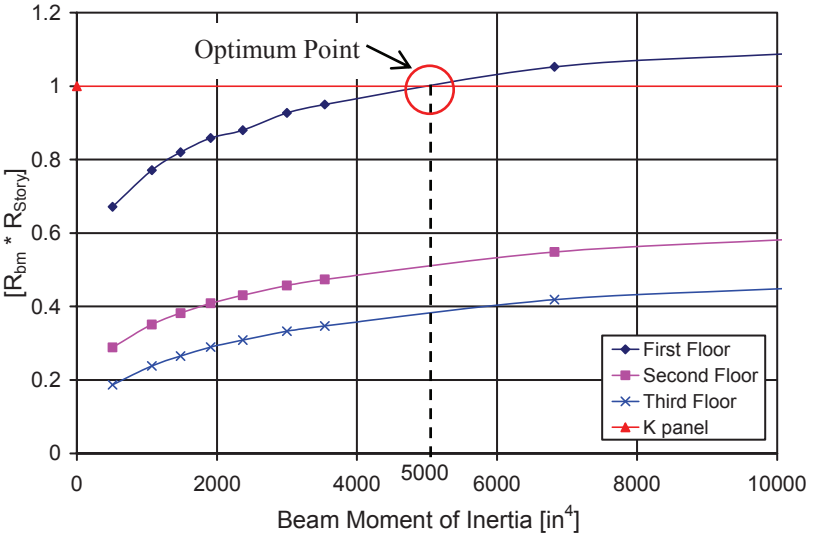

Fig. 10. Reduction caused by frame rotation for a three-story SSPF.

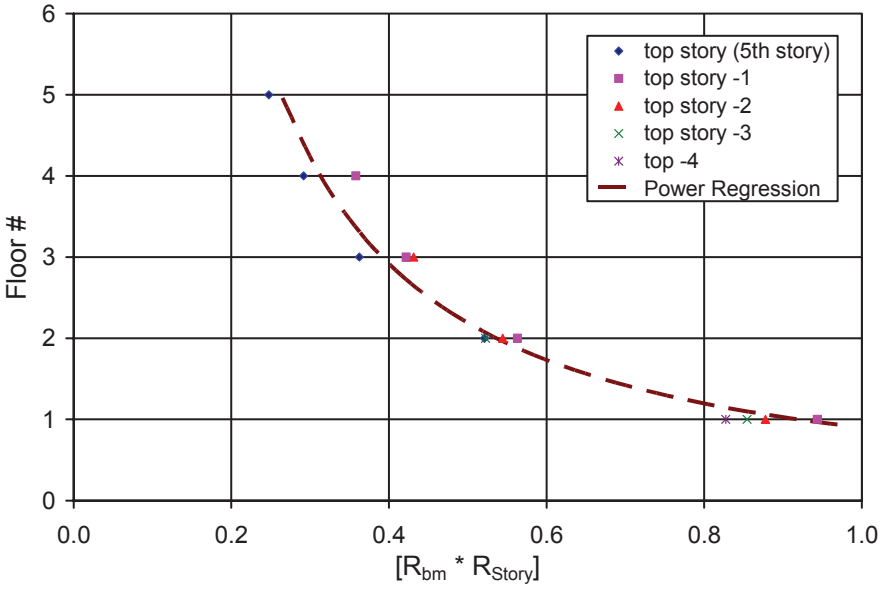

Fig. 11. Stiffness as a function of the floor number.

Nevertheless, this plot results in a very good approximation for estimating the reductions in stiffness caused by the beam flexibility and by the frame rotation.

The other main factor that affects the stiffness in a frame is the number of bays with panels in the SSPF. Parametric studies of the frame revealed that as more bays in an SSPF are filled with panels, the effective stiffness provided by the panels increases. For example, the effective stiffness provided by the panels in a frame with five bays with panels is higher than the effective stiffness of the panels in a frame with two bays with panels. Five 10-story frames with 30-ft-wide bays and two ¾-in. panels at each bay were studied. All beam sections were W24×117; columns were W14×90 at all stories. For these frames, all the properties were the same except for the number of bays. The number of bays with panels was varied from two to five. The results of this study are summarized in Figure 12. The abscissa in this plot represents the stiffness provided by each panel at each story, normalized by the panel stiffness (obtained from Equation 4). The floor number is given in the ordinate.

Note that as more bays are part of the SSPF, the effective stiffness for each panel increases. The stiffness at each panel in the tenth floor is about 20% higher for the five-bay frame compared with the two-bay frame. This increase in stiffness is caused by the additional columns in the seismic frame. The beams are pin connected to the columns; however, because the columns are continuous from the foundation to the top (assuming that the column splices provide continuity), those adjacent to bays with panels appear to provide additional shear stiffness and flexural stiffness.

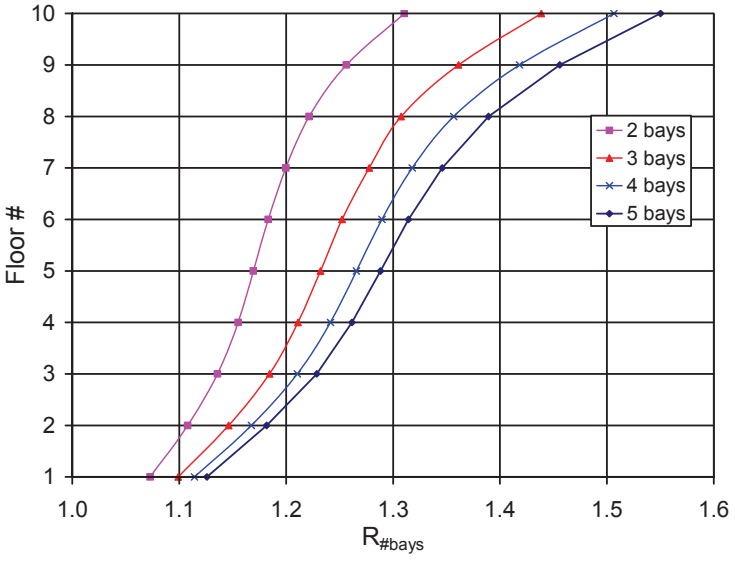

Fig. 12. Stiffness increase for more bays.

Determining the effective stiffness provided by a panel (K_{eff}) might be cumbersome initially because the analysis of many models is needed initially. However, Figures 10 and 11 may be used to approximate the number of panels required to satisfy stiffness. Figure 11 combines factors R_{bm} and R_{Story} into one. Figure 12 provides the $R_{\#bays}$ factor for certain

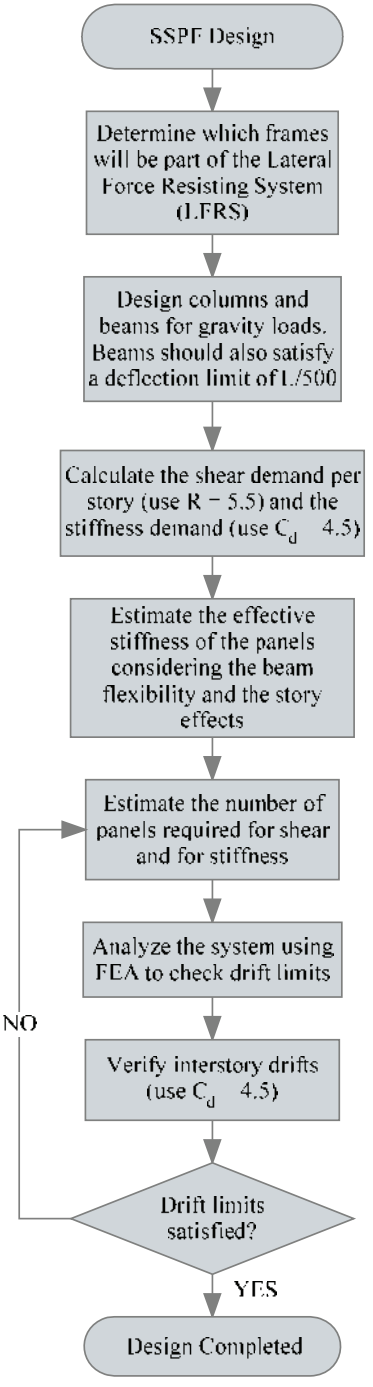

Fig. 13. SSPF design flowchart.

configurations. In an example shown in a later section, Figure 11 alone was used to estimate the required number of panels to satisfy drift limitations. Although these two plots were developed for one specific frame and panel geometry, they may be used to obtain an initial estimate.

Figure 13 shows a flowchart that summarizes the main steps for designing an SSPF.

STEEL SLIT PANEL–BEAM CONNECTION

SSPs are connected to the beams using fin plates. The fin plates are shop welded to the beams and bolted to the SSPs. These connections must be able to transfer the shear force and the moment generated by the panel. Slip of the connection is undesirable at service loads (dead, live and wind loads). Thus, high-strength structural bolts pretensioned on faying surfaces as specified by AISC 341 (AISC, 2005c) should be used. The design load for the connection (i.e., fin plate to beam and fin plate to SSP) is the ultimate capacity of the panel multiplied by 1.3. This factor accounts for the possibility of the yield strength of the panel being higher than the minimum specified yield strength and is the recommended R_y value for A36 steel used for plates (AISC, 2005c).

Bolt slip, shear and bearing capacity must be considered for both shear and overturning moment ($1.3Q_{ult}\ h/2$) demands. Moment capacity and shear capacity of the fin plate (i.e., shear yield, shear rupture, block shear rupture) must also be considered. The design load and moment should also be used to design the weld that connects the beam to the fin plate.

The connection must provide a uniform level of restraint to all the links. Special attention must be paid to the two exterior links. The bolts must extend to cover the exterior links. Figure 14 shows two connection details; the left detail is not recommended because experimental results have

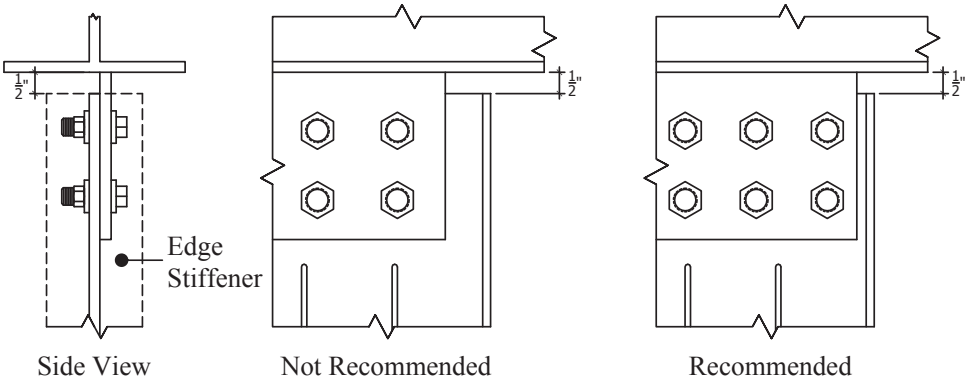

Fig. 14. Connection detail.

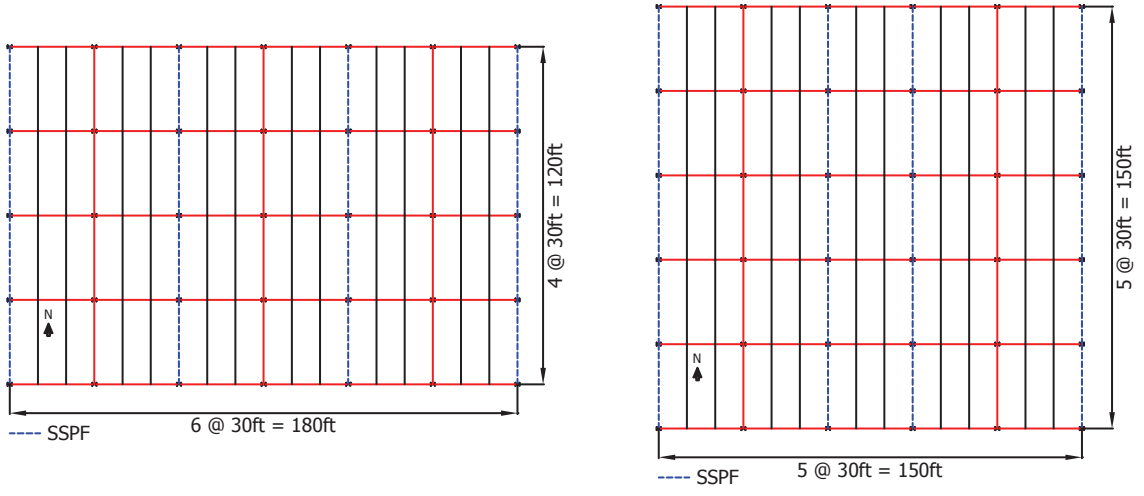

Fig. 15. Plan view of the three-story prototype building (left) and ten-story prototype building (right).

Table 1. T1 Panel Properties									
m	***n***	***B*** (in.)	***H*** (in.)	***T*** (in.)	***l*** (in.)	***b*** (in.)	α	β	***b/t***
3	9	59.375	130	0.5 or 0.75	32	6.375	4.9	0.72	12.8

Table 2. Required Strength and Stiffness		
Story	**V_i (kips)**	**K_{ei} (kip/in.)**
1	509	587
2	428	494
3	266	307

Table 3. Required Number Panels for Strength					
Floor	**Force (kips)**	**Panel Thickness (in.)**			
	V_i	⅜	½	⅝	¾
1	509	4.9	3.7	2.9	2.4
2	428	4.1	3.1	2.5	2.0
3	266	2.6	1.9	1.5	1.3

shown that it will not provide enough restraint to the exterior links. The detail shown on the right is expected to provide a more uniform restraint to all the links. The exterior links will not be able to reach their ultimate strength if they are not well restrained. The stiffness of the panel may also be affected.

Other types of connections may be used (e.g., single-angle connections). However, all tests to date were performed for panels connected using fin plates. Thus, testing other connections prior to their use is recommended.

PROTOTYPE BUILDING DESIGN

This section presents an overview of the design of two prototype buildings using SSPFs as their SFRS. The two prototype buildings were designed according to ASCE 7 (ASCE, 2005) for a site in Los Angeles, California. Both buildings were designed based on seismic weights of 125 psf at the roof and 114 psf at intermediate levels (Richards and Uang, 2003). These weights include dead load and 25% of the live load. The first prototype building is a three-story building with a rectangular plan. It has four bays in one direction and six in the orthogonal direction. All bays are 30 ft wide. The second prototype building is a ten-story building with a square plan and five 30-ft bays in each direction. For both buildings, the floor to-floor height of all stories is 13 ft. Figure 15 shows the plan views of both prototype buildings. The dashed lines indicate the bays where panels are placed. For the three-story building, ½-in. Type 1 (T1) panels (Cortes, 2009) were used. For the ten-story building, ¾-in. T1 panels were used. The main dimensions and parameters for the ½-in. and ¾-in. T1 panels are presented in Table 1.

The following paragraphs present the design process for the three-story building; for the ten-story building, only the results are presented. Following the design flowchart shown in Figure 13, the SSPFs were identified; these are indicated in Figure 15 with the dashed lines. Beams and columns were designed for gravity loads; beams also satisfied a deflection limit of $L/500$. The deflection limit was checked for a simply supported beam subjected to service dead and live loads ($D + L$), assuming a 50-psf live load for office buildings (ASCE, 2005). The moment of inertia required to satisfy the $L/500$ limit is 1912 in.^{4} (assuming a tributary width of 15 ft). W24×84 beams (2,370 in.^{4}) were provided. W14×90 sections were used for the columns. Lateral demands were also calculated following ASCE 7 (ASCE, 2005). Table 2 shows the required shear strength and lateral stiffness (Equation 17) per story. The importance factor (I) was taken as 1. Table 3 shows a summary of the required number of T1 panels with thicknesses of ⅜, ½, ⅝ and ¾ in. to resist story shears. The capacities of these panels were calculated with Equation 14. The next step would be to estimate the number of panels required to satisfy drift limits. Given the complexity of the panel-frame interaction and its effect on stiffness, one should then verify drift levels with a finite element model. All attributes of the panel (i.e., links, slits, edge stiffeners) should be included in the finite element model. Shell elements shall be used to model the panel. As an alternative to using shell elements, a simplified model of the SSP is presented in the next section. Table 4 shows the stiffness demand, K_{ei}, the reduction factor, $[R_{bm} \times R_{Story}]$, the effective

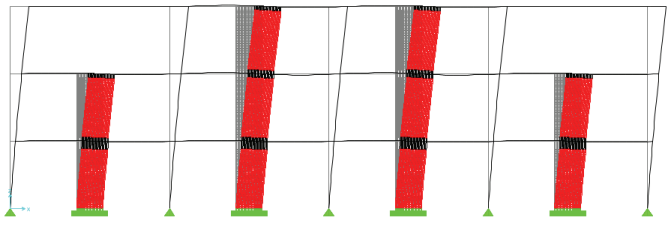

Fig. 16. Three-story building, second configuration.

Table 4. Required Number of Panels for Stiffness (½-in. panels)				
Floor	K_{ei} (kip/in.)	$[R_{bm} \times R_{Story}]$	$K_{eff} = K_{panel}[R_{bm} \times R_{Story}]$ (kip/in.)	Number of Panels
1	587	0.92	175	3.4
2	494	0.54	103	4.8
3	307	0.4	76	4.0

Table 5. Interstory Drifts for Configuration 1				
Floor	δ_{xe} (in.)	Δ (in.)	Δ_a (in.)	$\Delta < \Delta_a$
1	0.6	2.7	3.9	True
2	1.3	3.3	3.9	True
3	2.0	2.8	3.9	True

Table 6. Interstory Drifts for Configuration 2				
Floor	Deflection	Δ (in.)	Δ_a (in.)	$\Delta < \Delta_a$
1	0.65	2.92	3.90	True
2	1.47	3.69	3.90	True
3	2.44	4.37	3.90	False

stiffness of the panel, K_{eff}, and the number of ½-in. panels required to satisfy drift limits. The reduction factor was obtained from Figure 11, which only considers the flexibility of the beams and the story effects. In other words, the $R_{\#bays}$ was taken as 1. This is a conservative assumption because this value is always higher than 1. This should yield a reasonable approximation; furthermore, interstory drift values will be checked using finite element analysis. Observe that drift requirements control the required number of panels for the second and third story; the number of panels required in the first story is controlled by the shear demand. A few steel slit panel frame configurations with panels located in different locations were studied; two are discussed next.

The first configuration studied is shown in Figure 15. Four panels were used at all three stories. The finite element software SAP2000 was used to analyze the frame. Frame elements were used to model the beams and columns, and shell elements were used to model the panels (Cortes, 2009). The models of the panels included the edge stiffeners and the slits. The panels were connected to the beams using rigid links. The interstory drifts obtained for this configuration are shown in Table 5. This table shows the interstory drifts obtained from the elastic analysis (δ_{xe}); the drift values (Δ), which are amplified by C_d to account for the nonlinear effects; and the allowable interstory drift (Δ_a). The allowable drift is 3.9 inches, which corresponds to a 2.5% interstory drift. All stories satisfied interstory drift limits for this configuration.

The second configuration has four panels in the first and second stories and two panels in the upper story. All panels were located at the center of the bay. Figure 16 shows a deformed shape of the second configuration. Table 6 shows a summary of the drift values obtained for the three stories. Note that the third story did not satisfy drift limits. One could add more panels in this story or use thicker panels or use beams with a higher moment of inertia. For this example, the simplest solution would be to use beam sections with a higher moment of inertia. If W24×103 beams are used, all three stories satisfy interstory drift limits.

A similar procedure was performed for the ten-story prototype building. Two ¾-in. T1 panels were used at each bay. The SSPF used for the ten-story building is shown in Figure 17. Figure 17 also shows the interstory drift values obtained from the elastic analysis and amplified by C_d. Note that the interstory drift limit of 2% (ASCE, 2005) is satisfied for all stories.

SSP SIMPLIFIED MODEL

An SSP can be modeled in FEA software using shell elements. Its geometry needs to include the slits—and thus the links—and the edge stiffeners. Figure 18 shows a panel

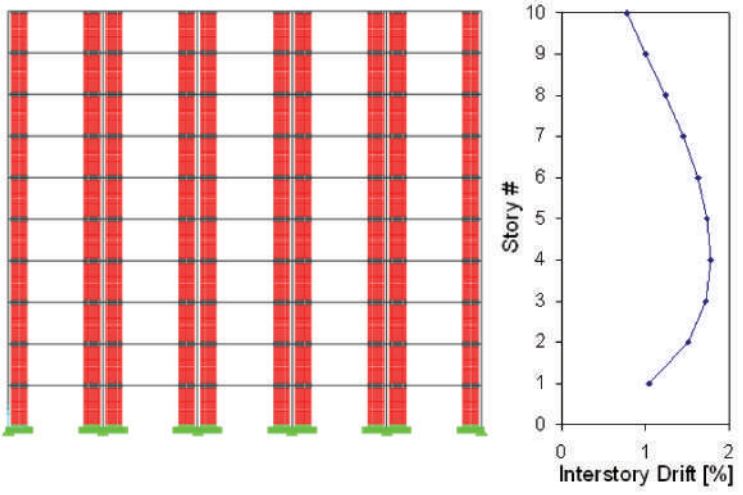

Fig. 17. Ten-story frame used in prototype building.

modeled in the FEA software SAP2000. While the most proper way of modeling the panels is using shell elements, there are reasons a simplified model may be needed. The first reason for a simplified model is that some FEA software may not have the capacity to model shell elements. Even if the software has the capacity to model the panels using shell elements, these may be limited to the elastic range. While most analyses for design are performed in the elastic range, more advanced analyses require the consideration of the material plasticity. This is especially true for the SSPs, which undergo much yielding at the link ends. The simplified model presented next is capable of capturing yielding at the links. The second reason for a simplified model is that it is simpler to model and thus is less computationally expensive than a model using shell elements.

The simplified model uses frame elements to model the SSP. The frame elements have cross sections equivalent to the actual dimensions of the links and the band zones. For the external links, the edge stiffener is modeled together, creating a T-shaped section. For each of the interior links, the centroid coincides with the geometrical center, but for the exterior T-shaped links, calculations are needed because the frame element should coincide with the centroid of the T-section. Rigid elements are used to connect the links to the center of the band zones. If it is desired to consider the material nonlinearity, each link may be modeled with plastic hinges at both ends to capture the plasticity at these regions. This is a good approximation because yielding of the panels only occurs at these regions. Figure 19 shows the simplified model. In this figure, the black circles represent the plastic hinge locations in the panel. The plastic hinge properties are based on the moment-rotation curves of the links.

The moment-rotation curve used to define the plastic hinges is very important because it dictates the global behavior of the panel. Figure 20 shows the moment-rotation curve recommended by ASCE 41 (ASCE, 2007). Point B

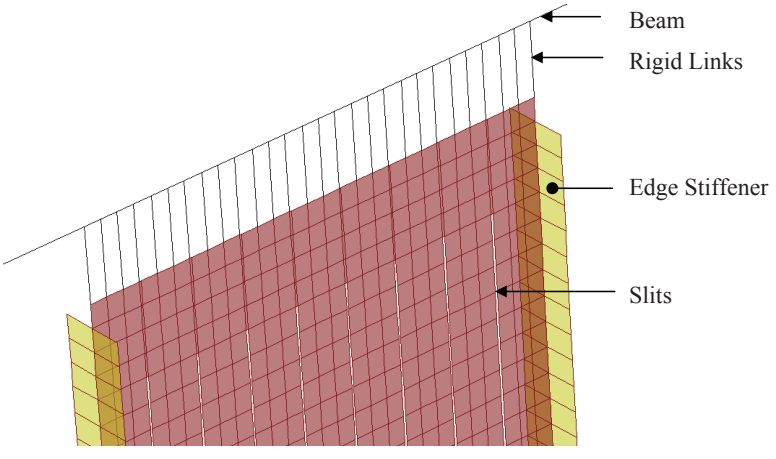

Fig. 18. Finite element model of the panel using shell elements.

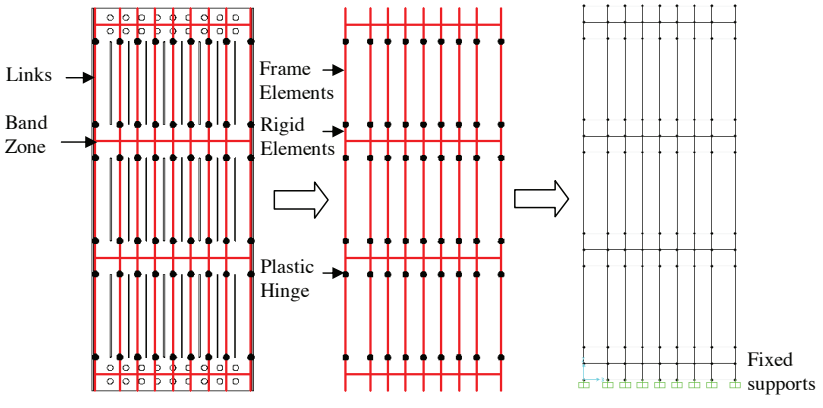

Fig. 19. Simplified panel model.

represents the point of first yield at the link. The yield moment, M_y, is given by Equation 19. In this equation, S_x is the section modulus.

$$M_y = S_x F_y \tag{19}$$

The yield rotation, θ_y, may be obtained from Equation 20 (ASCE, 2007). This equation assumes that the point of contraflexure occurs at mid-height of the link. In this equation, Z_x is the plastic modulus of the link and l is the length of the link; other parameters were previously defined.

$$\theta_y = \frac{Z_x F_y l}{6EI_{link}} \tag{20}$$

Point C of Figure 20 is the moment that causes the link to fail. Conservatively, this point was calibrated to occur when the panel reaches a displacement of 4% of its height. The moment corresponding to point C is the plastic moment of the section. For square sections, as is the case of the inner links, the plastic capacity of the section is 1.5 times the yield moment capacity. However, a value of 1.1 of the yield moment capacity is suggested for two main reasons: (1) the full plastic moment capacity may not necessarily be developed (e.g., if lateral-torsional buckling or shear buckling occurs) and (2) experiments correlated better with the suggested value of 1.1. In addition, the FEMA 356 Commentary (FEMA, 2000) mentions that the slope from B to C is usually between 0 to 10%. Point D was taken as the rotation corresponding to 4.5% interstory drift, and it was assumed that the residual moment capacity is 0.3 times the yield moment capacity. The 4.5% drift value was used to avoid a sharp transition from point C to D; otherwise, computational difficulties may occur. The residual strength was conservatively assumed as $0.3M_y$ to account for the capacity of the panel to resist loads after drift values beyond 4.5%. Point E was defined at 6% interstory drift based on experiments. However, it was observed that even if no residual strength had been assumed, similar results would be achieved.

The rotation at the links may be calculated from the rotation of the story, which is equivalent to the interstory drift. Because only the links rotate (the band zones do not rotate), the rotation at the links is calculated by multiplying the rotation of the story (interstory drift) by the ratio of the story height to the height of all links. This is expressed in the following equation:

$$\theta_{link} = \left(\frac{H_{story}}{ml}\right)\theta_{story} \tag{21}$$

In this equation, H_{story} represents the story height, and ml is the number of rows of links, m, multiplied by the height of one link, l. Note that this equation is used to convert the global behavior of the panel, observed in experimental tests, to local behavior in the links. Thus, the interstory drifts at which points B, C, D and E of Figure 20 occur are converted to rotation at the links by means of this equation.

To validate the simplified model (considering material plasticity), the results from the two experimental tests were compared to simplified models of the specimens. Figure 21 shows the moment-rotation curves used for modeling the nonlinear hinges in the interior and exterior links. Figure 22 shows the load-displacement curve for one test and the results from a nonlinear static analysis of the simplified model. The results from the simplified model compare fairly well with the experiment.

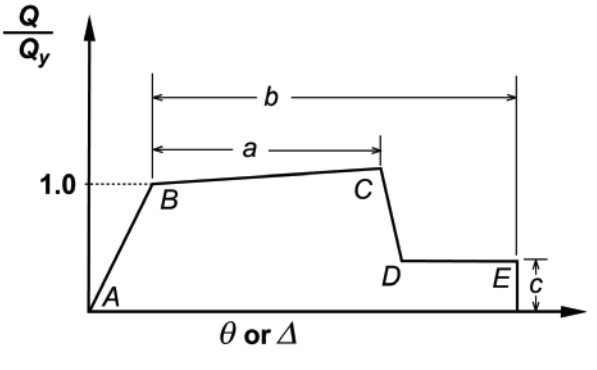

Fig. 20. Moment-rotation curve used for hinges (ASCE, 2007).

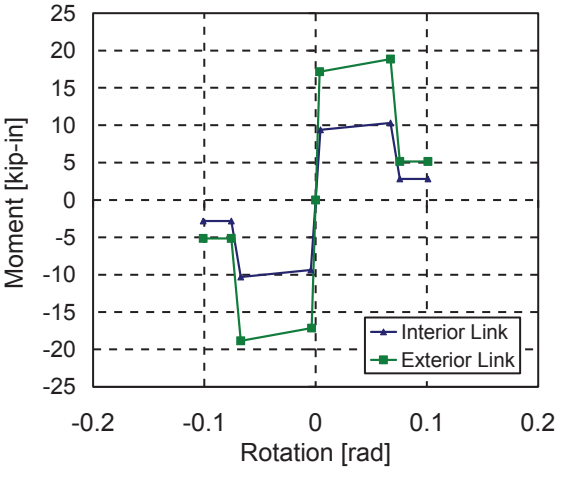

Fig. 21. Moment-rotation curve used for PF-3 panel hinges.

CONCLUSIONS

Steel slit panels (SSPs) exhibit ductile behavior and can be used in steel slit panel frames (SSPFs) for lateral resistance. The SSPF is designed to resist 100% of the base shear. The procedures for design of an SSP and SSPF have been provided. Recognizing that drift is likely to control the design, a method for designing the frame to satisfy drift limits was explained. Two prototype building designs were presented: one building has three stories; the other has ten stories. Two configurations were studied for the three-story frame. This study indicates that SSPFs are a viable SFRS for low- to medium-rise buildings.

Future research should be carried out to assess the performance of the system according to ASCE 41 (ASCE, 2007). In addition, the FEMA P695 methodology (FEMA, 2009) should be followed to determine seismic design parameters such as R and C_d. Finally, further experimental studies (e.g., quasi-static cyclic tests, shaking table tests) of full-scale frames are highly recommended. These would allow further verification of the design formulas and design approach explained in this paper.

ACKNOWLEDGMENTS

The authors would like to thank the American Institute of Steel Construction (AISC), Cives Steel and our AISC project oversight committee for their support and contributions to this research.

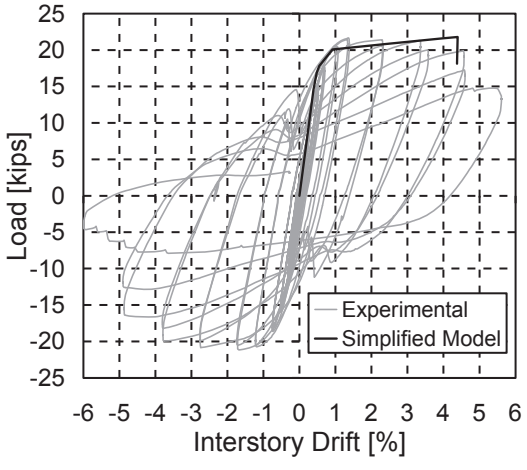

Fig. 22. PF-3 load-displacement curve from test and from simplified model.

REFERENCES

AISC (2005a), *Specification for Structural Steel Buildings*, ANSI/AISC 360-05, American Institute of Steel Construction, Chicago, IL.

AISC (2005b), *AISC Steel Construction Manual Companion*, v. 13.0, American Institute of Steel Construction, Chicago, IL.

AISC (2005c), *Seismic Provisions for Structural Steel Buildings*, ANSI/AISC 341s1-05, American Institute of Steel Construction, Chicago, IL.

AISC (2005d), *Steel Construction Manual*, 13th ed., American Institute of Steel Construction, Chicago, IL, pp. 9–15.

ASCE (2005), *Minimum Design Loads for Buildings and Other Structures*, ASCE 7-05, American Society of Civil Engineers, Reston, VA.

ASCE (2006), *Seismic Rehabilitation of Existing Buildings*, ASCE 41-06, American Society of Civil Engineers, Reston, VA.

Cortes, G. (2009), "Steel Slit Panel Frames for Lateral Resistance of Buildings," Ph.D. Dissertation, Department of Civil Engineering, Purdue University, West Lafayette, IN.

FEMA (2000), *Prestandard and Commentary for the Seismic Rehabilitation of Buildings*, FEMA 356.

FEMA (2009), *Quantification of Building Seismic Performance Factors*, FEMA P695, ATC-63 Project Report.

Hitaka, T. and Matsui, C. (2003), "Experimental Study on Steel Shear Wall with Slits," *Journal of Structural Engineering,* ASCE, Vol. 129, No. 5, pp. 586–595.

McCloskey, D.M. (2006), "Steel Slit Panels for Lateral Resistance of Steel Frame Buildings," MS Thesis, Department of Civil Engineering, Purdue University, West Lafayette, IN.

Richards, P. and Uang, C.-M. (2003), "Development of Testing Protocol for Short Links in Eccentrically Braced Frames," SSRP-2003/08, University of California at San Diego, San Diego, CA, pp. 4–9.

Timoshenko, S. and Gere, J.M. (1961), *Theory of Elastic Stability,* 2nd ed., McGraw-Hill, Inc., New York, NY, pp. 250–262, 367–371.

A Simple Stepped-Column Buckling Model and Computer Algorithm

JORGE VASQUEZ and RAFAEL RIDDELL

ABSTRACT

The paper presents a solution to the problem of obtaining the effective length ratios needed for the design of stepped columns. The formulation of a discrete model is presented, and a numerical algorithm is implemented to solve it as a matrix eigenvalue problem. The method is an alternative to using tabulated results, which have been obtained from closed-form solutions for a number of ideal boundary conditions, which in most practical cases is cumbersome and almost always unpredictably inaccurate. A MATLAB coding of the algorithm is provided, and examples illustrating its use are included.

Keywords: effective length, stepped columns.

The problem of obtaining the effective length ratios needed for the design of a stepped crane column (Figure 1a) can be stated in closed form using the beam-column theory (Timoshenko and Gere, 1961) to describe the flexibility of each of the column segments, together with equilibrium equations that include the *P*-delta effect. Thus the beam-column formulation takes care of what is often called the *P*-δ effect and global member equilibrium handles the *P*-Δ effect. The difficulty with this exact approach is that it leads to a transcendental eigenvalue problem, that is, one in which the eigenvalue is a multiplier of arguments of functions, as for instance, of the angle of a sine function. This is much more complicated than the usual discrete matrix eigenvalue problem appearing in many fields of practical engineering. For a general case, a rather elaborate solution algorithm (Watson and Howson, 2004) will be required. However, for some specific ideal boundary conditions (free, pinned, sliding, fixed), results have been made available under tabular form, as in AISC Steel Design Guide 7, *Industrial Buildings–Roofs and Anchor Rods* (Fisher, 2004) and in AISE Technical Report No. 13, *Guide for the Design and Construction of Mill Buildings* (2003). Common practice is to interpolate the values for more realistic elastic restraint boundary conditions, as well as, of course, for parameter combinations for which the table is lacking an entry. Charts have been also prepared for the pinned-base case (Fraser, 1990) and for the fixed-base case (Fraser and Bridge, 1990). But, as in many other instances, today's designers can easily replace tables and charts by short computer programs that, for the tabulated entries, readily yield the same or better results and, without interpolation, identical precision values for parameter combinations not tabulated. Furthermore, these programs

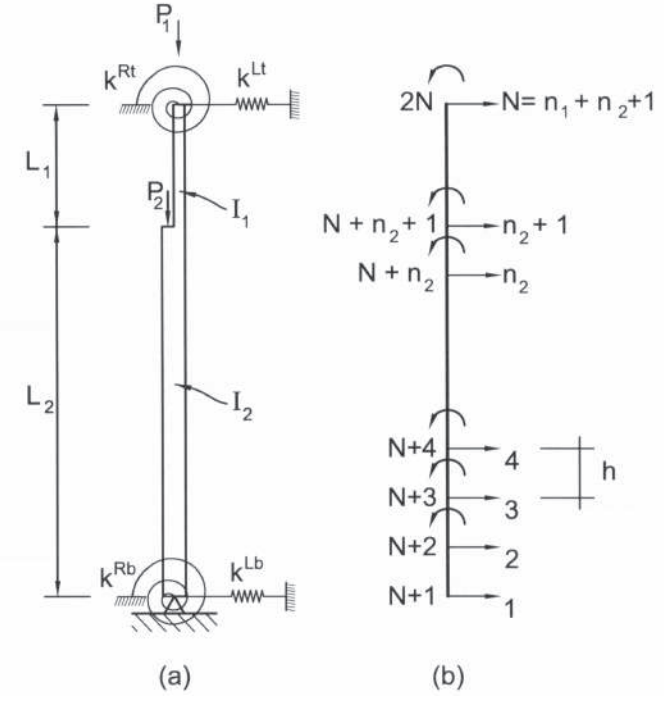

Fig. 1. The stepped-column: (a) idealization; (b) model.

Jorge Vasquez, Ph.D., Professor Emeritus, Universidad Catolica de Chile, Macul, Santiago, Chile. E-mail: mailto:jvasquez@ing.puc.cl

Rafael Riddell, Ph.D., Professor of Civil Engineering, Universidad Catolica de Chile, Macul, Santiago, Chile (corresponding author). E-mail: riddell@ing.puc.cl

often open the possibility of attaining greater generality in problem specification. This is the case of stepped-column design, in which a straightforward intuitive approach leads to a simple model that can include all of the features that need to be considered to evaluate the *K* factors to be used in analysis and design procedures that do require them. Some forms of second-order analysis, such as the direct analysis (Schmidt, 2001; AISC, 2005), which make no use of *K* factors, are unrelated to this paper. The purpose of the paper is to present the formulation of the stepped-column model and a computer algorithm that will provide the required results. A MATLAB (MATLAB, 2005) coding of this algorithm is presented. Application examples are included.

A DISCRETE MODEL FOR BEAM-COLUMN BEHAVIOR

By dividing a column into a number of short, elementary, bending-theory elements that are assembled taking into account the *P*-delta effect, beam-column behavior can be modeled with a precision that rapidly increases with the number of elements into which the column is divided. The division in a large number of elements numerically achieves the bending-axial interaction that in closed-form solutions would be established at a differential level.

The stiffness equation of an element of length *h* resulting from such subdivision can be written as:

$$(\mathbf{K}^e + f\mathbf{K}^{ge})\,\mathbf{q}^e = \mathbf{Q}^e \tag{1}$$

where $\mathbf{K}^e$ is the ordinary elastic stiffness matrix, $\mathbf{K}^{ge}$ is the *P*-delta geometric stiffness matrix of the element considering the second-order equilibrium effect of its nominal axial force *P*, *f* is an amplification factor of the axial loads, $\mathbf{q}^e$ is the local degree-of-freedom displacement vector, and $\mathbf{Q}^e$ is the local degree-of-freedom force vector. For the degree-of-freedom numbering of Figure 2, the two matrices are given as follows (Przemieniecki, 1968):

$$\mathbf{K}^e = \frac{EI}{h^3}\begin{bmatrix} 12 & 6h & -12 & 6h \\ 6h & 4h^2 & -6h & 2h^2 \\ -12 & -6h & 12 & -6h \\ 6h & 2h^2 & -6h & 4h^2 \end{bmatrix}$$

$$\mathbf{K}^{ge} = \frac{P}{h}\begin{bmatrix} -1 & 0 & 1 & 0 \\ 0 & 0 & 0 & 0 \\ 1 & 0 & -1 & 0 \\ 0 & 0 & 0 & 0 \end{bmatrix} \tag{2}$$

where *E* is the modulus of elasticity, *I* is the moment of inertia of the cross section and *P* is the axial load of the element. The axial force, *P,* can change from element to element so that, if needed, a variable axial load beam-column can be modeled.

The assemblage of the total stiffness matrix of the structure $\mathbf{K}^{tot}$ can be performed using the standard direct stiffness procedure by adding the combined elastic-geometric stiffness:

$$\mathbf{K}^{e,tot} = \mathbf{K}^e + f\mathbf{K}^{ge} \tag{3}$$

as the contribution of each element. However, it is preferable to write:

$$\mathbf{K}^{tot} = \mathbf{K} + f\mathbf{K}^g \tag{4}$$

where the matrices $\mathbf{K}$ and $\mathbf{K}^g$ result from separately assembling, by direct stiffness, the $\mathbf{K}^e$ matrices of the elements into the structure's ordinary elastic stiffness matrix $\mathbf{K}$ and the $\mathbf{K}^{ge}$ matrices of the elements into the structure's geometric stiffness $\mathbf{K}^g$. With these definitions, the stiffness equation of the model will read:

$$(\mathbf{K} + f\mathbf{K}^g)\,\mathbf{q} = \mathbf{Q} \tag{5}$$

Analysis will show that the structural stiffness degrades as *f* increases. And it degrades until the stiffness matrix becomes singular for a certain critical amplification factor f^{cr}. The meaning of this singularity is that for that amplification of the load, instability (i.e., buckling) occurs.

As in the analytical counterpart of this numerical approach, f^{cr} is independent of the applied lateral load, as represented by the load vector $\mathbf{Q}$. It is also independent of the eccentricities that the axial load may eventually present throughout the length of the member. Such eccentricities will certainly induce deformation-independent additional contributions to the load vector $\mathbf{Q}$, which are relevant in

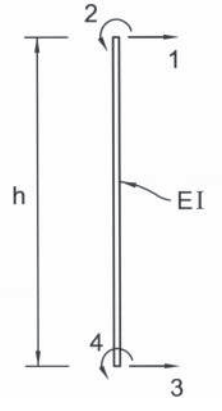

Fig. 2. Element local degrees of freedom.

beam-column stress analysis but not in buckling. Indeed, the "P-eccentricity" terms appearing in the equilibrium of the members will in no way alter the stiffness of the model, whereas instability requires a softening modification of the stiffness matrix.

The fact that buckling is eventually reached by successively increasing the f factor can be used to develop step-by-step schemes that will give f^{cr} within whatever precision is desired. Implementation of a scheme of this type is viable, but it will probably turn out to be a somewhat awkward procedure requiring an ad-hoc convergence strategy. Fortunately, there is a much more straightforward way to achieve the same goal. It arises from stating that there has to exist at least one displacement vector $\mathbf{q} = \mathbf{v}$ such that:

$$(\mathbf{K} + f\mathbf{K}^g)\mathbf{v} = \mathbf{0} \tag{6}$$

Actually there are as many such vectors as there are lateral displacement degrees of freedom in the model; they are the solution of the eigenvalue problem:

$$\mathbf{K}\mathbf{v} = -f\mathbf{K}^g\mathbf{v} \tag{7}$$

Consequently, for obvious physical reasons, f^{cr} is the lower eigenvalue (the one having the smallest magnitude), usually called the first eigenvalue. The corresponding $\mathbf{v}$ eigenvector is, of course, the associated buckling mode shape. The calculation of only the first eigenvalue is not at all costly; it can be easily obtained through inverse matrix iteration.

COMPUTER IMPLEMENTATION FOR CRANE COLUMNS

For the case of a typical crane column, there are only two distinct segments with different properties (Figure 1a): the upper shaft, with a moment of inertia I_1, length L_1 and a weight per unit length w_1, and the bottom shaft, with a moment of inertia I_7, length L_2 and a weight per unit length w_2. The column has a vertical applied load at the top of the column, P_1, and the crane load P_2 applied at the step. The maximum internal axial compression force in the upper shaft is then $P_U = P_1 + w_1L_1$, and in the lower shaft it is equal to the total load $P_T = P_1 + P_2 + w_1L_1 + w_2L_2$. In practical applications, the significance of w_1 and w_2 is minor.

When choosing how to divide the total length $L = L_1 + L_2$ of the column into short elements, it is convenient to make sure one gets elements of approximately equal length in both segments. With such a criterion, the total number of elements n will be found to be distributed into n_1 elements of the upper segment of the column and n_2 of the lower segment (Figure 1b).

To keep degree-of-freedom numbering as orderly as possible, it is preferable to assemble the structural system's $\mathbf{K}$ and $\mathbf{K}^g$ matrices first and only then suppress the fixed degrees of freedom the structure may have. Figure 1b shows the structural model, where, for the sake of keeping notation simple, N stands for the total number of divisions incremented by 1 ($N = n_1 + n_2 + 1$). From the model, it is easy to read the incidence index vectors of the elements needed for the direct stiffness assemblage into the $\mathbf{K}$ and $\mathbf{K}^g$ matrices. They are the vectors containing the numbers of the global degrees of freedom that coincide with the four local degrees of freedom of the element. For the first—the bottom—element its incidence vector is:

$$\mathbf{a} = \begin{bmatrix} 2 & N+2 & 1 & N+1 \end{bmatrix} \tag{8}$$

as can be read from comparing the local degrees of freedom of Figure 2 with the global degrees of freedom of Figure 1b. For the second element, the same vector $\mathbf{a}$ is used by adding 1 to all of its four components; then for the third element, the vector $\mathbf{a}$ is once again updated by adding 1 to all its components; and so on.

The model allows a quite general set of different boundary conditions. The lateral and rotational displacements at the bottom end can be specified as either fixed or as having elastic restraints, k^{Lb} and k^{Rb}, and in the same way the lateral and rotational displacements at the top end can be specified as either fixed or as having elastic restraints, k^{Lt} and k^{Rt}. The elastic restraint boundary conditions must be imposed by adding to the diagonal of $\mathbf{K}$ the stiffnesses k^{Lb} in the first row, k^{Rb} in the Nth row, k^{Lt} in the $(N+1)th$ row and k^{Rt} in the $2Nth$ row. Finally, the rows and columns of $\mathbf{K}$ and $\mathbf{K}^g$ corresponding to whatever degrees of freedom are prescribed as fixed must be suppressed. These are the degrees of freedom assigned with the numbers 1, N, $N + 1$, or $2N$, according to whether the corresponding restraint k^{Lb}, k^{Rb}, k^{Lt} or k^{Rt} is specified as infinite, or not. A vector $\mathbf{r}$, containing the indices of the fixed degrees of freedom, determines the rows and columns of matrices $\mathbf{K}$ and $\mathbf{K}^g$ that, after all the elastic restraints have been added, have to be suppressed.

There is also allowance for the specification of lateral and rotational displacement boundary conditions at an intermediate point. This feature is intended to account for the "lateral support usually provided at the level of the crane runway girder seat" (Galambos, 1989) when analyzing weak axis buckling. The point is specified through its distance L_s to the bottom end, which might be different from L_2, and it will be readily associated to the corresponding lateral degree of freedom n_s. The lateral and rotational displacements can be either fixed or have elastic restraints, k^{Ls} and k^{Rs}. The stiffness k^{Ls} has to be added to the n_sth row of the diagonal of $\mathbf{K}$, or, if specified as infinite, the degree of freedom n_s will have to be incorporated into the index vector $\mathbf{r}$. The same holds for the rotational stiffness k^{Rs}, but with the degree of freedom $N + n_s$ taking the place of n_s.

Table 1. Computed Equivalent Length Factors for $I_1/I_2 = 0.3$ and $L_1/L = 0.5$														
	Pin-Pin		Fixed-Free		Fixed-Pin		Fixed-Slider		Fixed-Fixed		Pin-Fixed		Pin-Slider	
P_2/P_T	K_1	K_2	K_1	K_2	K_1	K_2	K_1	K_2	K_1	K_2	K_1	K_2	K_1	K_2
0.0	0.833	1.520	1.332	2.432	0.578	1.055	0.718	1.310	0.407	0.743	0.533	0.972	1.876	3.435
0.2	0.872	1.424	1.344	2.196	0.598	0.977	0.746	1.219	0.427	0.697	0.563	0.919	2.047	3.343
0.4	0.934	1.321	1.367	1.933	0.632	0.894	0.797	1.127	0.458	0.647	0.610	0.863	2.305	3.260
0.6	1.049	1.212	1.415	1.634	0.697	0.805	0.901	1.040	0.516	0.595	0.696	0.804	2.751	3.176
0.8	1.341	1.095	1.586	1.295	0.870	0.711	1.181	0.963	0.661	0.540	0.910	0.743	3.788	3.093
1.0		0.969		1.000		0.612		0.902		0.481		0.681		3.010

Once the rows and columns of $\mathbf{K}$ and $\mathbf{K}^g$ specified by the index vector $\mathbf{r}$ are suppressed, the first eigenvalue problem is solved through inverse matrix iteration. With the eigenvalue f^{cr}, the K_1 and K_2 equivalent-length factors of AISC Steel Design Guide 7, *Industrial Buildings–Roofs and Anchor Rods* (Fisher, 2004), are calculated as:

$$K_1 = \sqrt{\frac{\pi^2 EI_1}{f^{cr} P_U L^2}} \tag{9a}$$

$$K_2 = \sqrt{\frac{\pi^2 EI_2}{f^{cr} P_T L^2}} \tag{9b}$$

The Appendix contains the MATLAB coding of this implementation. In addition to the main function's output, the code will plot the buckling mode shape. Translation of the MATLAB coding to some other numerical computation software package should prove to be quite direct.

APPLICATION EXAMPLE 1

As a first test of the numerical procedure, and for comparison purposes, a block of the table in AISC Steel Design Guide 7, *Industrial Buildings–Roofs and Anchor Rods* (Fisher, 2004), was recalculated. The block chosen is the one for ratio I_1/I_2 equal to 0.3 and ratio L_1/L equal to 0.5. As in the reference, it is tabulated in terms of the ratio between the crane load P_2 and the total load P_T (which, because the reference ignores self-weight, is just equal to $P_1 + P_2$). The results K_1 and K_2, all computed with n equal to 100, are the entries of Table 1. Within four-figure precision, the values obtained undergo absolutely no change for n larger than 100 so that the numerical processes can be regarded as having converged to the exact value. Comparison shows almost total agreement, with negligible differences no larger than 0.2%, except for the pin-slider end condition, where there seems to exist a small 1% error in some of the entries of the reference's table. The following MATLAB calling sequence was used to have the function output the entries in the first row and first column of Table 1 ($P_1 = 1$, $P_2 = 0$):

```
E = 1;
I1 = 0.3; I2 = 1;
L1 = 0.5; L2 = 0.5;
P1 = 1.0; P2 = 0.0;
kLt = Inf; kRt = 0; kLb = Inf; kRb = 0;
Ls = 0; kLs = 0; kRs = 0;
w1 = 0; w2 = 0;
n = 100;
[fcr,K1,K2,Dinfo,Vinfo] = SteppedColumn(E,I1,I2,L1,L2,P1,P2,...
kLt,kRt,kLb,kRb,Ls,kLs,kRs,w1,w2,n);
```

The relevant results are $K_1 = 0.83265$ and $K_2 = 1.52020$. The rest of the pin–pin column of the table will be obtained by modifying the definition of P_1 and P_2 as appropriate. Other columns of the table are obtained by modifying the end restrictions.

APPLICATION EXAMPLE 2

As a second test, the classical problem of finding the critical load factor of a fixed-free column under its own weight was solved. The analytical solution of the simple case of a prismatic bar is given by Timoshenko and Gere (1961). Naturally, in this case, the ratio L_1/L_2 into which the column is divided turns out to be immaterial. With the data of the following MATLAB calling sequence:

```
E = 1;
I1 = 1; I2 = 1;
L1 = 0.5; L2 = 0.5;
P1 = 0.0; P2 = 0.0;
kLt = 0; kRt = 0; kLb = Inf; kRb = Inf;
Ls = 0; kLs = 0; kRs = 0;
w1 = 1; w2 = 1;
n = 100;
[fcr,K1,K2,Dinfo,Vinfo] = SteppedColumn(E,I1,I2,L1,L2,P1,P2,...
kLt,kRt,kLb,kRb,Ls,kLs,kRs,w1,w2,n); fcr
```

The result for the critical load factor given by the function SteppedColumn is indeed the same $f^{cr} = 7.837$ value derived by Timoshenko and Gere.

APPLICATION EXAMPLE 3

The SteppedColumn function is now used to obtain the effective length factors for a crane stepped-column part of the mill building frame shown in Figure 3, which corresponds to an actual design, considering the computed elastic support provided by the rest of the frame.

Due to wind load effects, exterior columns control. One crane operates in each of the bays of the building. The most critical condition is when the two cranes align with one and the same frame, having their maximum load next to the exterior column of the corresponding bay. Both exterior columns would simultaneously be subjected to their maximum load condition. The lighter-loaded central columns will provide in-plane sway constraint to the heavier-loaded columns. Symmetry leads to each interior column providing lateral restraint to its neighboring exterior column. The restraint is exerted through the roof beam, which will also provide rotational restraint to the column. The translational and rotational restraints offered to the exterior columns at their top can be regarded as being provided by the substructure shown in Figure 4. The designer can estimate the values of the corresponding elastic constants through different schemes. The one chosen here was static condensation of the substructure's stiffness matrix in terms of the two corresponding degrees of freedom (lateral and rotational displacement at the connection point). With that approach, the result $k^{Lt} = 4.868$ kip/in. and $k^{Rt} = 1.293$e6 kip-in. was reached. A coupling stiffness coefficient was also found, –604.4 kip-in./in., that, through minor modifications of the computer code, can perfectly well be handled but whose effect was found to be not sufficiently significant to worry about it. The axial loads applied are, at the top, $P_1 = 75$ kips, and, at the step, $P_2 = 180$ kips. The column bases are to be considered fully fixed. Using this data, the following MATLAB calling sequence can be written:

```
E = 30000;  %ksi
%Upper shaft data; W27x178
P1 = 75;    %kips
L1 = 10;    %ft
I1 = 6990;  %in^4
w1 = 178;   %lb/ft
%Lower shaft data; W40x298
P2 = 180;   %kips
L2 = 59;    %ftt
I2 = 24200; %in^4
w2 = 298;   %lb/ft
%Unit conversions
w1 = w1/12/1000; w2 = w2/12/1000;   %kip/in
L1 = L1*12; L2 = L2*12;             %in
```

```
%Boundary conditions data
kLt = 4.868;         %kip/in
kRt = 1.292e+006;    %kip-in
kLb = Inf; kRb = Inf;Ls = 0; kLs = 0; kRs = 0;
n = 100;
[fcr,K1,K2,Dinfo,Vinfo] = SteppedColumn(E,I1,I2,L1,L2,P1,P2,...
kLt,kRt,kLb,kRb,Ls,kLs,kRs,w1,w2,n);
```

which leads to the buckling mode shape of Figure 5. The output arguments K_1 and K_2 are posted in the figure together with f^{cr}, as well as information that may be useful in the design procedure and a complete listing of the input data.

Reading the K factors from the table in AISC Steel Design Guide 7 (Fisher, 2004) would be a quite cumbersome procedure. Indeed, it would first require performing for three cases, the fixed-free, the fixed-pin and the fixed-slider—a numerical three-way interpolation for the ratios $I_1/I_2 = 0.284$, $L_1/L_2 = 0.855$ and $P_2/(P_1+P_2) = 0.706$—using four entry readings for each interpolated result. This is a tedious task but straightforward. What is not at all straightforward is the next step, which calls for interpolation between the values obtained for the three ideal cases, assigning them weights supposed to reflect the effect of the lateral and rotational elastic restraint constants involved. Clearly, such is a guesswork process that can hardly be considered reliable.

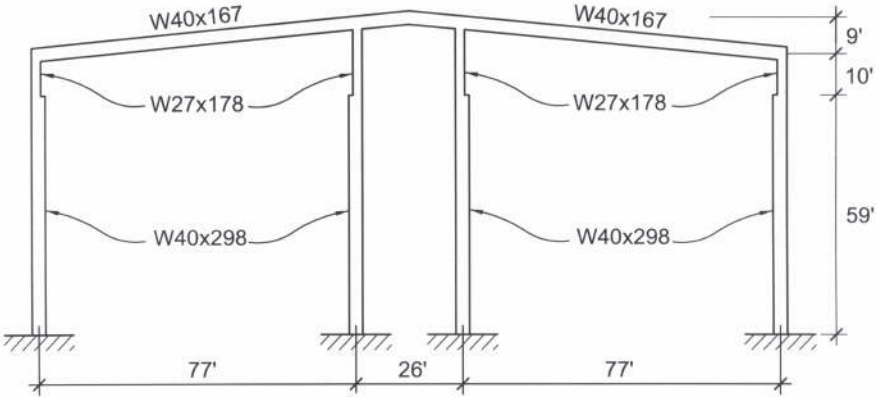

Fig. 3. Mill building frame of Example 3.

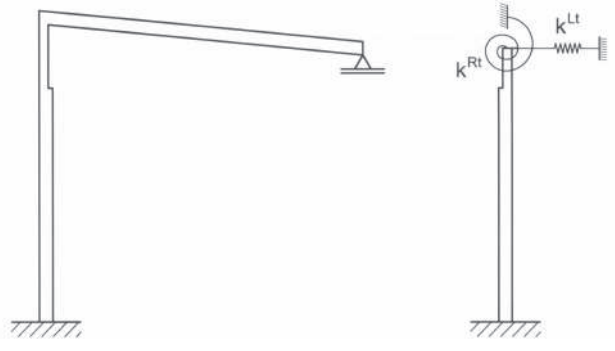

Fig. 4. Substructure providing restraint to exterior columns.

CONCLUSIONS

A simple model for a stepped column was formulated, in which the column is divided into a number of segments that are considered linear in their deformation, linear-elastic in their flexibility, but subjected to second-order effects in their equilibrium. Thus, the so-called *P*-Δ aspect of the *P*-delta effect imposed at each segment level achieves the inclusion of the *P*-δ aspect, as the number of segments increases, that would otherwise require the use of beam-column analytical formulas. The problem of finding the critical load, and hence the effective lengths, is then rendered a discrete matrix eigenvalue problem instead of a continuous transcendental one. A computer code, a MATLAB function, implementing an algorithm based on the model was developed, and applied to three examples. A division into 100 segments was found to be suitable in all three cases, while keeping processing requirements well within very reasonable time limits. The first example shows the complete coincidence of the results obtained from the function with entries from the well-known table in AISC Steel Design Guide 7 (Fisher, 2004). The second example is a successful comparison with a theoretical problem discussed by Timoshenko and Gere (1961), using the available, but not all that important, self-weight capability. The third example computes the "exact" *K* factors required for the design for individual member stability of a crane column of an actual mill building; reading the *K* factors from the table in AISC Steel Design Guide 7 would be a very cumbersome and unreliable procedure.

REFERENCES

AISC (2005), *Steel Construction Manual*, 13th ed., American Institute of Steel Construction, Chicago, IL.

AISE (2003), Technical Report No. 13, *Guide for the Design and Construction of Mill Buildings*, Association of Iron and Steel Engineers, Pittsburg, PA.

Fisher, J.M. (2004), *Steel Design Guide 7, Industrial Buildings—Roofs and Anchor Rods*, American Institute of Steel Construction, Chicago, IL.

Fraser, D.J. (1990), "The In-Plane Stability of a Frame Containing Pin-Based Stepped Columns," *Engineering Journal*, AISC, 2nd Quarter, pp. 49–53.

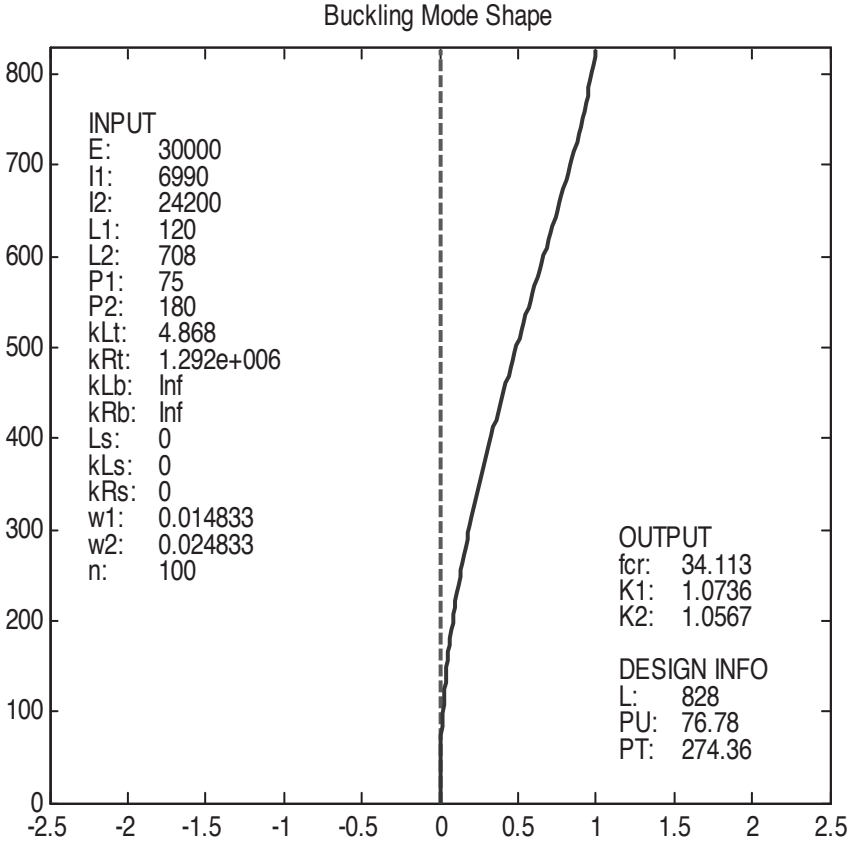

Fig. 5. Graphical MATLAB output for Example 3.

Fraser, D.J. and Bridge, R.Q. (1990), "Buckling of Stepped Crane Columns," *Journal of Constructional Steel Research*, Vol. 16, pp. 23–28.

Galambos, T.V. (1998), *Guide to Stability Design Criteria for Metal Structures*, 5th ed., John Wiley & Sons, Inc., New York, NY.

MATLAB (2005), *The Language of Technical Computing*, Version 7.0.4, The MathWorks, Inc., Natick, MA.

Przemienecki, J.S. (1968), *Theory of Matrix Structural Analysis*, McGraw-Hill, Inc., New York, NY.

Schmidt, J. (2001), "Design of Mill Building Columns Using Notional Loads," *Engineering Journal*, AISC, 2nd Quarter, pp. 90–99.

Timoshenko, S.P. and Gere, J.M. (1961), *Theory of Elastic Stability*, McGraw-Hill, Inc., New York, NY.

Watson, A. and Howson, N.P. (2004), "Buckling of Spring Supported Tapered Columns Allowing for Shear Deformation," *Proceedings of the International Conference on Computational & Experimental Engineering,* Madeira, Portugal, pp. 2105–2110.

APPENDIX

MATLAB Code

```
function [fcr,K1,K2,Dinfo,Vinfo] = SteppedColumn(E,I1,I2,L1,L2,P1,P2,...
        kLt,kRt,kLb,kRb,Ls,kLs,kRs,w1,w2,n)
% DESCRIPTION:
%       computes critical load factors for a stepped column formed by two
%       segments of different cross-sectional shapes with loads both at the
%       top end and at the step, with choice of different elastic or fixed
%       end conditions; the own weight of shafts can de handled separately
% USE:
%       [fcr,K1,K2,Dinfo,Vinfo] = SteppedColumn(E,I1,I2,L1,L2,P1,P2,...
%        kLt,kRt,kLb,kRb,Ls,kLs,kRs,w1,w2,n)
% INPUT:
%       E       Modulus of elasticity
%       I1      Moment of inertia of the upper shaft cross-section
%       I2      Moment of inertia of the lower shaft cross-section
%       L1      Length of the upper shaft
%       L2      Length of the lower shaft
%       P1      Vertical load applied at the top of the column
%       P2      Vertical load applied at the step
%       kLt     Lateral spring constant at the top (Inf for fixed)
%       kRt     Rotational stiffness at the top (Inf for fixed)
%       kLb     Lateral spring constant at the base (Inf for fixed)
%       kRb     Rotational stiffness at the base (Inf for fixed)
%       Ls      Distance from base to intermediate step support point
%       kLs     Lateral spring constant at the step (Inf for fixed)
%       kRs     Rotational stiffness at the step (Inf for fixed)
%       w1      Weight per unit length of the upper shaft
%       w2      Weight per unit length of the lower shaft
%       n       Specified number of divisions of the length of the column
% OUTPUT:
%       fcr     Critical factor for the specified loads
%       K1      Upper shaft equivalent length factor =pi*sqrt(E*I1/(fcr*PU))/L
%       K2      Lower shaft equivalent length factor =pi*sqrt(E*I2/(fcr*PT))/L
```

```
%       Dinfo   Vector containing information needed for design
%               L  = L1 + L2
%               PU = P1 + w1*L1
%               PT = P1 + P2 + w1*L1 + w2*L2
%       Vinfo   Buckling mode shape information given through a three column
%               matrix: first column contains the lateral displacements;
%               second column, the rotational displacements; third column,
%               the corresponding coordinates (from the bottom)
% ALGORITHM:
%       The column is divided into n bending elements with inclusion of the
%       P-delta effect; the elastic stiffness matrix K and the geometric
%       stiffness matrix Kg are assembled, and the eigenvalue problem
%       Kc*v = f*Kg*v is solved, with a result in which fcr equal to lowest
%       eigenvalue is the critical factor of the loads
%       The first eigenvalue and eigenvector are obtained by inverse matrix
%       iteration using the adjoining function inv_mat_iter
% NOTES:
%       ALL INPUT ARGUMENTS MUST BE SPECIFIED; ENTER 0 WHERE NOT RELEVANT
%       ALL OUTPUT ARGUMENTS MUST BE SPECIFIED

L = L2 + L1;                    %Total column length
PU = P1 + w1*L1;                %Axial force at bottom end of upper shaft
PT = PU + P2 + w2*L2;           %Axial force at bottom end of lower shaft
dL = L/n;                       %Divisions to have about the same length
n2 = round(L2/dL);
n1 = round(L1/dL);
N = n2 + n1 + 1;
dL2 = L2/n2;
dL1 = L1/n1;
kg  = [-1  0  1  0              %Base matrix for geometric stiffness matrices
        0  0  0  0
        1  0 -1  0
        0  0  0  0];
h = dL2;                        %Bottom segment elements stiffness matrix
Ke2 = E*I2*[12     6*h   -12    6*h
            6*h  4*h^2  -6*h  2*h^2
            -12   -6*h    12   -6*h
            6*h  2*h^2  -6*h  4*h^2]/h^3;
h = dL1;                        %Top segment elements stiffness matrix
Ke1 = E*I1*[12     6*h   -12    6*h
            6*h  4*h^2  -6*h  2*h^2
            -12   -6*h    12   -6*h
            6*h  2*h^2  -6*h  4*h^2]/h^3;
%ASSEMBLE STRUCTURAL SYSTEM'S ELASTIC AND GEOMETRIC STIFFNESS MATRICES
K  = zeros(2*N);
Kg = zeros(2*N);
a = [2 N+2 1 N+1];
z(1) = 0; iz = 1;
W = 0.5*w2*dL2;
```

```
for i=1:n2
    K(a,a)  = K(a,a)  + Ke2;
    Kg(a,a) = Kg(a,a) + (PT - W)*kg/dL2;
    a = a + 1;
    W = W + w2*dL2;
    iz = iz + 1;
    z(iz) = z(iz-1) + dL2;
end
W = 0.5*w1*dL1;
for i=1:n1
    K(a,a)  = K(a,a)  + Ke1;
    Kg(a,a) = Kg(a,a) + (PU - W)*kg/dL1;
    a = a + 1;
    W = W + w1*dL1;
    iz = iz + 1;
    z(iz) = z(iz-1) + dL1;
end
%ADD SUPPORT STIFFNESSES AND/OR PREPARE FOR FIXED DOF SUPPRESSION
r = [];
if isinf(kLt)
    r = [r N];
else
    K(N,N) = K(N,N) + kLt;
end
if isinf(kRt)
    r = [r 2*N];
else
    K(2*N,2*N) = K(2*N,2*N) + kRt;
end
if isinf(kLb)
    r = [r 1];
else
    K(1,1) = K(1,1) + kLb;
end
if isinf(kRb)
    r = [r N+1];
else
    K(N+1,N+1) = K(N+1,N+1) + kRb;
end
ns = round(n2*Ls/L2) + 1;       %Find ns: "step" lateral DOF
if isinf(kLs)
    r = [r ns];
else
    K(ns,ns) = K(ns,ns) + kLs;
end
if isinf(kRs)
    r = [r N+ns];
else
    K(N+ns,N+ns) = K(N+ns,N+ns) + kRs;
end
rc = 1:2*N; rc(r) = [];         %Indices of non-fixed DOFs
K  = K(rc,rc);                  %Suppress row and columns of fixed DOFs
Kg = Kg(rc,rc);
```

```
%SOLVE FOR LOWER OR FIRST EIGENVALUE PROBLEM
[V,fcr] = inv_mat_iter(K,-Kg);
%PROCESS INFORMATION FOR OUTPUT
K1 = pi*sqrt(E*I1/(fcr*PU))/L;
K2 = pi*sqrt(E*I2/(fcr*PT))/L;
Dinfo = [L; PU; PT];            %Information that may be useful for design
q = zeros(2*N,1);               %Full 2*N DOF buckling mode shape vector
q(rc) = V;
Vinfo = [q(1:N) q(N+1:2*N) z']; %Buckling mode shape information matrix
draw_mode_shape(q,N,fcr,K1,K2,L,PU,PT,z,E,I1,I2,L1,L2,...
        P1,P2,kLt,kRt,kLb,kRb,Ls,kLs,kRs,w1,w2,n)

%%%%%%%%BEGIN ADJOINING INVERSE MATRIX ITERATION FUNCTION%%%%%%%%%%%%
function [V,f] = inv_mat_iter(K,Kg);
R = chol(K);
V = R\(R'\diag(Kg)); V = V/max(abs(V));
f0 = 0;
for j=1:100
    V = R\(R'\(Kg*V));
    f = V'*K*V/(V'*Kg*V);
    if abs(f - f0)<f*1e-6;
        break
    end
    f0 = f;
    V = V/max(abs(V));
end
%%%%%%%%%%END ADJOINING INVERSE MATRIX ITERATION FUNCTION%%%%%%%%%%%%

%%%%%%BEGIN ADJOINING DRAWING BUCKLING MODE SHAPE FUNCTION%%%%%%%%%%%
function draw_mode_shape(q,N,fcr,K1,K2,L,PU,PT,z,E,I1,I2,L1,L2,...
        P1,P2,kLt,kRt,kLb,kRb,Ls,kLs,kRs,w1,w2,n)
q = q(1:N);
MM = max(q); mm = min(q);
if abs(MM)>abs(mm)
    q = q/MM;
else
    q = q/mm;
end
clf;
plot([0 0],[0 z(N)],'r--',q,z,'b','LineWidth',2)
title('Buckling Mode Shape')
t = 0.035*L;
d = -2.25; e = -1.80; s = 0.90*L;
text(d,s,'INPUT'); s = s - t;
text(d,s,'E:')  ; text(e,s,sprintf('%0.5g',E))  ; s = s - t;
text(d,s,'I1:') ; text(e,s,sprintf('%0.5g',I1)) ; s = s - t;
text(d,s,'I2:') ; text(e,s,sprintf('%0.5g',I2)) ; s = s - t;
text(d,s,'L1:') ; text(e,s,sprintf('%0.5g',L1)) ; s = s - t;
text(d,s,'L2:') ; text(e,s,sprintf('%0.5g',L2)) ; s = s - t;
text(d,s,'P1:') ; text(e,s,sprintf('%0.5g',P1)) ; s = s - t;
text(d,s,'P2:') ; text(e,s,sprintf('%0.5g',P2)) ; s = s - t;
text(d,s,'kLt:'); text(e,s,sprintf('%0.5g',kLt)); s = s - t;
text(d,s,'kRt:'); text(e,s,sprintf('%0.5g',kRt)); s = s - t;
```

```
text(d,s,'kLb:'); text(e,s,sprintf('%0.5g',kLb)); s = s - t;
text(d,s,'kRb:'); text(e,s,sprintf('%0.5g',kRb)); s = s - t;
text(d,s,'Ls:') ; text(e,s,sprintf('%0.5g',Ls)) ; s = s - t;
text(d,s,'kLs:'); text(e,s,sprintf('%0.5g',kLs)); s = s - t;
text(d,s,'kRs:'); text(e,s,sprintf('%0.5g',kRs)); s = s - t;
text(d,s,'w1:') ; text(e,s,sprintf('%0.5g',w1)) ; s = s - t;
text(d,s,'w2:') ; text(e,s,sprintf('%0.5g',w2)) ; s = s - t;
text(d,s,'n:')  ; text(e,s,sprintf('%0.5g',n))  ; s = s - t;
d = 1.15; e = 1.55; s = 0.35*L;
text(d,s,'OUTPUT'); s = s - t;
text(d,s,'fcr:'); text(e,s,sprintf('%0.5g',fcr)); s = s - t;
text(d,s,'K1:') ; text(e,s,sprintf('%0.5g',K1)) ; s = s - t;
text(d,s,'K2:') ; text(e,s,sprintf('%0.5g',K2)) ; s = s - 2*t;
text(d,s,'DESIGN INFO'); s = s - t;
text(d,s,'L:')  ; text(e,s,sprintf('%0.5g',L)) ;  s = s - t;
text(d,s,'PU:') ; text(e,s,sprintf('%0.5g',PU));  s = s - t;
text(d,s,'PT:') ; text(e,s,sprintf('%0.5g',PT));
axis ([-2.5 2.5 0 z(N)]);
%%%%%%%%END ADJOINING DRAWING BUCKLING MODE SHAPE FUNCTION%%%%%%%%%%
```

Fillet Weld Design for Rectangular HSS Connections

JEFFREY A. PACKER and MIN SUN

ABSTRACT

The 2010 AISC *Specification for Structural Steel Buildings* has expanded the scope in Chapter K ("Design of HSS and Box Member Connections") with a new Section K4, "Welds to Branches." This paper describes the background to this development and examines the structural reliability of the weld effective length provisions contained therein. The latter is achieved by using a database of 31 welded square/rectangular hollow structural section (HSS) K-, T- and cross- (or X-) connections in which all test specimen failures were reached by fracture of the welded joints. The potential inclusion (or exclusion) of the sin θ effect, whereby fillet weld capacity is increased for loading not parallel to the axis of the weld, has also been investigated. In conclusion, some design examples are given to illustrate the weld design method, performed to the 2010 AISC *Specification* in both LRFD and ASD.

Keywords: hollow structural sections, connections, joints, welding, trusses, effective weld lengths.

WELD DESIGN PHILOSOPHY FOR HSS CONNECTIONS

AISC Design Guide 21, *Welded Connections—A Primer for Engineers* (Miller, 2006), provides excellent general advice for engineers on welding, including some particular remarks on welding hollow structural sections (HSS). It has been well known, however, that the welds at the footprint of an HSS branch member, like the four walls of the HSS branch itself, are generally loaded in a highly nonuniform manner. In particular, the branch walls (and adjacent welds) transverse to the direction of a HSS truss are liable to have a very high concentration of strain and stress at the branch corners but low strain and stress in the middle of the branch transverse wall. The lower the stress in the middle portion of a branch transverse wall, the less effective that location is in resisting load.

With HSS-to-HSS welded connections, there are currently two design philosophies that can be used for weld design, as described in AISC Design Guide 24, *Hollow Structural Section Connections* (Packer et al., 2010):

1. The weld can be proportioned so that it develops the yield strength of the connected branch wall at all locations around the branch. This will represent an upper limit on the weld size and hence be a conservative design procedure. This approach is particularly appropriate if there is low confidence in the design forces acting on the branch, or if there is uncertainty regarding method 2, or if plastic stress redistribution is required in the connection. The same effective weld size should be maintained all around the attached branch. The one exception to this latter rule is for the hidden weld in HSS-to-HSS partially overlapped K- (or N-) connections, which may be left unwelded (usually just tacked) provided the force components of the two branches normal to the chord do not differ by more than 20%. The hidden weld refers to the weld along the hidden toe of the overlapped branch, which is hidden in the final connection by the overlapping branch. This is particularly an issue with square/rectangular partially overlapped HSS-to-HSS connections where the typical fabrication procedure is to tack all the branches into place and perform final welding afterward (Packer et al., 2010).
2. The weld can be proportioned so that it resists the applied forces in the branch. This approach may be appropriate where there is high confidence in the design forces acting on the branch, or if the branch forces are particularly low relative to the branch member capacity. The latter situation often arises if the branches are sized for aesthetic reasons. For example, the branches of a simply supported truss may be the same throughout the truss, yet at the center of the truss the web member forces will be very low under uniformly distributed load. If this design philosophy is adopted, then weld effective lengths must be taken into account, because HSS connections are usually very flexible. The same effective weld size should still be maintained all around the attached branch, with the entire branch perimeter welded (including the hidden toe, if applicable).

Jeffrey A. Packer, Bahen/Tanenbaum Professor of Civil Engineering, University of Toronto, Toronto, ON, Canada (corresponding author). E-mail: jeffrey.packer@utoronto.ca

Min Sun, Research Assistant, Department of Civil Engineering, University of Toronto, Toronto, ON, Canada. E-mail: min.sun@utoronto.ca

HISTORICAL TREATMENT OF WELD DESIGN IN HSS CONNECTIONS

In 1981, Subcommission XV-E of the International Institute of Welding (IIW) produced its first design recommendations for statically loaded HSS connections, which were updated and revised with a second edition later that decade (IIW, 1989). These recommendations are still the basis for nearly all current design rules around the world dealing with statically loaded connections in onshore HSS structures, including those in Europe (CEN, 2005), Canada (Packer and Henderson, 1997) and the United States (AISC, 2010). The IIW (1989) recommendations and welding requirements are discussed next.

Fillet welds that are automatically prequalified for any member loads should be designed to give a resistance that is not less than the member capacity. This results in the following minimum throat thickness for fillet welds, assuming matched electrodes:

$$t_w \geq 0.95t_b \text{ , for Fe 360 } (F_{yb} = 235 \text{ MPa or } 34.1 \text{ ksi}) \quad (1a)$$

$$t_w \geq 1.00t_b \text{ , for Fe 430 } (F_{yb} = 275 \text{ MPa or } 39.9 \text{ ksi}) \quad (1b)$$

$$t_w \geq 1.07t_b \text{ , for Fe 510 } (F_{yb} = 355 \text{ MPa or } 51.5 \text{ ksi}) \quad (1c)$$

This requirement may only be waived where departure from them can be justified in terms of strength and deformational and/or rotational capacity.

Research at the University of Toronto (Frater and Packer, 1992a, 1992b) on fillet-welded rectangular HSS branches in large-scale Warren trusses with gapped K-connections (Figure 1) showed that fillet welds in that context can be proportioned on the basis of the loads in the branches, thus resulting in relatively smaller weld sizes compared to IIW (1989). It was concluded simplistically that the welds along all four sides of the HSS branch could be taken as fully effective when the chord-to-branch angle is 50° or less, but that the weld along the heel should be considered as completely ineffective when the angle is 60° or more. A linear interpolation was recommended when the chord-to-branch angle is between 50° and 60°. Based on this research, the formulas for the effective length of branch member welds in planar, gapped, rectangular HSS K- and N-connections, subject to predominantly static axial load, were taken in Packer and Henderson (1992) as:

When $\theta \leq 50°$:

$$L_e = \frac{2H_b}{\sin\theta} + 2B_b \quad (2a)$$

When $\theta \leq 60°$:

$$L_e = \frac{2H_b}{\sin\theta} + B_b \quad (2b)$$

In 1992, the American Welding Society (AWS) adopted these recommendations, and a linear interpolation was recommended between 50° and 60°. For the welds in planar T-, Y- and cross- (or X-) connections, AWS (1992) also implemented the following effective-length formulas based on the conclusions from the research on gapped rectangular HSS K-connections:

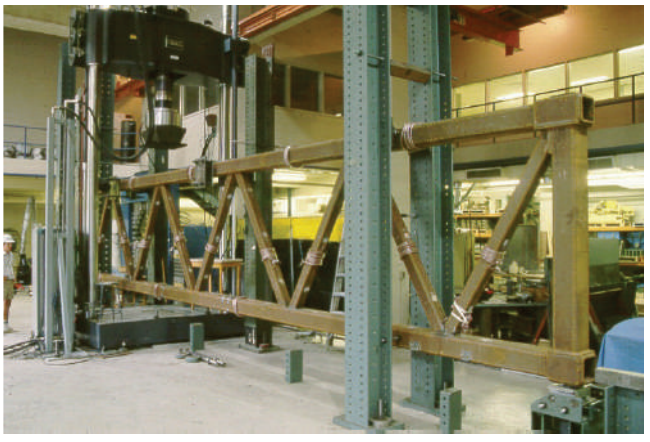

(a)

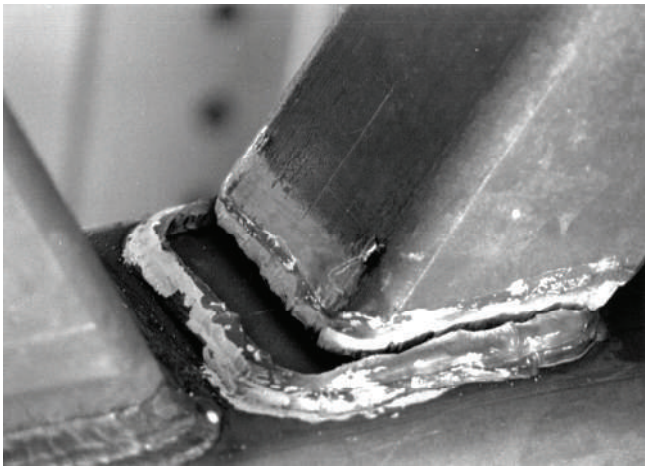

(b)

Fig. 1. Large-scale, laboratory testing of rectangular HSS K-connections: (a) welded HSS truss with gapped and overlapped K-connections; (b) weld failure in a gapped K-connection.

When $\beta \leq 0.85$:

$$L_e = \frac{2H_b}{\sin\theta} + 2B_b \quad (3a)$$

When $\beta \leq 0.85$:

$$L_e = \frac{2H_b}{\sin\theta} \quad (3b)$$

However, Packer and Henderson (1992) wrote that the addition of the $2B_b$ term in Equation 3a was likely nonconservative for $\theta \geq 60°$. In a further study by Packer and Cassidy (1995), by means of 16 large-scale connection tests that were designed to be weld-critical (Figure 2), new weld effective length formulas for T-, Y- and cross- (or X-) connections were developed. It was found that more of the weld perimeter was effective for lower branch member inclination angles for T-, Y- and cross (or X-) connections. Thus, the formulas for the effective length of branch member welds in planar T-, Y- and cross- (or X-) rectangular HSS connections, subjected to predominantly static axial load, were revised in Packer and Henderson (1997) to:

When $\theta \leq 50°$:

$$L_e = \frac{2H_b}{\sin\theta} + B_b \quad (4a)$$

When $\theta \leq 60°$:

$$L_e = \frac{2H_b}{\sin\theta} \quad (4b)$$

A linear interpolation was recommended between 50° and 60°.

The latest (third) edition of the International Institute of Welding recommendations (IIW, 2009) requires that the design resistance of HSS connections be based on failure modes that do not include weld failure, with the latter being avoided by satisfying either of the following criteria:

1. Welds are to be proportioned to be "fit for purpose" and to resist forces in the connected members, taking account of joint deformation/rotation capacity and considering weld effective lengths.
2. Welds are to be proportioned to achieve the capacity of the connected member walls.

This IIW (2009) document thus specifically acknowledges the effective-length concept for weld design. The most recent guidance on this topic (Packer et al., 2009) again notes that for ISO steel grades and matched electrodes, the minimum throat thickness for fillet welds to achieve branch member yield capacity is (CEN, 2005):

$$t_w \geq 0.92t_b \text{ , for S235 } (F_{yb} = 235 \text{ MPa or } 34.1 \text{ ksi}) \quad (5a)$$

$$t_w \geq 0.96t_b \text{ , for S275 } (F_{yb} = 275 \text{ MPa or } 39.9 \text{ ksi}) \quad (5b)$$

$$t_w \geq 1.10t_b \text{ , for S355 } (F_{yb} = 355 \text{ MPa or } 51.5 \text{ ksi}) \quad (5c)$$

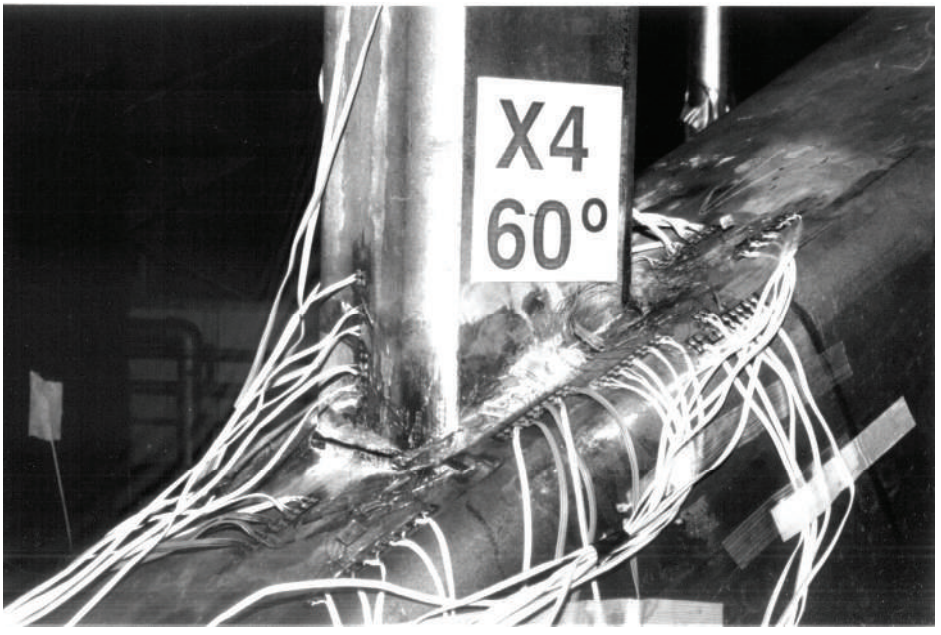

Fig. 2. Laboratory testing of rectangular HSS cross- (or X-) connections, with failure of the welds.

$t_w \geq 1.42t_b$, for S420 (F_{yb} = 420 MPa or 60.9 ksi) (5d)

$t_w \geq 1.48t_b$, for S460 (F_{yb} = 460 MPa or 66.7 ksi) (5e)

2010 AISC SPECIFICATION, SECTION K4

In Section K4 of the 2010 AISC *Specification* (AISC, 2010), a more detailed design method considering weld effective lengths (L_e) is given for different types of RHS connections and branch loadings, as described next.

T-, Y- and Cross- (or X-) Connections under Branch Axial Load or Bending

Effective weld properties are given by:

$$L_e = \frac{2H_b}{\sin\theta} + 2b_{eoi} \tag{6}$$

$$S_{ip} = \frac{t_w}{3}\left(\frac{H_b}{\sin\theta}\right)^2 + t_w b_{eoi}\left(\frac{H_b}{\sin\theta}\right) \tag{7}$$

$$S_{op} = t_w\left(\frac{H_b}{\sin\theta}\right)B_b + \frac{t_w}{3}\left(B_b^2\right) - \frac{\left(t_w/3\right)\left(B_b - b_{eoi}\right)^3}{B_b} \tag{8}$$

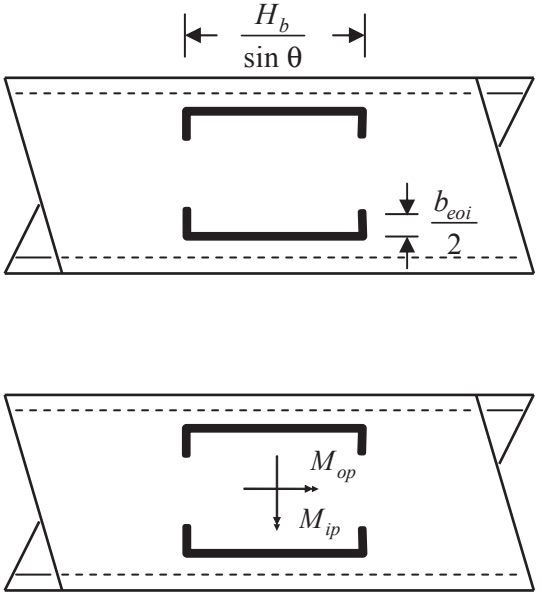

Fig. 3. Weld effective-length terminology for T-, Y- and cross- (or X-) connections: (a) weld effective length; (b) in-plane and out-of-plane bending moment directions.

$$b_{eoi} = \frac{10}{B/t}\left(\frac{F_y t}{F_{yb} t_b}\right)B_b \leq B_b \tag{9}$$

When $\beta > 0.85$ or $\theta > 50°$, $b_{eoi}/2$ shall not exceed $2t$. This limitation represents additional engineering judgment.

In contrast to Equations 4a and 4b, the weld effective length in Equation 6 was—for consistency—made equivalent to the branch wall effective lengths used in Section K2.3 of the *Specification* for the limit state of local yielding of the branch(es) due to uneven load distribution, which in turn is based on the IIW *Design Recommendations* (1989). The effective length of the weld transverse to the chord, b_{eoi}, is illustrated in Figure 3a. This term, b_{eoi}, was empirically derived on the basis of laboratory tests in the 1970s and 1980s (Davies and Packer, 1982). The weld effective elastic section moduli for in-plane bending and out-of-plane bending, S_{ip} and S_{op}, respectively (Equations 7 and 8), apply in the presence of bending moments M_{ip} and M_{op}, as shown in Figure 3b. Equation 7 can be determined by deriving:

$$\begin{aligned} I_{ip} &= 2 \times \frac{1}{12} t_w \left(\frac{H_b}{\sin\theta}\right)^3 + 4t_w\left(\frac{b_{eoi}}{2}\right)\left(\frac{H_b}{2\sin\theta}\right)^2 \\ &= \frac{t_w}{6}\left(\frac{H_b}{\sin\theta}\right)^3 + \frac{t_w b_{eoi}}{2}\left(\frac{H_b}{\sin\theta}\right)^2 \end{aligned} \tag{10}$$

and substituting into:

$$S_{ip} = \frac{I_{ip}}{\left(\frac{H_b}{2\sin\theta}\right)} \tag{11}$$

Similarly, Equation 8 can be determined by deriving:

$$\begin{aligned} I_{op} &= 2t_w\left(\frac{H_b}{\sin\theta}\right)\left(\frac{B_b}{2}\right)^2 + 2 \times \frac{1}{12} t_w\left(B_b^3\right) - 2 \times \frac{1}{12} t_w\left(B_b - b_{eoi}\right)^3 \\ &= \frac{t_w}{2} B_b^2 \frac{H_b}{\sin\theta} + \frac{t_w}{6}\left(B_b^3\right) - \frac{t_w}{6}\left(B_b - b_{eoi}\right)^3 \end{aligned} \tag{12}$$

Table 1. Measured Properties of 15 Gapped K-Connections Exhibiting Weld Failure						
Truss 1						
Connection Number	**HSS Chord Member**		**HSS Branch Member**		**θ (degrees)**	**F_{uw} (ksi)**
	$H \times B \times t$ (in. × in. × in.)	**F_y, F_u (ksi)**	**$H_b \times B_b \times t_b$ (in. × in. × in.)**	**F_{yb}, F_{ub} (ksi)**		
K1	12.02 × 8.05 × 0.472	F_y = 62.6 F_u = 74.1	5.03 × 5.03 × 0.465	F_{yb} = 57.6 F_{ub} = 73.2	60	98.3
K2						
K3						
K4						
K5						
K6						
K7						
K8						
K9						
Truss 2						
Connection Number	**HSS Chord Member**		**HSS Branch Member**		**θ (degrees)**	**F_{uw} (ksi)**
	$H \times B \times t$ (in. × in. × in.)	**F_y, F_u (ksi)**	**$H_b \times B_b \times t_b$ (in. × in. × in.)**	**F_{yb}, F_{ub} (ksi)**		
K10	8.03 × 8.03 × 0.476	F_y = 58.7 F_u = 74.8	5.04 × 5.04 × 0.472	F_{yb} = 61.3 F_{ub} = 75.7	60	78.3
K11						
K12						
K13						
K14						
K15						

and substituting into:

$$S_{op} = \frac{I_{op}}{\left(\frac{B_b}{2}\right)} \tag{13}$$

For Gapped K- and N-Connections under Branch Axial Load

Effective weld lengths are given by:

When $\theta \le 50°$:

$$L_e = \frac{2\left(H_b - 1.2t_b\right)}{\sin\theta} + 2\left(B_b - 1.2t_b\right) \tag{14a}$$

When $\theta \ge 60°$:

$$L_e = \frac{2\left(H_b - 1.2t_b\right)}{\sin\theta} + \left(B_b - 2t_b\right) \tag{14b}$$

When $50° < \theta < 60°$, a linear interpolation is to be used to determine L_e.

No provisions are given for branch moment loading because the recommended K- and N- connection design procedure in *Specification* Section K2.3 is based on axial loads only in the branches of such connections. This results from the truss design method recommended, in which all branch members are considered as pin-ended. Equations 14a and 14b are very similar to Equations 2a and 2b, but the former incorporate a reduction to allow for a typical HSS corner radius. For gapped K- and N-connections, the simplified nature of these effective-length formulas (Equations 14a and 14b) was preferred to the more complex ones that would result if the branch effective widths of the HSS walls in the *Specification* Section K2.3 were adopted. Effective weld length provisions for overlapped HSS K- and N-connections were also provided in *Specification* Section K4 (AISC, 2010), based on branch effective widths of the HSS walls in *Specification* Section K2.3; however, in this case, no research data on weld-critical overlapped HSS K- and N-connections were available.

Table 2. Measured Properties of 16 T- and X-Connections Exhibiting Weld Failure						
Connection Number	HSS Chord Member		HSS Branch Member		θ (degrees)	F_{uw} (ksi)
	$H \times B \times t$ (in. × in. × in.)	F_y, F_u (ksi)	$H_b \times B_b \times t_b$ (in. × in. × in.)	F_{yb}, F_{ub} (ksi)		
T1	9.99 × 9.99 × 0.476	$F_y = 59.5$ $F_u = 61.5$	5.00 × 5.00 × 0.480	$F_{yb} = 79.0$ $F_{ub} = 87.4$	90	83.2
T2						
T3			7.99 × 7.99 × 0.474	$F_{yb} = 64.5$ $F_{ub} = 66.8$		
T4						
X1			5.00 × 5.00 × 0.480	$F_{yb} = 79.0$ $F_{ub} = 87.4$	30	
X2					40	
X3					50	
X4					60	
X5					70	
X6					80	
X7			7.99 × 7.99 × 0.474	$F_{yb} = 64.5$ $F_{ub} = 66.8$	30	
X8					40	
X9					50	
X10					60	
X11					70	
X12					80	

Table 3. Measured Weld Sizes of Gapped K-Connections and Failure Loads of Welded Joints													
Connection Number	Weld 1 (in.)			Weld 2 (in.)			Weld 3 (in.)			Weld 4 (in.)			Joint Failure Load (kips)
	w_b	w_c	t_w	w_b	w_c	t_w	w_b	w_c	t_w	w_b	w_c	t_w	
K1	0.236	0.260	0.154	0.217	0.220	0.154	0.205	0.224	0.106	0.268	0.343	0.240	171.1
K2	0.220	0.264	0.165	0.228	0.272	0.161	0.197	0.248	0.110	0.264	0.295	0.224	177.6
K3	0.256	0.311	0.173	0.256	0.287	0.189	0.201	0.291	0.118	0.311	0.406	0.276	175.8
K4	0.295	0.283	0.197	0.272	0.299	0.201	0.224	0.291	0.126	0.350	0.409	0.311	198.9
K5	0.382	0.425	0.256	0.402	0.433	0.260	0.378	0.382	0.189	0.441	0.496	0.370	217.4
K6	0.402	0.413	0.268	0.374	0.398	0.240	0.366	0.378	0.185	0.472	0.476	0.390	271.8
K7	0.531	0.433	0.323	0.492	0.469	0.319	0.492	0.406	0.224	0.559	0.500	0.445	362.6
K8	0.500	0.476	0.331	0.457	0.476	0.327	0.465	0.429	0.228	0.579	0.543	0.449	353.4
K9	0.496	0.551	0.343	0.555	0.484	0.346	0.587	0.567	0.287	0.606	0.622	0.520	368.0
K10	0.205	0.283	0.146	0.209	0.331	0.154	0.213	0.248	0.110	0.299	0.394	0.244	186.8
K11	0.287	0.417	0.197	0.307	0.421	0.217	0.260	0.394	0.150	0.390	0.516	0.307	239.0
K12	0.339	0.429	0.248	0.346	0.445	0.252	0.382	0.445	0.205	0.504	0.555	0.386	304.2
K13	0.512	0.634	0.362	0.457	0.650	0.350	0.461	0.528	0.244	0.567	0.760	0.492	333.4
K14	0.469	0.630	0.358	0.528	0.598	0.370	0.555	0.606	0.287	0.634	0.724	0.528	308.9
K15	0.650	0.815	0.484	0.669	0.913	0.508	0.760	0.713	0.350	0.783	1.094	0.681	369.6

Table 4. Measured Weld Sizes of T- and X-Connections and Failure Loads of Welded Joints													
Connection Number	Weld 1 (in.)			Weld 2 (in.)			Weld 3 (in.)			Weld 4 (in.)			Joint Failure Load (kips)
	w_b	w_c	t_w	w_b	w_c	t_w	w_b	w_c	t_w	w_b	w_c	t_w	
T1	0.205	0.264	0.157	0.205	0.256	0.142	0.189	0.260	0.142	0.244	0.220	0.154	118.5
T2	0.244	0.319	0.185	0.232	0.291	0.169	0.280	0.319	0.209	0.244	0.287	0.181	154.4
T3	0.213	0.248	0.146	0.197	0.185	0.130	0.154	0.220	0.126	0.201	0.244	0.134	203.9
T4	0.252	0.287	0.181	0.256	0.299	0.185	0.256	0.291	0.161	0.220	0.299	0.165	195.1
X1 upper	0.256	0.272	0.177	0.291	0.319	0.205	0.307	0.315	0.213	0.398	0.465	0.295	did not fail
X1 lower	0.213	0.291	0.154	0.228	0.295	0.173	0.291	0.343	0.224	0.457	0.539	0.378	310.2
X2 upper	0.217	0.276	0.165	0.220	0.276	0.165	0.244	0.315	0.189	0.248	0.287	0.193	did not fail
X2 lower	0.232	0.299	0.177	0.256	0.283	0.185	0.307	0.358	0.213	0.295	0.311	0.244	200.7
X3 upper	0.185	0.260	0.146	0.213	0.252	0.165	0.232	0.311	0.173	0.244	0.260	0.165	149.0
X3 lower	0.209	0.264	0.150	0.189	0.280	0.146	0.224	0.299	0.185	0.209	0.157	0.114	did not fail
X4 upper	0.157	0.244	0.134	0.189	0.256	0.146	0.209	0.244	0.138	0.280	0.291	0.224	104.3
X4 lower	0.213	0.283	0.157	0.169	0.252	0.138	0.209	0.217	0.122	0.276	0.287	0.224	did not fail
X5 upper	0.189	0.232	0.126	0.213	0.244	0.150	0.189	0.232	0.126	0.217	0.283	0.177	did not fail
X5 lower	0.177	0.236	0.138	0.154	0.240	0.126	0.161	0.181	0.106	0.232	0.280	0.193	95.3
X6 upper	0.181	0.205	0.130	0.177	0.217	0.130	0.213	0.201	0.134	0.177	0.256	0.150	96.9
X6 lower	0.181	0.224	0.134	0.209	0.256	0.157	0.181	0.201	0.130	0.185	0.236	0.142	did not fail
X7 upper	0.291	0.283	0.201	0.299	0.311	0.217	0.374	0.402	0.260	0.559	0.567	0.469	did not fail
X7 lower	0.287	0.307	0.201	0.303	0.299	0.213	0.276	0.429	0.224	0.512	0.531	0.425	571.2
X8 upper	0.295	0.287	0.205	0.311	0.311	0.224	0.315	0.366	0.236	0.295	0.315	0.232	380.4
X8 lower	0.311	0.303	0.217	0.283	0.295	0.201	0.315	0.346	0.224	0.295	0.319	0.240	did not fail
X9 upper	0.295	0.272	0.201	0.307	0.327	0.220	0.319	0.307	0.220	0.287	0.319	0.224	did not fail
X9 lower	0.307	0.299	0.217	0.327	0.327	0.232	0.256	0.311	0.201	0.260	0.299	0.205	310.2
X10 upper	0.232	0.248	0.169	0.228	0.236	0.165	0.232	0.240	0.142	0.283	0.327	0.236	did not fail
X10 lower	0.240	0.276	0.189	0.232	0.248	0.173	0.205	0.264	0.130	0.276	0.350	0.228	218.5
X11 upper	0.224	0.236	0.161	0.260	0.295	0.197	0.236	0.268	0.165	0.264	0.295	0.213	197.8
X11 lower	0.256	0.248	0.177	0.248	0.260	0.181	0.252	0.260	0.161	0.264	0.287	0.220	did not fail
X12 upper	0.220	0.244	0.169	0.236	0.228	0.161	0.173	0.224	0.130	0.205	0.244	0.154	196.3
X12 lower	0.236	0.228	0.161	0.248	0.240	0.173	0.165	0.244	0.130	0.220	0.248	0.169	did not fail
Note: "upper" and "lower" denote the upper or the lower branch members.													

EXPERIMENTS ON HSS WELDS

Two large-scale, 39.4-ft (12.0-m) and 40.0-ft (12.2-m) span, simply supported, fillet-welded, rectangular HSS Warren trusses, comprised of 60° gapped and overlapped K-connections, were tested by Frater and Packer (1992a, 1992b). Quasi-static loading was performed in a carefully controlled manner (Figure 1a) to produce sequential failure of the tension-loaded, fillet-welded joints (rather than connection failures). Measured geometric properties of these two trusses are given in Table 1, along with measured mechanical properties of both the (as-deposited) weld metal and HSS members. In addition, a series of weld-critical tests have been performed (Packer and Cassidy, 1995) on four T-connections and 12 cross- (or X-) connections, with the branches loaded in quasi-static tension. The measured geometric and mechanical properties of these test specimens are given in Table 2.

Weld sizes in all of the preceding connections were determined by making a negative mold of each test specimen and then measuring the leg sizes and throat sizes of each weld at multiple points. The effective leg sizes of the welds, measured along the branch member and chord member, respectively (w_b and w_c), plus the throat sizes (t_w), are listed in

Table 5. Values of ϕ, Ω, F_{nBM}, F_{nw}, A_{BM} and A_{we} for Fillet Welds				
Load Type	**Pertinent Metal**	**ϕ and Ω**	**F_{nBM} or F_{nw}**	**A_{BM} or A_{we}**
Shear	Base metal	$\phi = 0.75$ $\Omega = 2.00$	$F_{nBM} = 0.60F_{ub}$ or $F_{nBM} = 0.60F_u$	$A_{BM} = L_e w_b$ or $A_{BM} = L_e w_c$
	Weld metal	$\phi = 0.75$ $\Omega = 2.00$	$F_{nw} = 0.60F_{EXX}$	$A_{we} = L_e t_w$

Tables 3 and 4. Each separate weld size is reported as an average for weld 1, weld 2, weld 3 and weld 4, according to the notation in Figure 4. Tables 3 and 4 also list the failure loads of all welded joints, which are subsequently used to evaluate nominal weld strengths and predicted weld design strengths according to the 2010 AISC *Specification*.

WELD DESIGN PROCEDURE TO AISC 2010 SPECIFICATION

Section J2.4 of the AISC *Specification* (AISC, 2010) requires that the design strength, ϕR_n, and the allowable strength, R_n/Ω, of welded joints be the lower value of the base material strength (determined according to the limit states of tensile rupture and shear rupture) and the weld metal strength (determined according to the limit state of rupture) as follows:

For the base metal

$$R_n = F_{nBM} A_{BM} \tag{15a}$$

For the weld metal

$$R_n = F_{nw} A_{we} \tag{15b}$$

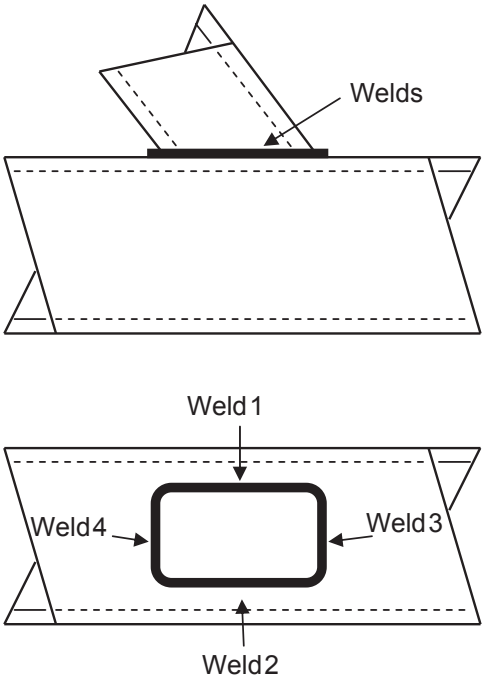

Fig. 4. Weld notation.

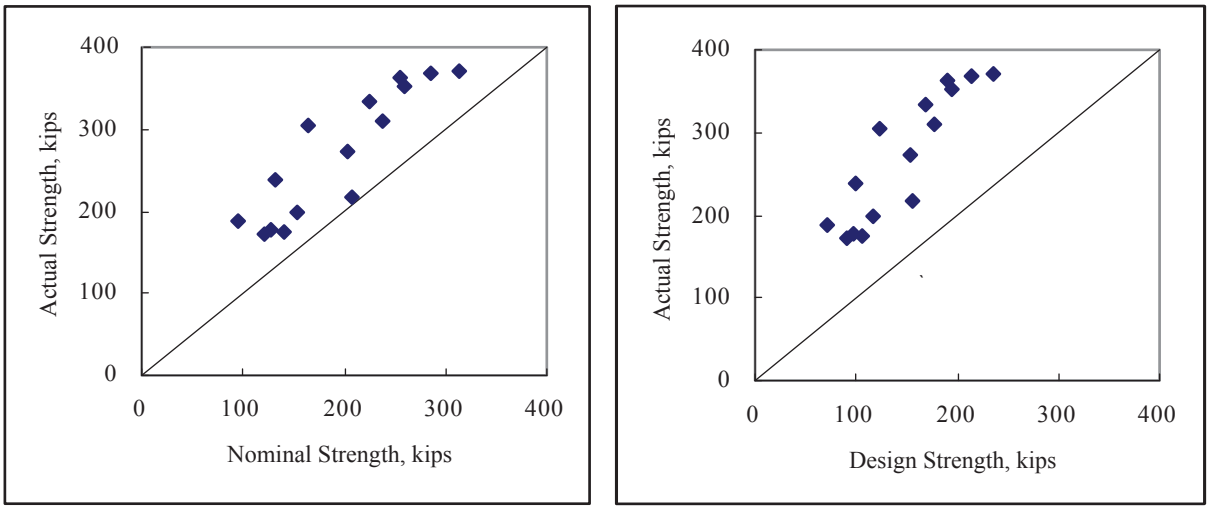

Fig. 5. Correlation with test results for gapped K-connection test specimens, without inclusion of the $(1.00 + \sin^{1.5}\theta)$ term: (a) actual strength vs. predicted nominal strength; (b) actual strength vs. predicted LRFD design strength.

Table 6. Actual Strengths, Nominal Strengths (R_n) and Predicted Resistances (ϕR_n) of Welded Joints in Gapped K-Connection Test Specimens, without Inclusion of the ($1.00 + \sin^{1.5}\theta$) Term								
Connection Number	R_{nbb} (kips)	R_{nbc} (kips)	R_{nw} (kips)	R_n (kips)	ϕR_n (kips)	Actual (kips)	Actual/R_n	Actual/(ϕR_n)
K1	142.9	154.8	121.5	121.5	91.2	171.1	1.407	1.877
K2	140.5	172.2	128.6	128.6	96.4	177.6	1.381	1.842
K3	155.5	195.3	141.4	141.4	106.1	175.8	1.243	1.657
K4	172.7	191.6	154.3	154.3	115.7	198.9	1.289	1.719
K5	252.0	272.9	206.9	206.9	155.2	217.4	1.051	1.401
K6	247.8	261.3	203.5	203.5	152.6	271.8	1.336	1.781
K7	328.9	287.5	254.6	254.6	191.0	362.6	1.424	1.899
K8	308.3	304.0	260.5	260.5	195.3	353.4	1.357	1.809
K9	353.7	350.4	285.6	285.6	214.2	368.0	1.288	1.718
K10	140.1	192.1	95.7	95.7	71.8	186.8	1.952	2.603
K11	192.1	273.3	131.6	131.6	98.7	239.0	1.815	2.420
K12	238.1	291.8	164.2	164.2	123.2	304.2	1.852	2.470
K13	320.5	403.2	224.0	224.0	168.0	333.4	1.488	1.984
K14	346.1	406.2	236.9	236.9	177.7	308.9	1.304	1.738
K15	463.4	543.4	314.1	314.1	235.6	369.6	1.177	1.569

The values of ϕ, Ω, F_{nBM}, F_{nw}, A_{BM} and A_{we} for different types of welds are given in Table J2.5 of the AISC *Specification* (AISC, 2010). Because all the welded joints in the HSS connection test specimens listed in Tables 1 through 4 were considered to be fillet-welded and loaded in shear, the part for fillet welds is abstracted from Table J2.5 and Section J4 and is given for both Load and Resistance Factor Design (LRFD) and Allowable Stress Design (ASD) in Table 5.

It should be noted that the LRFD weld and base metal resistances for the AISC *Specification* (AISC, 2010), determined using Equations 15a and 15b (in conjunction with Table 5), are the same as the Limit States Design (LSD) weld and base metal resistances calculated using CSA (2009), because the ϕF_{nw} terms $(\phi = 0.75)(0.60F_{EXX})$ and $(\phi = 0.67)(0.67F_{EXX})$ both equal $0.45F_{EXX}$. Thus, the use of either AISC or CSA formulations results in the same design outcome.

EVALUATION OF AISC 2010 *SPECIFICATION* WITH EXPERIMENTS ON HSS WELDS

Table 5 and Equations 6, 9, 14 and 15 were used to calculate the nominal strengths (excluding the resistance factor) of the 31 welded joints in Tables 1 through 4. Although weld metal strength may be expected to typically govern in a design situation, the analysis of laboratory tests—where weld and base metal strengths vary considerably—requires the strength calculation for both weld metal failure and base metal failure. The predicted strength of each welded joint, without consideration of the $(1.00 + \sin^{1.5}\theta)$ effect, was determined by the summation of the strengths of the four separate welds (see Figure 4)—that together add up to the perimeter around the branch footprint—and is given as a predicted nominal strength, R_n, in Table 6 (for gapped K-connections) and Table 7 (for T- and X-connections). The predicted nominal strength, R_n, is taken as the lowest of the values for the branch base metal (R_{nbb}), the chord base metal (R_{nbc}) and the weld metal (R_{nw}). Here, R_{nw} governed over R_{nbb} and R_{nbc} in all cases. These tables also show the predicted welded joint design strength, ϕR_n, using $\phi = 0.75$.

The correlations between the actual strengths and predicted nominal strengths, and between the actual strengths and predicted design strengths, are shown in Figure 5 (for gapped K-connection test specimens) and Figure 6 (for T-and X-connection test specimens). For gapped K-connections, the Mean of the (Actual/R_n) ratios given in Table 6, and shown in Figure 5a, is 1.424 with a coefficient of variation (COV) of 0.180. For T- and X-connections, the mean of the (actual/R_n) ratios given in Table 7, and shown in Figure 6a, is 1.153 with a COV of 0.136.

To assess whether adequate, or excessive, safety margins are inherent in the correlations shown in Figures 5a and 6a, one can check to ensure that a minimum safety index of $\beta^+ = 4.0$ (per Chapter B of the AISC *Specification* Commentary) is achieved, using a simplified reliability analysis in which the resistance factor ϕ is given by (Fisher et al., 1978; Ravindra and Galambos, 1978):

$$\phi = m_R \exp(-\alpha\beta^+ \mathrm{COV}) \quad (16)$$

Table 7. Actual Strengths, Nominal Strengths (R_n) and Predicted Resistances (ϕR_n) of Welded Joints in T- and X-Connection Test Specimens, without Inclusion of the ($1.00 + \sin^{1.5}\theta$) Term								
Connection Number	**R_{nbb} (kips)**	**R_{nbc} (kips)**	**R_{nw} (kips)**	**R_n (kips)**	**ϕR_n (kips)**	**Actual (kips)**	**Actual/ R_n**	**Actual/ (ϕR_n)**
T1	147.6	127.2	100.8	100.8	75.6	118.5	1.175	1.567
T2	173.5	152.1	122.9	122.9	92.2	154.4	1.257	1.675
T3	158.3	160.3	134.7	134.7	101.0	203.9	1.514	2.018
T4	199.2	214.4	177.2	177.2	132.9	195.1	1.101	1.468
X1 upper	352.4	268.7	235.5	235.5	176.6	did not fail	—	—
X1 lower	300.7	273.9	216.4	216.4	162.3	310.2	1.434	1.912
X2 upper	224.0	197.4	162.2	162.2	121.6	did not fail	—	—
X2 lower	255.1	210.8	181.0	181.0	135.8	200.7	1.109	1.479
X3 upper	180.4	160.5	131.3	131.3	98.5	149.0	1.135	1.514
X3 lower	176.3	160.6	122.7	122.7	92.0	did not fail	—	—
X4 upper	150.3	141.4	112.6	112.6	84.4	104.3	0.926	1.235
X4 lower	160.6	146.9	115.7	115.7	86.8	did not fail	—	—
X5 upper	149.7	127.1	100.0	100.0	75.0	did not fail	—	—
X5 lower	128.9	123.6	96.5	96.5	72.4	95.3	0.987	1.317
X6 upper	131.6	108.7	90.9	90.9	68.2	96.9	1.066	1.421
X6 lower	137.8	118.5	97.9	97.9	73.4	did not fail	—	—
X7 upper	510.2	476.1	461.0	461.0	345.8	did not fail	—	—
X7 lower	489.7	482.1	444.0	444.0	333.0	571.2	1.286	1.715
X8 upper	388.4	362.8	348.7	348.7	261.6	380.4	1.091	1.454
X8 lower	382.5	360.8	340.7	340.7	255.5	did not fail	—	—
X9 upper	337.6	311.5	297.6	297.6	223.2	did not fail	—	—
X9 lower	338.0	320.1	305.1	305.1	228.8	310.2	1.017	1.356
X10 upper	209.9	204.7	190.2	190.2	142.6	did not fail	—	—
X10 lower	211.6	221.4	201.0	201.0	150.8	218.5	1.087	1.449
X11 upper	203.4	206.3	188.1	188.1	141.1	197.8	1.052	1.402
X11 lower	211.3	197.8	188.5	188.5	141.4	did not fail	—	—
X12 upper	177.5	174.4	161.0	161.0	120.7	196.3	1.219	1.625
X12 lower	187.1	174.8	164.1	164.1	123.1	did not fail	—	—
Note: "upper" and "lower" denote the upper or the lower branch members.								

where m_R = mean of the ratio: (actual element strength)/(nominal element strength = R_n); COV = associated coefficient of variation of this ratio; and α = coefficient of separation taken to be 0.55 (Ravindra and Galambos, 1978). Equation 16 neglects variations in material properties, geometric parameters and fabrication effects, relying solely on the so-called professional factor. In the absence of reliable statistical data related to welds, this is believed to be a conservative approach. Application of Equation 16 produced $\phi = 0.959$ for welded joints in gapped K-connections and $\phi = 0.855$ for T- and X-connections. Because both of these exceed 0.75, the effective weld length concepts advocated in Section K4 of the *Specification* can, on the basis of the available experimental evidence, be deemed adequately conservative.

Introduction of the ($1.00 + 0.50 \sin^{1.5}\theta$) Term

The AISC *Specification* (AISC, 2010) and the recent Canadian *Standard* (CSA, 2009)—like their preceding editions—permit a greater available strength for a fillet weld, when loaded at an angle of θ relative to the longitudinal axis of the weld, to be taken into account in weld design, where

applicable, by using Equation 17. Conservatively, one is allowed to set the function $(1.00 + 0.50 \sin^{1.5} \theta)$ to unity.

$$F_{nw} = 0.60 F_{EXX} (1.00 + 0.50 \sin^{1.5} \theta) \quad (17)$$

The AISC *Specification* (AISC, 2010) notes, in Section J2.4, that Equation 17 is applicable only for fillet welds in a weld group that:

1. Is linear (a group in which all elements are in a line or are parallel), with a uniform leg size, and loaded through the center of gravity; or
2. Is loaded and analyzed using an instantaneous center of rotation method.

Thus, the strength enhancement of Equation 17 is not deemed appropriate for the simple design method for fillet welds to HSS branches, as described herein. This policy is also evident in the recent AISC *Design Guide* on HSS connections (Packer et al., 2010). The effect of including the $\sin \theta$ effect in fillet weld design formulas for rectangular HSS-to-HSS connections was last considered by Packer (1995), but since that time the AISC *Specification* design equations for weld effective length have evolved, as explained previously. If this $\sin \theta$ effect is taken into consideration for all branch fillet welds 1 through 4 (see Figure 4) in the analysis of the data presented in this paper, the statistical outcomes change to:

- For gapped K-connections: $m_R = 1.127$, COV = 0.145 and $\phi = 0.819$ (using Equation 16 with $\beta^+ = 4.0$).
- For T- and X-connections: $m_R = 0.998$, COV = 0.142 and $\phi = 0.730$ (using Equation 16 with $\beta^+ = 4.0$).

CONCLUSIONS

Design guides or specifications/codes requiring the welds to develop the yield capacity of the branch members produce a conservative yet easy design process, but they may lead to extra cost due to weld overdesign. Alternate design methods that consider an effective weld length have the potential to provide a relatively smaller weld size, thus achieving a more economical weld design.

By comparing the actual strengths of fillet-welded joints in weld-critical T-, cross- (X-) and gapped K-connection specimens to their predicted nominal strengths and predicted design strengths, it has been shown that the relevant effective-length design formulas in the AISC *Specification* Section K4 (AISC, 2010)—without use of the $(1.00 + 0.50 \sin^{1.5} \theta)$ term for fillet welds—result in an appropriate weld design with an adequate safety level. The effective-length design formulas for gapped K-connections, even with the $(1.00 + 0.50 \sin^{1.5} \theta)$ term included for fillet welds, were also shown to be conservative. However, the effective-length formulas for T- and cross- (X-) connections, with the $(1.00 + 0.50 \sin^{1.5} \theta)$ term included for fillet welds, currently result in an inadequate reliability index.

A limitation of this study is that all test specimens were under predominantly axial loads in the branches. However, the weld effective length formulas for T-, Y- and cross- (X-) connections in *Specification* Table K4.1 (AISC, 2010) also address branch bending. The available test data do not provide an opportunity to evaluate the accuracy of formulas applicable to branch bending loads. Thus, the general use of the $(1.00 + 0.50 \sin^{1.5} \theta)$ strength enhancement term for fillet welds in HSS-to-HSS connections is not recommended.

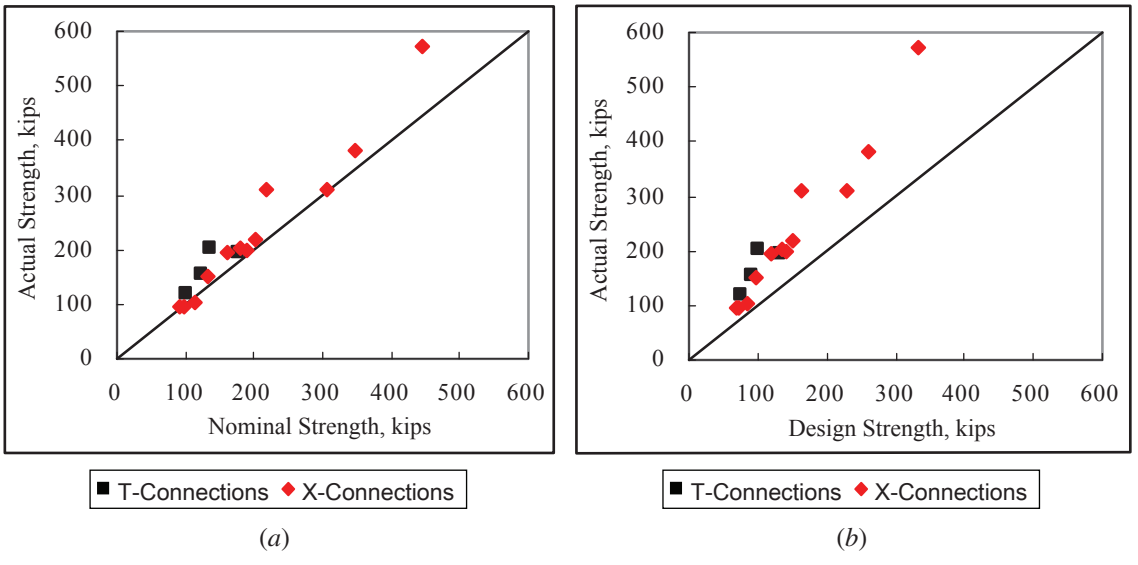

Fig. 6. Correlation with test results for T- and X-connection test specimens, without inclusion of the $(1.00 + \sin^{1.5} \theta)$ term: (a) actual strength vs. predicted nominal strength; (b) actual strength vs. predicted LRFD design strength.

DESIGN EXAMPLES

Two design examples follow, using square and rectangular ASTM A500 HSS (ASTM, 2010). These examples illustrate the *Specification* Section K4 (AISC, 2010) weld design method for square and rectangular HSS, with the examples performed in both LRFD and ASD and presented to AISC format (Packer et al., 2010).

Design Example for a T-Connection

Given:

Determine the weld size to connect the square HSS branch member to the square HSS chord member to resist the applied load as shown in Figure 7. The dead and live loads on the branch member are $P_D = 20$ kips and $P_L = 20$ kips.

The material properties are as follows:
HSS chord member: ASTM A500 Grade B steel, $F_y = 46$ ksi, $F_u = 58$ ksi
HSS branch member: ASTM A500 Grade B steel, $F_{yb} = 46$ ksi, $F_{ub} = 58$ ksi
Electrode E70: $F_{E70} = 70$ ksi

The geometric properties are as follows:
HSS $10 \times 10 \times ½$: $H = B = 10$ in., $t = 0.465$ in.
HSS $5 \times 5 \times ⅜$: $H_b = B_b = 5$ in., $t_b = 0.349$ in.
Branch member inclination angle: $\theta = 90°$

Solution:

Calculate the required strength

LRFD	ASD
$P_r = 1.2(20 \text{ kips}) + 1.6(20 \text{ kips})$ $= 56$ kips	$P_r = 20 \text{ kips} + 20 \text{ kips}$ $= 40$ kips

The T-connection in the design example meets all the limits of applicability of Table K2.2A in the *Specification* (AISC, 2010). The available axial strength of the T-connection, determined by applying the formulas in Table K2.2, also exceeds the required strength.

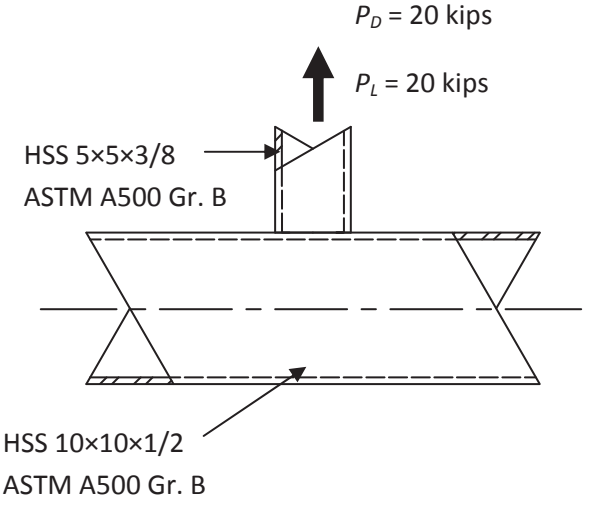

Fig. 7. Design example for a T-connection.

Calculate the effective weld length

Apply Equation 9 to determine the effective width of the branch weld transverse to the chord:

$$b_{eoi} = \frac{10}{B/t}\left(\frac{F_y t}{F_{yb} t_b}\right) B_b$$
$$= \frac{10}{10 \text{ in.}/0.465 \text{ in.}}\left(\frac{46 \text{ ksi}\,(0.465 \text{ in.})}{46 \text{ ksi}\,(0.349 \text{ in.})}\right)(5 \text{ in.})$$
$$= 3.10 \text{ in.} \le B_b = 5 \text{ in.}$$

Apply Equation 6 to determine the effective weld length for resisting the applied load:

$$L_e = \frac{2H_b}{\sin\theta} + 2b_{eoi} = \frac{2(5 \text{ in.})}{\sin 90°} + 2(3.10 \text{ in.}) = 16.20 \text{ in.}$$

Determine the required weld size

Section J2.4 of the *Specification* (AISC, 2010) requires the design strength, ϕR_n, and the allowable strength, R_n/Ω, of welded joints to be the lower value of the base material strength (determined according to the limit states of tensile rupture and shear rupture) and the weld metal strength (determined according to the limit state of rupture). In other words, R_n shall be the least value among the nominal strength of the branch member base metal (R_{nbb}), the nominal strength of the chord member base metal (R_{nbc}) and the nominal strength of the weld metal (R_{nw}).

Let $w_b = w_c = w$, where w is the required weld size (leg).

- For the branch member base metal

  $R_{nbb} = F_{nBM} A_{BM}$ — Equation 15a
  $= (0.6F_{ub})(L_e w_b)$ — Table 5
  $= (0.6 \times 58 \text{ ksi})(16.20 \text{ in.} \times w)$
  $= 563.8w$ kips

- For the chord member base metal

  $R_{nbc} = F_{nBM} A_{BM}$ — Equation 15a
  $= (0.6F_u)(L_e w_c)$ — Table 5
  $= (0.6 \times 58 \text{ ksi})(16.20 \text{ in.} \times w)$
  $= 563.8w$ kips

- For the weld metal

  For all four sides of weld, $t_w = w\sqrt{2}$, as all welds are 90° fillets.
  $R_{nw} = F_{nw} A_{we}$ — Equation 15b
  $= (0.6F_{EXX})(L_e t_w)$ — Table 5
  $= (0.6 \times 70 \text{ ksi})(16.20 \text{ in.} \times w\sqrt{2})$
  $= 481.1w$ kips

Thus, $R_n = \min R_{nbb}, R_{nbc}, R_{nw} = \min 563.8w$ kips, $563.8w$ kips, $481.1w$ kips $= 481.1w$ kips. In other words, the weld metal controls, as is expected, even considering all base metals as loaded in shear.

LRFD	ASD
$\phi = 0.75$ $\phi R_n \geq P_r = 56$ kips $0.75(481.1w \text{ kips}) \geq 56$ kips $w \geq 0.155$ in. Hence, use 3⁄16-in. weld.	$\Omega = 2.00$ $R_n/\Omega \geq P_r = 40$ kips $481.1w \text{ kips} / 2.00 \geq 40$ kips $w \geq 0.166$ in. Hence, use 3⁄16-in. weld.

The 3⁄16-in. weld is placed all around the joint. Check that fillet welding along the longitudinal sides of the branch is still possible on the "flat" of the HSS chord connecting face.

Minimum width of HSS "flat" $\approx B - 2(3t)$

$= 10.0 \text{ in.} - 2(3 \times 0.465 \text{ in.})$

$= 7.21 \text{ in.} > 5.0 \text{ in.} + 2(3⁄16 \text{ in.})$

$= 5.38$ in. **o.k.**

Design Example for a Gapped K-Connection

Given:

Determine the weld size to connect the square HSS branch member to the rectangular HSS chord member to resist the applied loads as shown in Figure 8. The dead and live loads on each branch member are P_D = 20 kips and P_L = 20 kips.

The material properties are as follows:
HSS chord member: ASTM A500 Grade B steel, $F_y = 46$ ksi, $F_u = 58$ ksi
HSS branch member: ASTM A500 Grade B steel, $F_{yb} = 46$ ksi, $F_{ub} = 58$ ksi
Electrode E70: $F_{E70} = 70$ ksi

The geometric properties are as follows:
HSS 12 × 8 × ½: $H = 12$ in., $B = 8$ in., $t = 0.465$ in.
HSS 4 × 4 × ⅜: $H_b = B_b = 4$ in., $t_b = 0.349$ in.
Branch member inclination angle: $\theta = 60°$

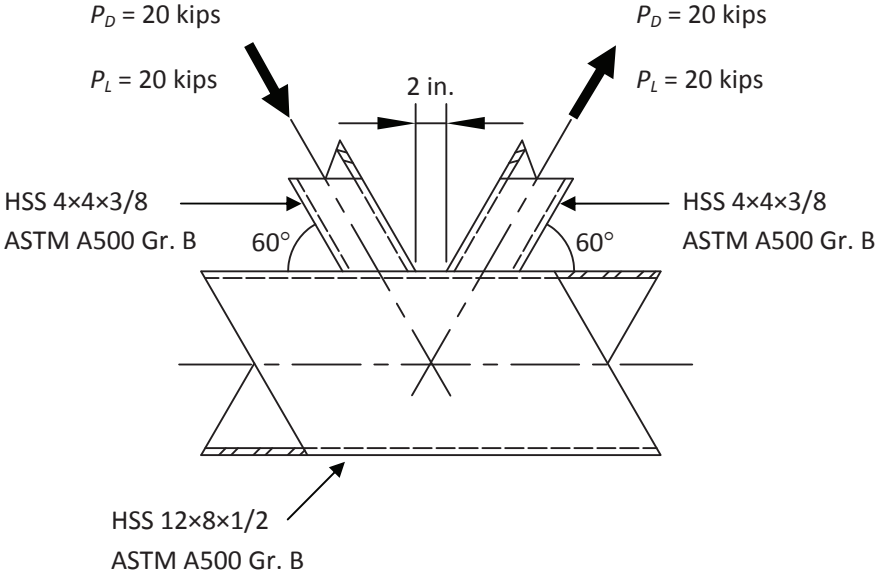

Fig. 8. Design example for a gapped K-connection.

Solution:

Calculate the required strength

LRFD	ASD
$P_r = 1.2(20 \text{ kips}) + 1.6(20 \text{ kips})$ $= 56 \text{ kips}$	$P_r = 20 \text{ kips} + 20 \text{ kips}$ $= 40 \text{ kips}$

The gapped K-connection in the design example meets all the limits of applicability of Table K2.2A in the *Specification* (AISC, 2010). The available axial strength of the gapped K-connection, determined by applying the formulas in Table K2.2, also exceeds the required strength.

Calculate the effective weld lengths

Apply Equation 14b to determine the effective weld lengths for one branch member. For the two longitudinal side welds:

$$L_e = \frac{2(H_b - 1.2t_b)}{\sin\theta} = \frac{2\left[4 \text{ in.} - (1.2)(0.349 \text{ in.})\right]}{\sin 60°} = 8.27 \text{ in.}$$

For the transverse toe weld:

$$L_e = (B_b - 1.2t_b) = (4 \text{ in.} - 1.2 \times 0.349 \text{ in.}) = 3.58 \text{ in.}$$

Note that this effective length assumes that the weld at the heels of both branches is totally ineffective, at this branch angle.

Determine the required weld size

Section J2.4 of the *Specification* (AISC, 2010) requires the design strength, ϕR_n, and the allowable strength, R_n/Ω, of welded joints to be the lower value of the base material strength (determined according to the limit states of tensile rupture and shear rupture) and the weld metal strength (determined according to the limit state of rupture). In other words, R_n shall be the least value among the nominal strength of the branch member base metal (R_{nbb}), the nominal strength of the chord member base metal (R_{nbc}) and the nominal strength of the weld metal (R_{nw}).

Assume that a common effective weld size is placed all around each branch. Try ¼-in. weld ($= w_b = w_c$) for weld 1 and weld 2 as shown in Figure 4.

- For weld 1 and weld 2 branch member base metal

  $R_{nbb} = F_{nBM} A_{BM}$ — Equation 15a
  $= (0.6F_{ub})(L_e w_b)$ — Table 5
  $= (0.6 \times 58 \text{ ksi})(8.27 \text{ in.} \times 0.25 \text{ in.})$
  $= 71.9 \text{ kips}$

- For weld 1 and weld 2 chord member base metal

  $R_{nbc} = F_{nBM} A_{BM}$ — Equation 15a
  $= (0.6F_u)(L_e w_c)$ — Table 5
  $= (0.6 \times 58 \text{ ksi})(8.27 \text{ in.} \times 0.25 \text{ in.})$
  $= 71.9 \text{ kips}$

- For weld 1 and weld 2 weld metal

  For weld 1 and weld 2 (see Figure 4), the angle between the branch face and the chord face is 90°, so $t_w = w\sqrt{2}$
  $= 0.177 \text{ in.}$

  $R_{nw} = F_{nw} A_{we}$ — Equation 15b
  $= (0.6F_{EXX})(L_e t_w)$ — Table 5
  $= (0.6 \times 70 \text{ ksi})(8.27 \text{ in.} \times 0.177 \text{ in.})$
  $= 61.5 \text{ kips}$

Thus, R_n = min R_{nbb}, R_{nbc}, R_{nw} = min 71.9 kips, 71.9 kips, 61.5 kips = 61.5 kips for (weld 1 + weld 2). In other words, the weld metal controls, as is expected, even considering all base metals as loaded in shear.

Now consider weld 3 (see Figure 4). To maintain a weld effective throat of t_w = 0.177 in., $w_b = w_c$ = 0.354 in. for weld 3.

- For weld 3 branch member base metal

$R_{nbb} = F_{nBM} A_{BM}$ Equation 15a
$= (0.6F_{ub})(L_e w_b)$ Table 5
$= (0.6 \times 58 \text{ ksi})(3.58 \text{ in.} \times 0.354 \text{ in.})$
$= 44.1$ kips

- For weld 3 chord member base metal

$R_{nbc} = F_{nBM} A_{BM}$ Equation 15a
$= (0.6F_u)(L_e w_c)$ Table 5
$= (0.6 \times 58 \text{ ksi})(3.58 \text{ in.} \times 0.354 \text{ in.})$
$= 44.1$ kips

- For weld 3 weld metal

$R_{nw} = F_{nw} A_{we}$ Equation 15b
$= (0.6F_{EXX})(L_e t_w)$ Table 5
$= (0.6 \times 70 \text{ ksi})(3.58 \text{ in.} \times 0.177 \text{ in.})$
$= 26.6$ kips

Thus, R_n = min R_{nbb}, R_{nbc}, R_{nw} = min 44.1 kips, 44.1 kips, 26.6 kips = 26.6 kips for weld 3. In other words, the weld metal controls, as is expected, even considering all base metals as loaded in shear.

Thus, for (weld 1 + weld 2 + weld 3), R_n = 61.5 kips + 26.6 kips = 88.1 kips. Note that when $\theta \geq 60°$, weld 4 at the branch heel is not effective in resisting the applied load according to Equation 14b.

LRFD	ASD
$\phi = 0.75$	$\Omega = 2.00$
$\phi R_n = 0.75(88.1 \text{ kips}) = 66.1$ kips	$R_n/\Omega = 88.1 \text{ kips}/ 2.00 = 44.1$ kips
$P_r = 56$ kips $< \phi R_n$ **o.k.**	$P_r = 40$ kips $< R_n/\Omega$ **o.k.**
Hence, use ¼-in. weld.	Hence, use ¼-in. weld.

The fillet weld is placed all around the joint. Calculations can sometimes lead to slightly different answers for LRFD and ASD, depending on the live-to-dead load ratio. LRFD and ASD procedures are calibrated to yield the same result for a live-to-dead load ratio of 3:1. Check that the fillet welding along the longitudinal sides of the branch is still possible on the "flat" of the HSS chord connecting face.

Minimum width of HSS "flat" $\approx B - 2(3t)$
$= 8.0 \text{ in.} - 2(3 \times 0.465 \text{ in.})$
$= 5.21 \text{ in.} > 4.0 \text{ in.} + 2(¼ \text{ in.})$
$= 4.5$ in. **o.k.**

SYMBOLS

A_{BM} = effective area of the base metal, in.^{2}

A_{we} = effective (throat) area of the weld, in.^{2}

B = overall width of rectangular HSS chord member, measured 90° to the plane of the connection, in.

B_b = overall width of rectangular HSS branch member, measured 90° to the plane of the connection, in.

F_{EXX} = filler metal classification strength, ksi

F_{nBM} = nominal stress of the base metal, ksi

F_{nw} = nominal stress of the weld metal, ksi

F_u = tensile strength of the HSS chord member material, ksi

F_{ub} = tensile strength of the HSS branch member material, ksi

F_{uw} = tensile strength of the weld metal, ksi

F_y = yield strength of the HSS chord member material, ksi

F_{yb} = yield strength of the HSS branch member material, ksi

H = overall height of rectangular HSS chord member, measured in the plane of the connection, in.

H_b = overall height of rectangular HSS branch member, measured in the plane of the connection, in.

I_{ip} = weld effective moment of inertia for in-plane bending, in.^{4}

I_{op} = weld effective moment of inertia for out-of-plane bending, in.^{4}

L_e = effective length of groove and fillet welds to rectangular HSS, for weld strength calculations, in.

M_{ip} = in-plane bending moment, kip-in.

M_{op} = out-of-plane bending moment, kip-in.

P_r = required strength, kips

R_n = nominal strength of the welded joint (the least value of R_{nbb}, R_{nbc} and R_{nw}), kips

R_{nbb} = nominal strength of the branch member base metal, kips

R_{nbc} = nominal strength of the chord member base metal, kips

R_{nw} = nominal strength of the weld metal, kips

S_{ip} = weld effective elastic section modulus for in-plane bending, in.^{3}

S_{op} = weld effective elastic section modulus for out-of-plane bending, in.^{3}

b_{eoi} = effective width of the transverse branch face welded to the chord, in.

m_R = mean of ratio: (actual element strength)/(nominal element strength) = professional factor

t = wall thickness of HSS chord member, in.

t_b = wall thickness of HSS branch member, in.

t_w = effective weld throat thickness, in.

w_b = effective leg size of weld, measured along the branch member, in.

w_c = effective leg size of weld, measured along the chord member, in.

α = separation factor = 0.55

β = width ratio = the ratio of overall branch width to chord width for HSS connection

β^+ = safety (reliability) index for LRFD and LSD

θ = acute angle between the branch and chord, degrees; angle of loading measured from a weld longitudinal axis for fillet weld strength calculation, degrees

ϕ = resistance factor

Ω = safety factor

REFERENCES

AISC (2010), *Specification for Structural Steel Buildings*, ANSI/AISC 360-10, American Institute of Steel Construction, Chicago, IL.

ASTM (2010), *Standard Specification for Cold-Formed Welded and Seamless Carbon Steel Structural Tubing in Rounds and Shapes*, ASTM A500/A500M-10, ASTM International, West Conshohocken, PA.

AWS (1992), *Structural Welding Code—Steel*, ANSI/AWS D1.1-92, 13th ed., American Welding Society, Miami, FL.

CEN (2005), *Eurocode 3: Design of Steel Structures—Part 1-1: General Rules and Rules for Buildings*, EN 1993-1-1:2005(E), European Committee for Standardization, Brussels, Belgium.

CSA (2009), *Design of Steel Structures*, CSA-S16-09, Canadian Standards Association, Toronto, Canada.

Davies, G. and Packer, J.A. (1982), "Predicting the Strength of Branch Plate–RHS Connections for Punching Shear," *Canadian Journal of Civil Engineering*, Vol. 9, No. 3, pp. 458–467.

Fisher, J.W., Galambos, T.V., Kulak, G.L. and Ravindra, M.K. (1978), "Load and Resistance Factor Design Criteria for Connectors," *Journal of the Structural Division*, American Society of Civil Engineers, Vol. 104, No. 9, pp. 1427–1441.

Frater, G.S. and Packer, J.A. (1992a), "Weldment Design for RHS Truss Connections. I: Applications," *Journal of Structural Engineering*, American Society of Civil Engineers, Vol. 118, No. 10, pp. 2784–2803.

Frater, G.S. and Packer, J.A. (1992b), "Weldment Design for RHS Truss Connections. II: Experimentation," *Journal of Structural Engineering*, American Society of Civil Engineers, Vol. 118, No. 10, pp. 2804–2820.

IIW (1989), *Design Recommendations for Hollow Section Joints—Predominantly Statically Loaded*, 2nd ed., IIW Doc. XV-701-89, International Institute of Welding Annual Assembly, Paris, France.

IIW (2009), *Static Design Procedure for Welded Hollow Section Joints—Recommendations*, 3rd ed., IIW Doc. XV-1329-09, International Institute of Welding Annual Assembly, Paris, France.

Miller, D.K. (2006), *Design Guide No. 21, Welded Connections—A Primer for Engineers*, American Institute of Steel Construction, Chicago, IL.

Packer, J.A. (1995), "Design of Fillet Welds in Rectangular Hollow Section T, Y and X Connections using New North American Code Provisions," *Proceedings, 3rd International Workshop on Connections in Steel Structures*, Trento, Italy, Proceedings pp. 463–472.

Packer, J.A. and Cassidy, C.E. (1995), "Effective Weld Length for HSS T, Y, and X Connections," *Journal of Structural Engineering*, American Society of Civil Engineers, Vol. 121, No. 10, pp. 1402–1408.

Packer, J.A. and Henderson, J.E. (1992), *Design Guide for Hollow Structural Section Connections*, Canadian Institute of Steel Construction, Toronto, Canada.

Packer, J.A. and Henderson, J.E. (1997), *Hollow Structural Section Connections and Trusses—A Design Guide*, 2nd ed., Canadian Institute of Steel Construction, Toronto, Canada.

Packer, J.A., Sherman, D.R. and Lecce, M. (2010), *Design Guide No. 24, Hollow Structural Section Connections*, American Institute of Steel Construction, Chicago, IL.

Packer, J.A., Wardenier, J., Zhao, X.L., van der Vegte, G.J. and Kurobane, Y. (2009), *Design Guide for Rectangular Hollow Section (RHS) Joints under Predominantly Static Loading*, CIDECT Design Guide No. 3, 2nd ed., CIDECT, Switzerland.

Ravindra, M.K. and Galambos, T.V. (1978), "Load and Resistance Factor Design for Steel," *Journal of the Structural Division*, American Society of Civil Engineers, Vol. 104, No. 9, pp. 1337–1353.

Plastic Moment of Intermediate Horizontal Boundary Elements of Steel Plate Shear Walls

BING QU and MICHEL BRUNEAU

ABSTRACT

This paper presents results of an analytical study of plastic moment in horizontal boundary elements (HBEs) in steel plate shear walls. To account for the effect of shear and vertical stresses in HBE web, the reduced axial yield strength was studied using the von Mises yield criterion. In the spirit of classic plastic analysis, analytical procedures for estimating plastic moment of the intermediate HBE under equal top and bottom tension fields are developed. Those analytical procedures are then extended for intermediate HBE under unequal top and bottom tension fields. Both positive and negative flexures are considered. Results from the analytical procedures are shown to agree well with those from finite element analysis. Simplified models for estimating plastic moment of HBEs are also developed for design and shown to be accurate.

Keywords: steel plate shear walls; horizontal boundary elements; plastic moments.

A special plate shear wall (SPSW) consists of unstiffened infill steel panels bounded by columns, called vertical boundary elements (VBEs), on both sides and beams, called horizontal boundary elements (HBEs), above and below. These panels are allowed to buckle in shear and subsequently form diagonal tension fields to resist lateral forces. Past experimental studies in the United States, Canada, Japan, Taiwan, and other countries have shown that SPSW can exhibit high initial stiffness, behave in a ductile manner and dissipate significant amounts of hysteretic energy—which make it a viable option for the design of new buildings as well as for the retrofit of existing constructions (an extensive literature review is available in Sabelli and Bruneau, 2006). Analytical research on SPSW has also validated useful models for the design and analysis of this system (e.g., Thorburn et al., 1983; Elgaaly et al., 1993; Driver et al., 1997; Berman and Bruneau, 2003b). Recent design procedures for SPSW are provided by the CSA *Limit States Design of Steel Structures* (CSA, 2009) and the AISC *Seismic Provisions for Structural Steel Buildings* (AISC, 2010). Innovative SPSW designs have also been proposed and experimentally validated to expand the range of applicability of SPSW (Berman and Bruneau, 2003a, 2003b; Vian and Bruneau, 2005).

Bing Qu, Assistant Professor, Department of Civil and Environmental Engineering, California Polytechnic State University, San Luis Obispo, CA (corresponding author). E-mail: bqu@calpoly.edu

Michel Bruneau, Professor, Department of Civil, Structural and Environmental Engineering, University at Buffalo, Buffalo, NY. E-mail: bruneau@buffalo.edu

However, this remains a relatively new structural system for seismic applications and is still the subject of much study. In particular, in an experimental study on full-scale two-story SPSWs conducted to investigate the seismic behavior of intermediate HBEs with reduced beam section (RBS) connections (Qu et al., 2008), the yield pattern of RBS in the intermediate HBE was different from expected. In conventional steel moment frames, plastic hinges are typically observed at the center of RBS. However, instead of forming at the RBS centers, the HBE plastic hinges moved toward the near column faces in the tested SPSW (i.e., developed in a zone between the RBS center and the HBE end). Likewise, similar yielding behavior of intermediate HBEs having RBS connections was consistently observed from recent experimental investigations on SPSWs (Tsai and Lee, 2007). These discrepancies in observed versus expected yielding behavior of intermediate HBE suggest that plastic moment in intermediate HBEs deserves to be further studied. Some detailed information about the aforementioned yield pattern of intermediate HBE was shown in Qu and Bruneau (2010).

Conventional simple plastic analysis procedures for determining the plastic moment of wide flange members in a steel moment frame cannot be applied to intermediate HBEs of SPSWs because the web of an HBE is under large biaxial stresses when the tension fields of the wall develop. To account for this effect—and consequently ensure predictable and ductile behavior of intermediate HBEs—analytical procedures to correctly quantify the strength of plastic hinges in HBEs subjected to axial force, shear force and vertical stresses due to infill panel forces are needed.

This paper first discusses the loading characteristics of HBE cross sections. Following a review of the classic plastic analysis procedure to calculate the plastic moment of wide flange members in steel moment frames, the reduced axial

yield strength of HBE web under shear and vertical stresses is studied using the von Mises yield criterion. Then, the analytical procedures for estimating the plastic moment of intermediate HBEs under equal and unequal top and bottom tension fields are respectively presented. Those procedures are verified by finite element (FE) examples and simplified for practical use. Finally, additional comments are given to anchor HBEs, defined in the next section. The procedures to estimate the plastic moment of intermediate HBE developed in this paper can be used in capacity design of intermediate HBEs (Qu and Bruneau, 2010).

LOADING CHARACTERISTICS OF HBE CROSS SECTIONS

In any multistory SPSW such as the one shown in Figure 1, HBEs can be classified as anchor HBEs and intermediate HBEs. Anchor HBEs are the top and bottom ends of a SPSW, and they anchor the infill panel yield forces. Because they are loaded by tension fields only on one side (either above or below), they are typically of substantial size. Intermediate HBEs are the beams at all levels other than the top and bottom of the SPSW. The variation between the top and bottom infill panel forces acting on intermediate HBE can sometimes be small (or nil) when the top and bottom infill panels of identical (or near identical) thicknesses are both yielding. Compared with the sizes of anchor HBEs, intermediate HBEs are often relatively small.

To understand the infill panel effects on HBE behavior, the aforementioned SPSW with rigid HBE-to-VBE connections is considered. The loading conditions at the ends of HBEs when the wall develops the expected plastic collapse mechanism are schematically shown in Figure 2. In this figure, τ represents the shear stress in HBE web; P and M represent the axial compression force and moment acting at HBE ends, respectively; and ω_{ybi+1} and ω_{ybi} represent the vertical components of the top and bottom infill tension fields, respectively. Mathematical expressions for ω_{ybi+1} and ω_{ybi} are given in Qu and Bruneau (2010).

Note that an HBE is typically in compression when the expected plastic mechanism of the SPSW develops as described in Qu and Bruneau (2010). The magnitudes of τ, P, and M may vary at different locations along the HBE. Although the direction of shear stress, τ, depends on the resulting shear effects due to infill tension fields and HBE flexural actions, it has no impact on HBE plastic moment as demonstrated later. Accordingly, the loading characteristics of HBE cross-sections are summarized in Table 1. Note that for the purpose of the present discussion, flexure designated as plus (+) or minus (–) respectively refers to the bending action producing tension or compression in the flange on which the greater tension field is applied. For intermediate HBEs under equal top and bottom tension fields, the acting direction of flexure has no impact on the plastic moment resistance as shown later.

PLASTIC MOMENT OF WIDE FLANGE IN MEMBER MOMENT FRAME

A well-known lower bound approach to estimate the plastic moment of wide flange member in steel moment frame, based on stress diagrams, and classic plastic analysis can be used to account for the combined interaction of flexure, axial force, and shear force (Bruneau et al. 1998). Using this procedure, the uniform shear stress, τ_w, assumed to act on

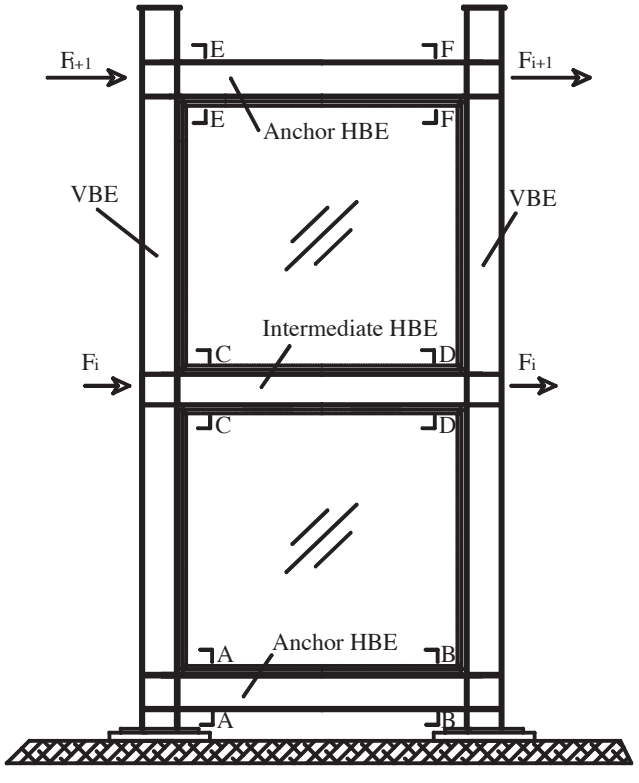

Fig. 1. A typical multistory SPSW.

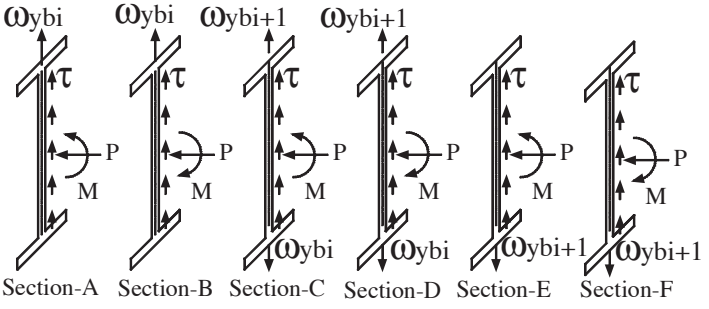

Fig. 2. Loading at HBE ends.

Table 1. Loading Characteristics of HBE Cross Sections				
HBE type	Corresponding Cross Section for Figure 1	Flexure		Ratio of Tension Fields $\omega_{yi}/\omega_{yi+1}$
		+	–	
Intermediate	C/D			1
Intermediate	C	✓		>1
Intermediate	D		✓	>1
Anchor	A		✓	0*
Anchor	B	✓		0*
Anchor	E	✓		∞**
Anchor	F		✓	∞**
*when $\omega_{yi} = 0$. ** when $\omega_{yi}+1 = 0$.				

the web of the section as a result of the applied shear force, *V*, is calculated as:

$$\tau_w = \frac{V}{h_w t_w} \tag{1}$$

where h_w and t_w are depth and thickness of the web of the cross section, respectively.

Then, the von Mises yield criterion is used to calculate the maximum axial stress, σ_w, that can be applied on the web (i.e., the remaining axial yield strength):

$$\sigma_w = \sqrt{f_y^2 - 3\tau_w^2} \tag{2}$$

where f_y is the yield strength of steel.

The strength of the flanges remains f_y. In the case where the neutral axis remains in the web, as shown in Figure 3, location of the neutral axis, y_0, is given by:

$$y_o = \frac{P}{2\sigma_w t_w} \tag{3}$$

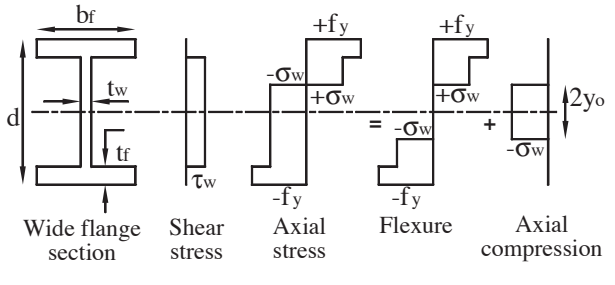

Fig. 3. Example of plastic resistance of a wide flange structural shape subjected to flexure, axial and shear forces.

Neglecting strain hardening, the plastic axial stress diagram of a typical wide flange section can be divided into pure flexural and axial contributions as shown in Figure 3. The contributions of the web and flanges to plastic moment can be calculated based on the flexural stress diagrams, respectively, as:

$$M_{pr-web}^{P,V} = \frac{t_w\left(d-2t_f\right)^2}{4}\sigma_w - \frac{t_w\left(2y_o\right)^2}{4}\sigma_w \tag{4}$$

$$M_{pr-flange}^{P,V} = b_f t_f \left(d-t_f\right) f_y \tag{5}$$

where the superscript (*P, V*) indicates that the plastic moment is reduced taking into account the applied axial and shear forces, and where b_f and t_f are the flange width and thickness of the cross section, respectively. Then, plastic moment of the cross section, $M_{pr}^{P,V}$, can be obtained as:

$$M_{pr}^{P,V} = M_{pr-web}^{P,V} + M_{pr-flange}^{P,V} \tag{6}$$

The preceding lower-bound approach, which provides acceptable results, has been used for steel moment frame design. However, for SPSWs, experimental results described in Qu et al. (2008) provide evidence that a more sophisticated procedure is warranted for intermediate HBEs. To do so, a review of the von Mises criterion in the plane stress condition is necessary and presented in the following section.

REDUCED YIELD STRENGTH IN HBE WEB

To better understand the reduced axial yield strength in an HBE web due to the presence of shear and vertical stresses, two elements are arbitrarily selected from the axial tension and compression zones of a segment of intermediate HBE

web as shown in Figure 4. These elements are in plane stress condition.

The results of classic mechanics of materials show that the von Mises yield criterion in plane stress condition can be written as:

$$\left(\frac{\sigma_x}{f_y}\right)^2-\left(\frac{\sigma_x}{f_y}\right)\left(\frac{\sigma_y}{f_y}\right)+\left(\frac{\sigma_y}{f_y}\right)^2+3\left(\frac{\tau_{xy}}{f_y}\right)^2=1 \qquad (7)$$

Equation 7 can be reorganized as a quadratic equation in terms of σ_x/f_w and solved to give the reduced axial yield strengths for given values of the other two terms:

$$\left(\frac{\sigma_x}{f_y}\right)=\frac{1}{2}\left(\frac{\sigma_y}{f_y}\right)\pm\frac{1}{2}\sqrt{4-3\left(\frac{\sigma_y}{f_y}\right)^2-12\left(\frac{\tau_{xy}}{f_y}\right)^2} \qquad (8)$$

Note that the reduced tension and compression axial yield strength can be obtained by considering the plus (+) and minus (–) solutions to Equation 8, respectively.

In the absence of vertical stress (i.e., $\sigma_y = 0$), the compression and tension axial yield strengths predicted by Equation 8 are of the same magnitude, which is

$$\left(\frac{\sigma_x}{f_y}\right)=\pm\sqrt{1-3\left(\frac{\tau_{xy}}{f_y}\right)^2} \qquad (9)$$

Note that Equation 9 is equivalent to Equation 2, which is used for estimating the plastic moment of wide flange members in steel moment frames.

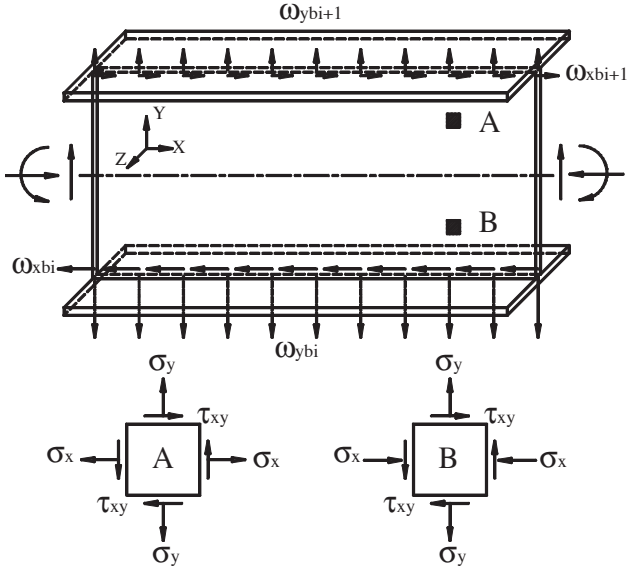

Fig. 4. Loading on the intermediate HBE segment.

The reduced tension and compression axial yield strengths, in the σ_x/f_y and σ_y/f_y space, for given values of τ_{xy}/f_y are shown in Figure 5, as a graphical representation of Equation 8. As shown, the tension and compression axial yield strengths are unequal due to the presence of vertical stresses. This is the stress condition found in the HBE web. Also note from Figure 5 that the compression axial yield strength is significantly reduced and can even become nil under the combined action of shear and vertical stresses. The tension axial yield strength is also affected by the shear and vertical stresses, but to a lesser degree. The maximum value of σ_y/f_y shown in Figure 5 is less than 1.0 in some cases (e.g., for the case of $\tau_{xy}/f_y = 0.40$) because the maximum allowable vertical stress (i.e., σ_y) is reduced due to the presences of axial and shear stresses (i.e., σ_x and τ_{xy}, respectively).

INTERMEDIATE HBE UNDER EQUAL TOP AND BOTTOM TENSION FIELDS

The plastic moment of an intermediate HBE under equal top and bottom tension fields is first discussed because this case provides some of the building blocks necessary to understand the more complex scenarios presented later.

Derivation of Plastic Moment

In the spirit of classic plastic cross-section analysis and using the reduced axial yield strength obtained from the von Mises yield criterion accounting for the vertical and shear stresses, one can generate the stress diagrams for a fully plastified HBE cross section under equal top and bottom tension fields. Note that all the equations derived in this section remain valid for cases of both flexures shown in Figure 6.

As traditionally done in structural steel for wide flange sections, uniform shear stress is assumed to act on the HBE web and is calculated according to Equation 1. In addition, a constant vertical tension stress is assumed in the HBE web as a result of the identical top and bottom tension fields, which is:

$$\sigma_y=\frac{\omega_{ybi}}{t_w} \qquad (10)$$

Consistent with Equation 8, the tension and compression axial yield strengths, σ_t and σ_c, can be calculated as:

$$\left(\frac{\sigma_t}{f_y}\right)=\frac{1}{2}\left(\frac{\sigma_y}{f_y}\right)+\frac{1}{2}\sqrt{4-3\left(\frac{\sigma_y}{f_y}\right)^2-12\left(\frac{\tau_w}{f_y}\right)^2} \qquad (11)$$

$$\left(\frac{\sigma_c}{f_y}\right)=\frac{1}{2}\left(\frac{\sigma_y}{f_y}\right)-\frac{1}{2}\sqrt{4-3\left(\frac{\sigma_y}{f_y}\right)^2-12\left(\frac{\tau_w}{f_y}\right)^2} \qquad (12)$$

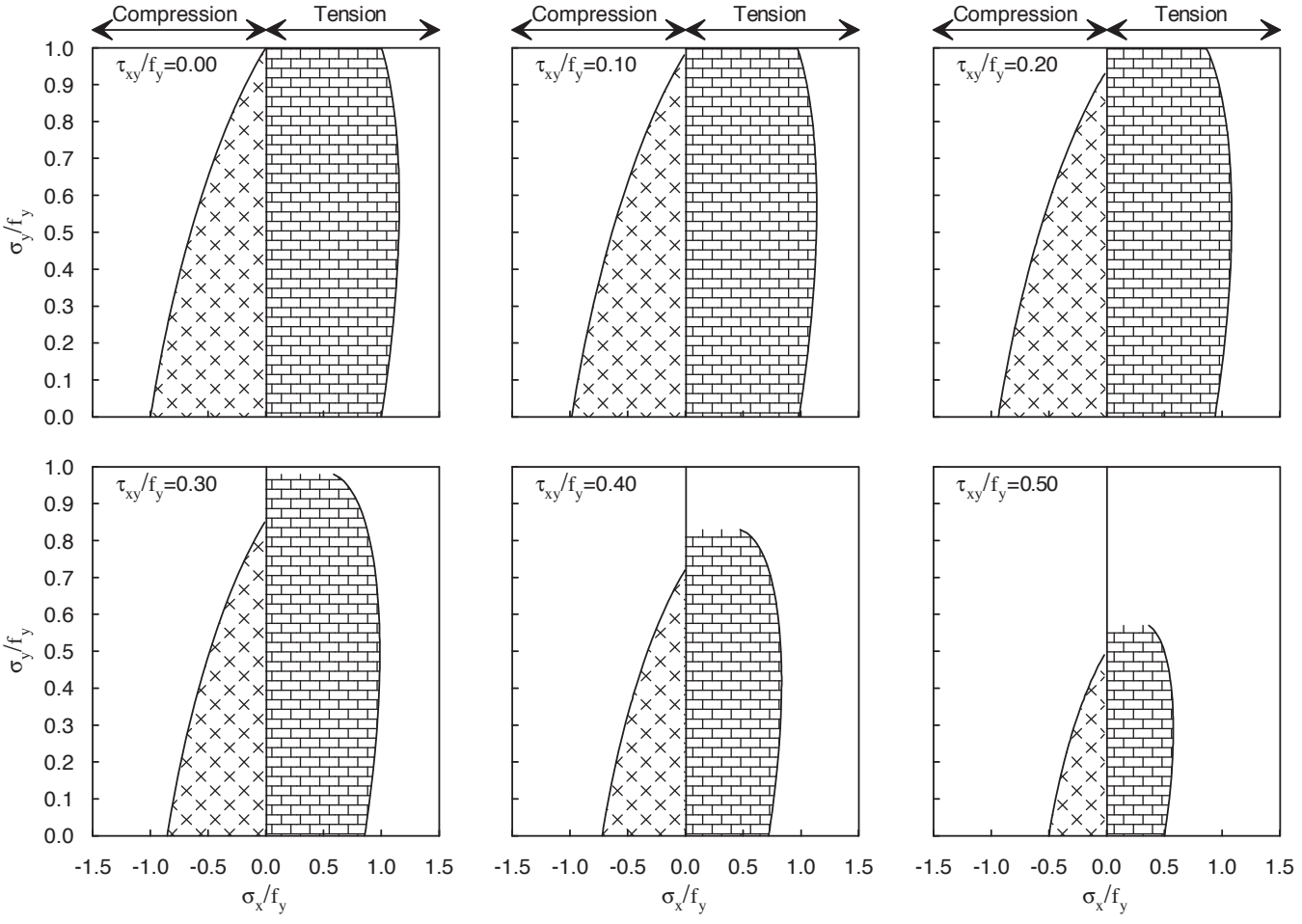

Fig. 5. Reduced yield strength per the von Mises yield criterion in plane stress.

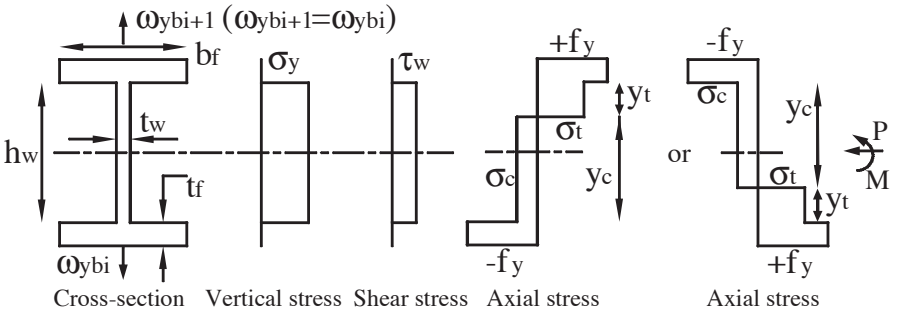

Fig. 6. Stress diagrams of intermediate HBE cross section under flexure, axial compression, shear force and vertical stresses due to equal top and bottom tension fields.

From the geometry in Figure 6,

$$y_t = h_w - y_c \tag{13}$$

where y_c and y_t represent compression and tension portion of the web, respectively.

For the common case that the neutral axis remains in the web, the governing equation of axial force equilibrium can be given as:

$$\sigma_c y_c t_w + \sigma_t y_t t_w = P \tag{14}$$

Note that the contribution of the flanges to axial compression is nil because the resultant axial force of each flange has the same magnitude but opposite sign (and thus each cancels the other).

Substituting Equation 13 into Equation 14 and solving for y_c gives

$$y_c = \frac{\left(\frac{\sigma_t}{f_y}\right) + \beta_w}{\left(\frac{\sigma_t}{f_y}\right) - \left(\frac{\sigma_c}{f_y}\right)} \times h_w \tag{15}$$

where β_w is the ratio of the applied axial compression to the nominal axial strength of the web, which is given by:

$$\beta_w = \frac{-P}{f_y h_w t_w} \tag{16}$$

The contributions of the web and flanges to the plastic moment of the whole cross section, M_{pr-web} and $M_{pr-flange}$, can be respectively determined as:

$$M_{pr-web} = \sigma_t t_w y_t \left(\frac{h_w}{2} - \frac{y_t}{2}\right) - \sigma_c t_w y_c \left(\frac{h_w}{2} - \frac{y_c}{2}\right) \tag{17}$$

$$M_{pr-flange} = f_y b_f t_f \left(d - t_f\right) \tag{18}$$

A cross-section plastic moment reduction factor, β, is defined to quantify the loss in plastic strength attributable to the combined effect of the axial compression, shear force and vertical stresses acting on the HBE web. The magnitude of β can be determined as:

$$\beta = \frac{M_{pr-web} + M_{pr-flange}}{f_y Z} \tag{19}$$

where Z is the plastic section modulus of HBE.

As shown in Equations 11 and 12, the acting direction of shear stresses (i.e., the sign of τ_w) has no impact on the resulting compression and tension axial yield strengths and, consequently, makes no difference in the calculated plastic moment reduction factor.

For the extreme case for which the HBE web makes no contribution to the flexural resistance, the minimum value of the reduction factor, β_{min}, is obtained and is given as:

$$\beta_{min} = \frac{M_{pr-flange}}{f_y Z} \tag{20}$$

This will happen when the entire web is under uniform compression.

Finite Element Verification

To validate the approach developed earlier to calculate the plastic moment reduction factor of intermediate HBEs under equal top and bottom tension fields, a series of finite element analyses was performed on a segment of HBE. The finite element model is shown in Figure 7.

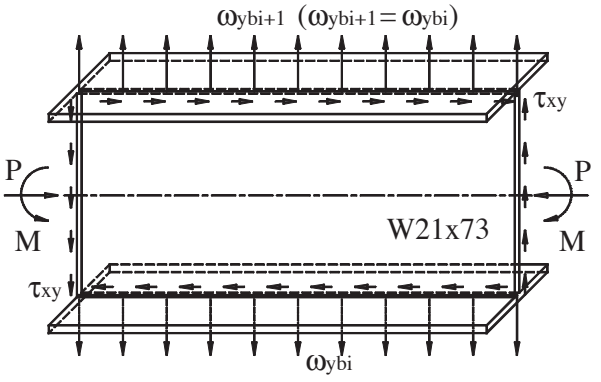

(*a*)

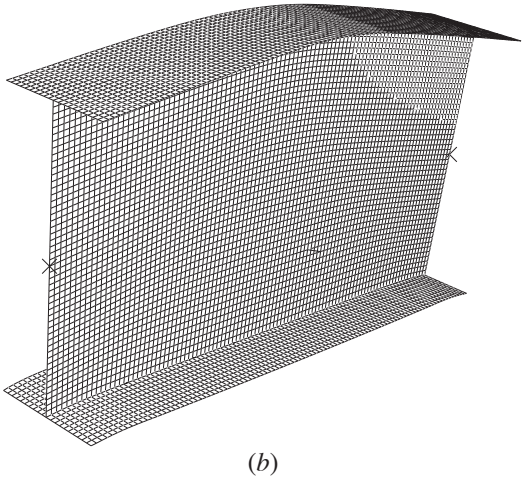

(*b*)

Fig. 7. Finite element model of intermediate HBE segment under flexure, axial compression, shear force and vertical stresses due to equal top and bottom tension fields.

In this case, a W21×73 member was modeled in ABAQUS/Standard (ABAQUS 2005). The length of this member was twice the cross-section depth. Material was assumed to be A572 Grade 50 steel with isotropic, elastic-perfectly-plastic constitutive behavior. A shell element (ABAQUS element S4R) was employed for the web and flanges. A fine mesh with 9,000 elements (2,000 elements per flange and 5,000 elements for the web) was used in this model.

As shown in Figure 7, uniform loads, ω_{ybi+1} and ω_{ybi}, of identical magnitude, but in opposite directions at the top and bottom edges of the HBE web, represented the vertical components of the top and bottom tension fields. Uniform shear stresses, τ_{xy}, were applied along the edges of the HBE web. Axial forces applied at the ends of the member represented the axial compression in the HBE.

The finite element analysis was conducted in two stages to correctly replicate the boundary conditions and to achieve the desired load scenario while keeping the whole model in self-equilibrium. In the first stage, the aforementioned tension fields, shear stresses and axial forces were applied on the model. In the second stage, a displacement-controlled analysis procedure was used in which the rotations of

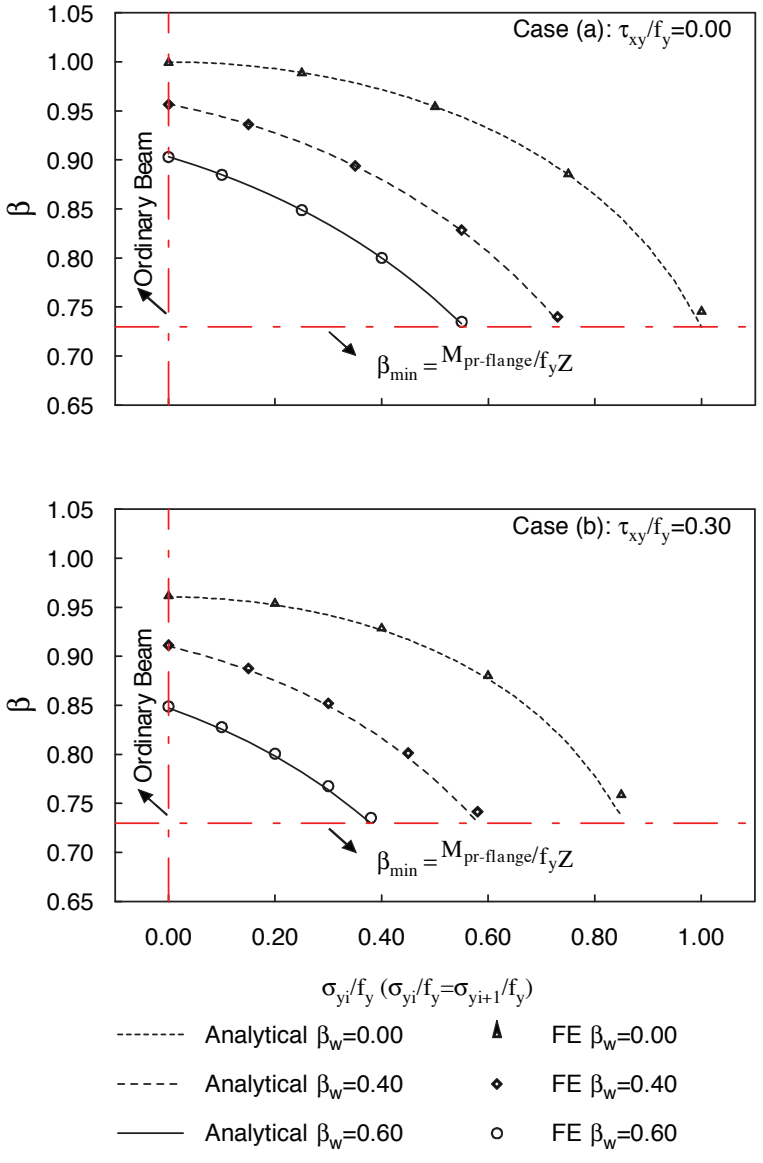

Fig. 8. Plastic moment reduction factor of intermediate HBE under axial compression, shear force and constant vertical stresses: analytical prediction versus finite element results.

opposite directions were proportionally increased up to a magnitude of 0.035 rad at the ends of the HBE segment to obtain the plastic moment strength A series of analyses was conducted on the finite element model to assess the accuracy of the analytical procedure. A comparison of results is given in Figure 8, which shows that the finite element analysis agrees with the analytical procedure. For the given axial compression and shear stresses, the magnitudes of the identical tension fields were increased from nil to the maximum value allowable in the HBE web to capture the entire range of solutions. For each case of β_w, five different vertical stress conditions (approximately equally spaced in the range of σ_y/f_y) were considered in the finite element models. Note that the axial compression, shear stresses and vertical stresses developed in the HBEs depend on the infill panel tension field actions and size and material property of the HBEs. As a result, the combined axial compression, shear stresses and vertical stresses selected for these analyses may not necessarily develop in a specific intermediate HBE. Also note that the plastic moment reduction factor of intermediate HBE shown in Figure 8 reduces to that which corresponds to the values of an ordinary beam in the absence of tension fields. As shown, the cross-section plastic moment reduction factor varies from unity to the minimum when increasing the shear stresses, axial forces and vertical stresses.

INTERMEDIATE HBE UNDER UNEQUAL TOP AND BOTTOM TENSION FIELDS

In many cases, the infill panels above and below intermediate HBE are of different thicknesses, which may result in unequal top and bottom tension fields when the expected plastic mechanism of the wall develops. This section investigates how the HBE plastic moment would be affected by the unequal top and bottom tension fields. As listed in Table 1, both the positive and negative flexures will be considered. The fundamental concepts and modeling assumptions previously presented still apply, except that a linear variation of vertical stresses is assumed instead of the prior constant vertical stresses.

Derivation of Plastic Moment under Positive Flexure

As shown in Figure 9, one can generate the stress diagrams for a fully plastified HBE cross section of elasto-perfectly plastic steel subjected to axial compression, shear, vertical stresses due to unequal top and bottom tension fields and positive flexure. As an approximation, linearly varying vertical stresses are assumed to act on the HBE web. Mathematically, this assumption is expressed as:

$$\frac{\sigma_y(y)}{f_y} = \left(\frac{\sigma_{yi}}{f_y}\right)\left(1 - \frac{y}{h_w}\right) + \left(\frac{\sigma_{yi+1}}{f_y}\right)\left(\frac{y}{h_w}\right) \tag{21}$$

where the vertical stresses at the top and bottom edges of the HBE web, σ_{yi+1} and σ_{yi}, can be calculated respectively as:

$$\sigma_{yi+1} = \frac{\omega_{ybi+1}}{t_w} \tag{22}$$

$$\sigma_{yi} = \frac{\omega_{ybi}}{t_w} \tag{23}$$

In accordance with Equation 8, the tension and compression axial yield strengths in the web can be respectively determined as:

$$\frac{\sigma_t(y)}{f_y} = \frac{1}{2}\frac{\sigma_y(y)}{f_y} + \frac{1}{2}\sqrt{4 - 3\left[\frac{\sigma_y(y)}{f_y}\right]^2 - 12\left(\frac{\tau_w}{f_y}\right)^2} \tag{24}$$

$$\frac{\sigma_c(y)}{f_y} = \frac{1}{2}\frac{\sigma_y(y)}{f_y} - \frac{1}{2}\sqrt{4 - 3\left[\frac{\sigma_y(y)}{f_y}\right]^2 - 12\left(\frac{\tau_w}{f_y}\right)^2} \tag{25}$$

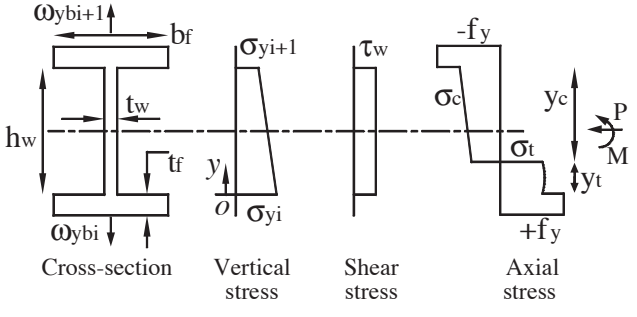

Fig. 9. Stress diagrams of intermediate HBE cross section under positive flexure, axial compression, shear force and vertical stresses due to unequal top and bottom tension fields.

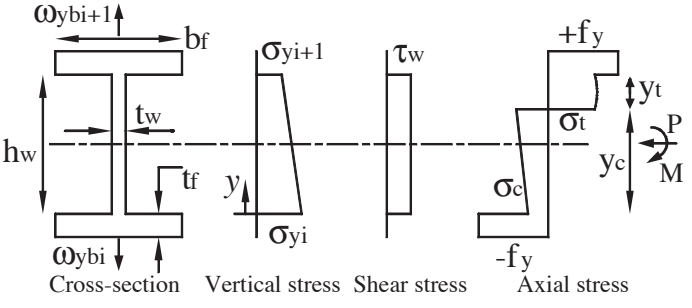

Fig. 10. Stress diagrams of intermediate HBE cross section under negative flexure, axial compression, shear force and vertical stresses due to unequal top and bottom tension fields.

Corresponding to Equation 14, the governing equation of axial force equilibrium can be given as:

$$\int_0^{h_w-y_c} \sigma_t(y)\,t_w\,dy + \int_{h_w-y_c}^{h_w} \sigma_c(y)\,t_w\,dy = P \tag{26}$$

Substituting Equations 24 and 25 into Equation 26, and also using the assumption expressed in Equation 21, gives the following equation:

$$\int_0^{h_w-y_c} \left\{ \begin{array}{l} \frac{1}{2}\left[\left(\frac{\sigma_{yi}}{f_y}\right)\left(1-\frac{y}{h_w}\right)+\left(\frac{\sigma_{yi+1}}{f_y}\right)\left(\frac{y}{h_w}\right)\right] \\ +\frac{1}{2}\sqrt{4-3\left[\left(\frac{\sigma_{yi}}{f_y}\right)\left(1-\frac{y}{h_w}\right)+\left(\frac{\sigma_{yi+1}}{f_y}\right)\left(\frac{y}{h_w}\right)\right]^2-12\left(\frac{\tau_{xy}}{f_y}\right)^2} \end{array} \right\} t_w\,dy$$
$$+\int_{h_w-y_c}^{h_w} \left\{ \begin{array}{l} \frac{1}{2}\left[\left(\frac{\sigma_{yi}}{f_y}\right)\left(1-\frac{y}{h_w}\right)+\left(\frac{\sigma_{yi+1}}{f_y}\right)\left(\frac{y}{h_w}\right)\right] \\ -\frac{1}{2}\sqrt{4-3\left[\left(\frac{\sigma_{yi}}{f_y}\right)\left(1-\frac{y}{h_w}\right)+\left(\frac{\sigma_{yi+1}}{f_y}\right)\left(\frac{y}{h_w}\right)\right]^2-12\left(\frac{\tau_{xy}}{f_y}\right)^2} \end{array} \right\} t_w\,dy = P \tag{27}$$

It is not possible to solve for the closed-form solution of y_c from Equation 27, but one may use software packages such as Mathcad to obtain the numerical solution of y_c. Then, knowing y_c, the contribution of the web to the plastic moment of the whole cross section can be determined as:

$$M_{pr-web} = \int_0^{h_w-y_c} \sigma_t(y)\left(\frac{h_w}{2}-y\right)t_w dy + \int_{h_w-y_c}^{h_w} \sigma_c(y)\left(\frac{h_w}{2}-y\right)t_w dy \tag{28}$$

For the contribution of the flanges, $M_{pr-flange}$, and the plastic moment reduction factor, β, Equations. 18 and 19 still apply.

Derivation of Plastic Moment under Negative Flexure

Results can also be generated following the same procedure for the case of negative flexure. The resulting stress diagrams are shown in Figure 10. All the equations developed to locate the neutral axis for the case of positive flexure remain valid, except that the integral limits of Equation 26 need to be modified as follows according to the stress diagrams shown in Figure 10:

$$\int_{y_c}^{h_w} \sigma_t(y)\,t_w\,dy + \int_0^{y_c} \sigma_c(y)\,t_w\,dy = P \tag{29}$$

Solving for y_c from Equation 29, one can obtain the contribution of the web to the plastic moment of the whole cross section as:

$$M_{pr-web} = \int_{y_c}^{h_w} \sigma_t(y)\left(y-\frac{h_w}{2}\right)t_w dy + \int_0^{y_c} \sigma_c(y)\left(y-\frac{h_w}{2}\right)t_w dy \tag{30}$$

For the contribution of the flanges to the moment resistance, $M_{pr-flange}$, and cross-section plastic moment reduction factor, β, Equations 18 and 19 remain valid.

Finite Element Verification

To validate the approach developed earlier for determining the plastic moment of intermediate HBEs under unequal top and bottom tension fields, a series of finite element analyses were performed. The finite element models for positive and negative flexure cases are shown in Figure 11.

The material, element, mesh, boundary condition and loading sequence are the same as those for intermediate HBEs under equal top and bottom tension fields, except that a surface traction was applied on the HBE web to achieve the transition between the unbalanced tension fields and satisfy vertical force equilibrium. The surface traction, *S*, can

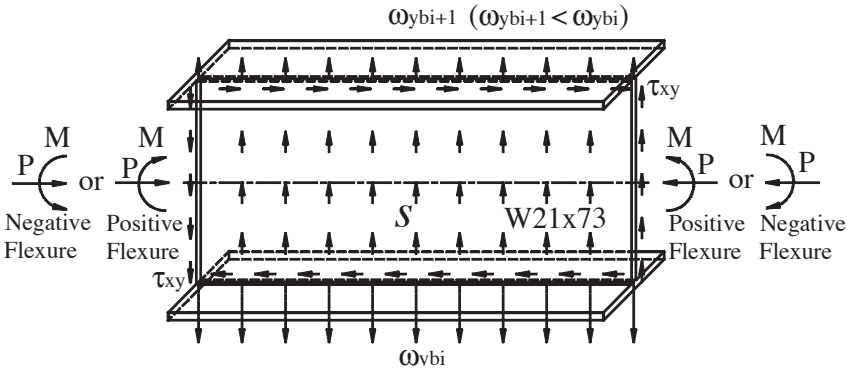

Fig. 11. Finite element model of intermediate HBE under flexure, axial compression, shear force and vertical stresses due to unequal top and bottom tension fields.

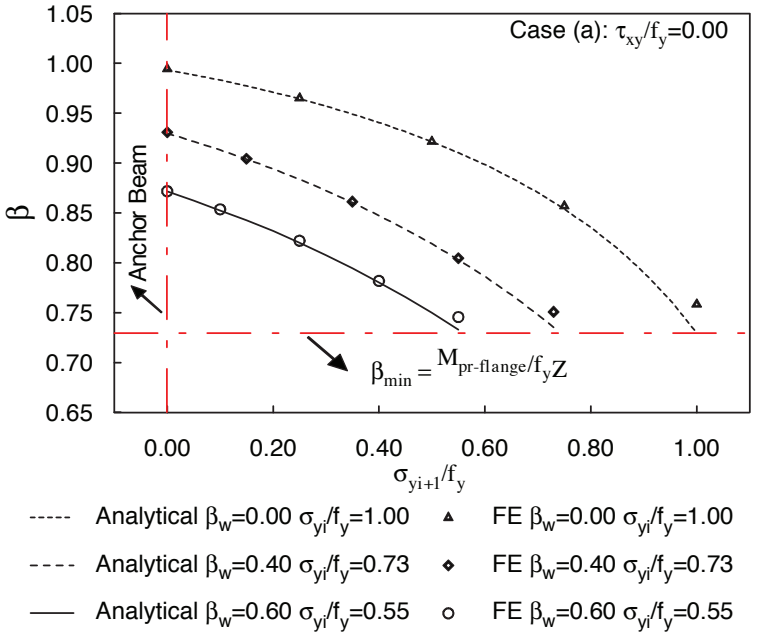

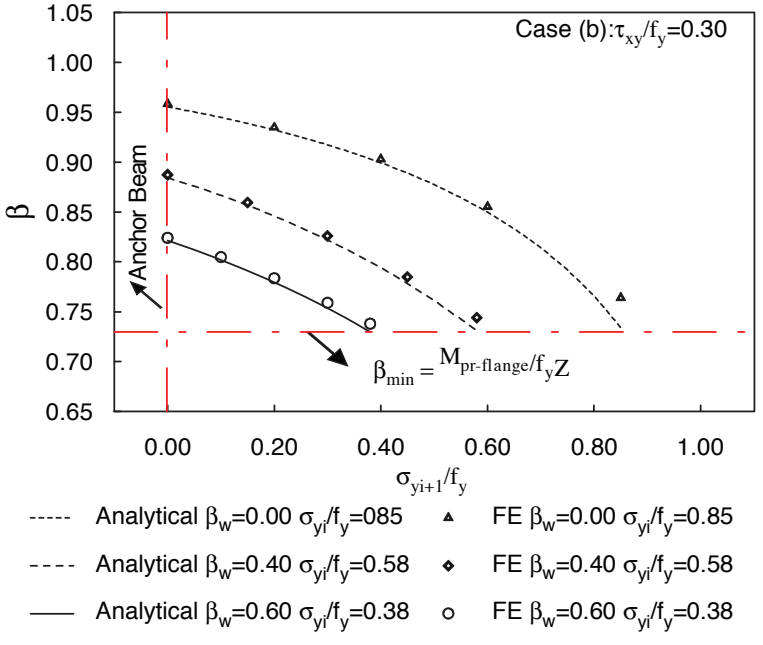

Fig. 12. Plastic moment reduction factor of intermediate HBE under positive flexure, axial compression, shear force and linear vertical stresses: analytical prediction versus finite element results.

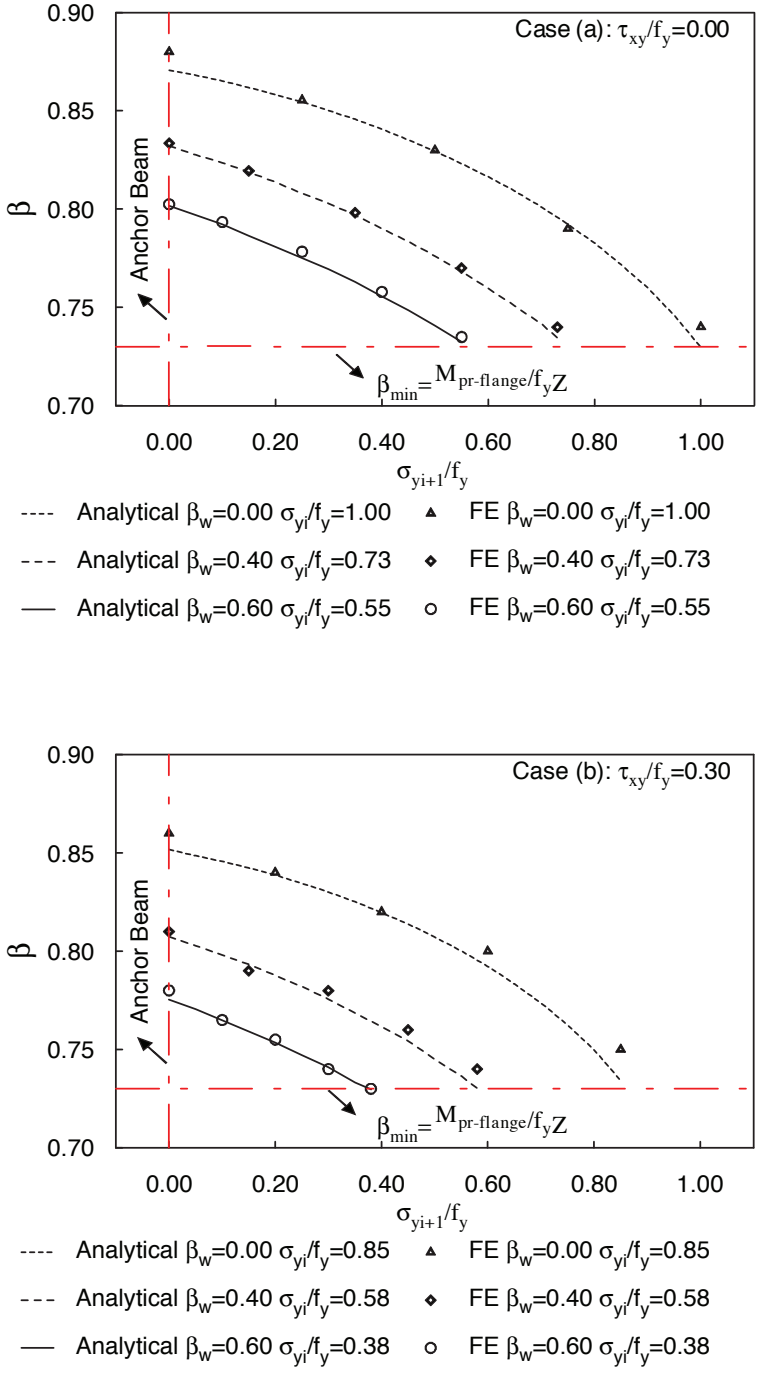

Fig. 13. Plastic moment reduction factor of intermediate HBE under negative flexure, axial compression, shear force and linear vertical stresses: analytical prediction versus finite element results.

be calculated as:

$$S = \frac{\omega_{ybi} - \omega_{ybi+1}}{h_w} \tag{31}$$

Note that, in reality, no such traction force is applied on the HBE web, because the unbalanced infill panel yield forces are equilibrated similarly to a uniformly distributed load on a beam. However, in modeling only a small beam segment as done earlier, the application of *S* keeps the segment in self-equilibrium and guarantees linear distribution of vertical stresses in the HBE web, consistent with the assumption used for derivation of the analytical procedures.

A series of analyses was conducted using the finite element models described earlier to assess the accuracy of the analytical procedures. In these analyses, for the given axial compression and shear force, the vertical component of the bottom tension field was kept constant and various magnitudes of the vertical component of the top tension field were considered—from zero up to a value equal to that of the bottom tension field. This range of infill panel yield forces acting on the top tension field starts from an intermediate HBE cross-section equivalent to an anchor HBE cross section in the absence of the top tension field and ends with the previously considered case of an intermediate HBE cross section under equal top and bottom tension fields.

Comparisons of the results from finite element analysis with those obtained following the analytical procedures are shown in Figures 12 and 13 for the positive and negative flexure cases, respectively. It is shown that the plastic moment of intermediate HBE under unequal top and bottom tension fields can be accurately estimated using the analytical procedures. The plastic moment reduction factor varies from unity to the minimum determined by Equation 20 as a result of the increasing shear force, axial force and vertical stresses.

Comparing the results shown in Figure 12 with those shown in Figure 13, it is also possible to observe that for the same combination of axial compression, shear forces and vertical stresses, the plastic moment under positive flexure is greater than that under negative flexure. For example, according to case a shown in Figure 12, the plastic moment reduction factor is 0.97 for an intermediate HBE under positive flexure for which $\tau_{xy}/f_y = 0.00$, $\beta_w = 0.00$, $\sigma_{yi}/f_y = 1.00$, and $\sigma_{yi+1}/f_y = 0.20$; however, a smaller value of 0.86 is obtained for the corresponding negative flexure case as shown in case a of Figure 13. This can be explained on the basis that higher vertical stresses are acting at the bottom of the beam segment, which is also in axial compression in the negative flexure case. Recall from Figure 5 (which shows yielding under biaxial loading conditions, per the von Mises yield criterion) that the compression axial yield strength is more reduced by the presence of vertical stresses than the tension axial yield strength. Therefore, the plastic moment is reduced more in the negative flexure case than the positive flexure case.

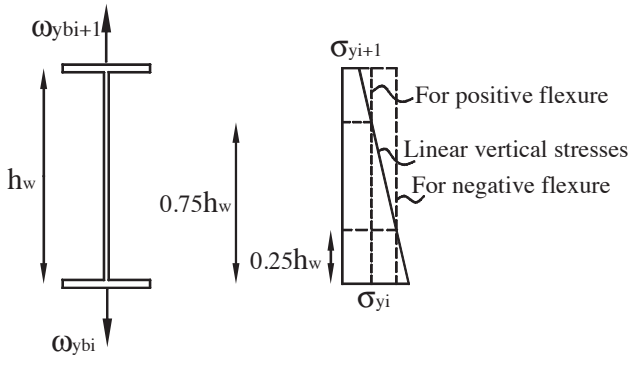

Fig. 14. Simplification of vertical stress distribution.

Simplification of Analytical Procedures

Although the analytical procedures to estimate the plastic moment of intermediate HBE under unequal top and bottom tension fields were developed and verified by finite element results, impediments exist that may limit the acceptance of this approach in design practice. For example, there are challenges in solving for y_c from Equations 27 and 29 using simple calculations. The mathematical difficulty results from the presence of nonconstant vertical stresses.

Aiming at the kind of simple equations derived to calculate the plastic moment of intermediate HBE under equal top and bottom tension fields, for which constant vertical stress is assumed, it would be expedient to replace the linearly varying vertical stresses in the case at hand by an equivalent constant vertical stress. However, it would not be appropriate to use a constant vertical stress of magnitude equal to the average stress of the linearly varying vertical stresses as an approximation, because such a unique equivalent constant vertical stress would result in identical plastic moments for both positive and negative flexure cases. This is inconsistent with the prior observations from Figures 12 and 13.

As a compromise between simplicity and accuracy, to consider the different effects of vertical stresses on plastic moment of intermediate HBEs under positive and negative flexures, the magnitudes of those stresses at the three-fourths and one-fourth points of the linearly varying stress diagram, as shown in Figure 14, are taken as the magnitudes of the equivalent constant vertical stresses for the positive and negative flexure cases, respectively. Mathematically, the magnitudes of these equivalent constant vertical stress distributions can be expressed as:

$$\sigma_{y-uni} = \frac{1}{2}\left(\sigma_{yi} + \sigma_{yi+1}\right) \pm \frac{1}{4}\left(\sigma_{yi} - \sigma_{yi+1}\right) \tag{32}$$

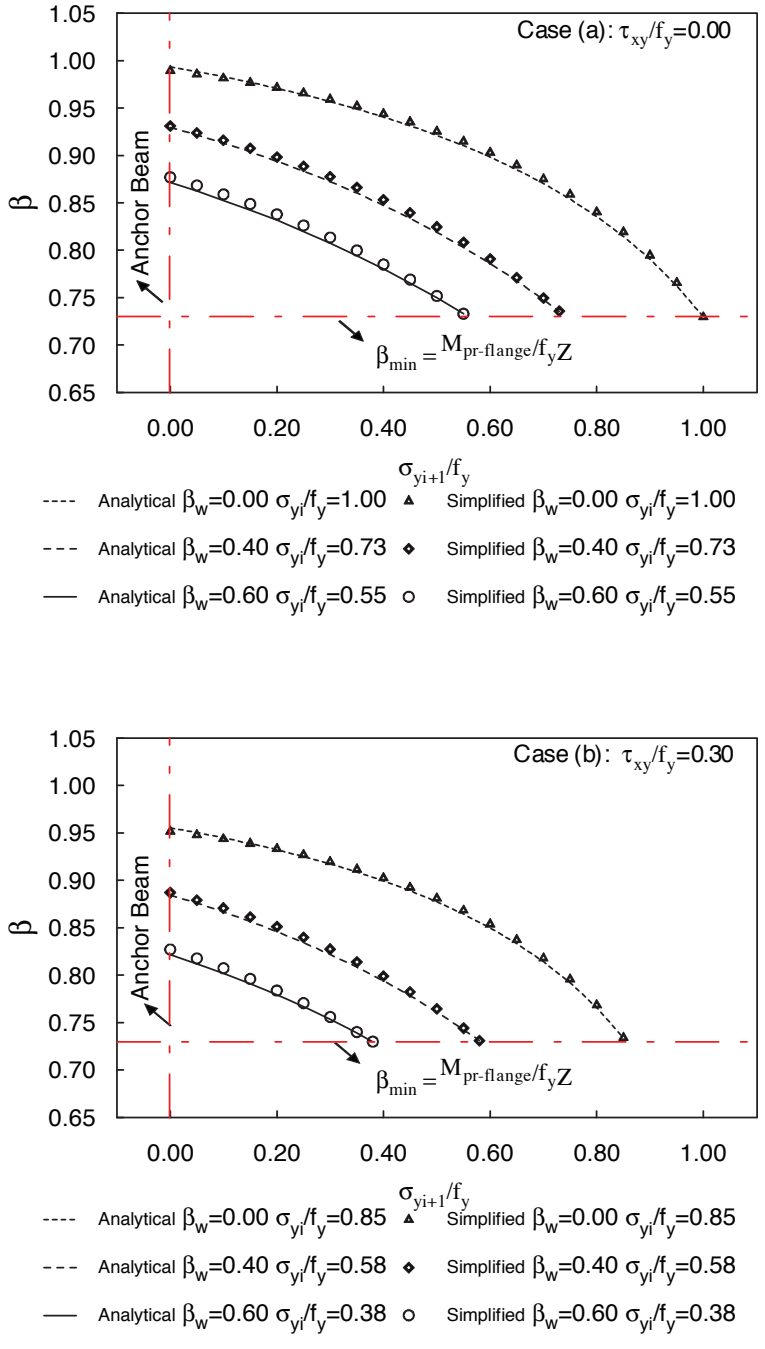

Fig. 15. Plastic moment reduction factor of intermediate HBE under positive flexure, axial compression, shear force and linear vertical stresses: analytical prediction versus simplified approach.

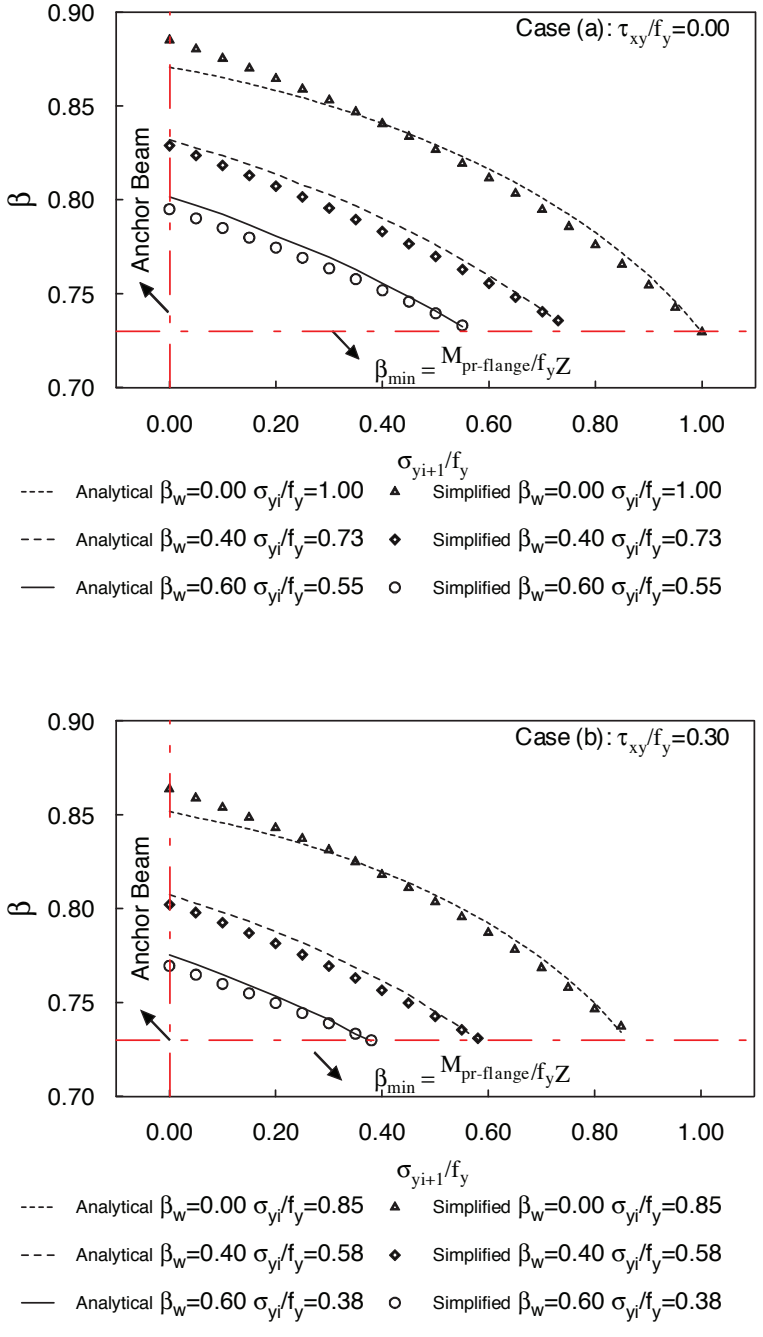

Fig. 16. Plastic moment reduction factor of intermediate HBE under negative flexure, axial compression, shear force and linear vertical stresses: analytical prediction versus simplified approach.

Minus (–) and plus (+) signs are employed in Equation 32 for the positive and negative flexure cases, respectively. Then, the procedures to determine the plastic moment of intermediate HBE under equal top and bottom tension fields can be used.

To check the adequacy of this model, the results obtained using the preceding simplified procedure are compared with those using the more rigorous analytical procedures developed earlier in Figures 15 and 16 for positive and negative flexure cases, respectively. It is found that the simplified procedure provides reasonable and relatively efficient estimates of the cross-section plastic moment reduction factors, although slightly less accurate results are observed in the negative flexure case.

ADDITIONAL DISSCUSSION ON ANCHOR HBE

Results developed for intermediate HBEs under unequal top and bottom tension fields can also be applied for anchor HBE because anchor HBE is only a special case of intermediate HBE for which the tension field is only applied on one side. This can be achieved by setting σ_{yi+1} equal to zero in all equations derived in previous section. Although examples shown in Figures 12, 13, 15 and 16 only provide results for anchor HBEs in limited scenarios (i.e., only loading scenarios corresponding to the left ends of those curves), additional examples developed by Qu and Bruneau (2008) further confirmed that the analytical procedures and simplified models for estimating the plastic moment of intermediate HBEs under unequal top and bottom tension fields remain valid for anchor HBEs.

CONCLUSIONS

Analytical procedures for estimating the plastic moments of intermediate HBEs of SPSWs have been developed in this paper. Those procedures are based on classic plastic analysis and rely on calculation of the reduced axial yield strength of HBE web accounting for the presence of shear and vertical stresses. Results from these procedures were shown to agree well with the results from finite element analysis. Simplified models developed for practical purposes were shown to be accurate. These formulations presented here were critical to explain the behavior observed experimentally in prior tests; see Qu and Bruneau (2010) for comparisons of test results with results from finite element analyses (similar to those for which the closed-form equations presented here have been shown to give satisfactory results). Implementation of the developed analytical procedure is necessary to achieve capacity design of HBE-to-VBE connections, which ensures desirable performance of HBEs.

ACKNOWLEDGMENTS

This work was supported by the Earthquake Engineering Research Centers Program of the National Science Foundation under award number ECC-9701471 to the Multidisciplinary Center for Earthquake Engineering Research. Any opinions, findings, conclusions and recommendations presented in this paper are those of the writers and do not necessarily reflect the views of the sponsors.

SYMBOLS

M = moment acting at HBE cross section

P = axial compression acting at HBE cross section

Z = plastic section modulus

b_f = flange width of the cross section

d = depth of the cross section

f_y = yield strength of steel

h_w = web depth of the cross section

t_f = flange thickness of the cross section

t_w = web thickness of the cross section

y_c = compression portion in the web of the cross section

y_t = tension portion in the web of the cross section

y_o = location of the neutral axis

σ_w = maximum axial stress that can be applied on the web of the cross section

σ_{yi} = vertical stress in HBE web

τ_w = shear stress acting on the web of the cross section

ω_{ybi} = vertical components of the infill panel forces

REFERENCES

ABAQUS (2005), *ABAQUS Analysis User's Manual* (version 6.5), Hibbitt, Karlsson, and Sorenson, Pawtucket, RI.

AISC (2010), ANSI/AISC 341-10, *Seismic Provisions for Structural Steel Buildings*, American Institute of Steel Construction, Chicago, IL.

Berman, J.W. and Bruneau, M. (2003a), "Experimental Investigation of Light-Gauge Steel Plate Shear Walls for the Seismic Retrofit of Buildings," *Technical Report MCEER-03-0001*, Multidisciplinary Center for Earthquake Engineering Research, Buffalo, NY.

Berman, J.W., and Bruneau, M. (2003b), "Plastic Analysis and Design of Steel Plate Shear Walls," *Journal of Structural Engineering*, Vol. 129, No. 11.

Bruneau, M., Uang, C.M. and Whittaker, A.S., (1998), *Ductile Design of Steel Structures,* McGraw-Hill Companies, Inc., New York, NY.

CSA (2009), CAN/CSA S16-01*, Limit States Design of Steel Structures,* Willowdale, ON, Canada.

Driver, R.G., Kulak, G.L., Kennedy, D.J.L. and Elwi, A.E. (1997), "Seismic Behavior of Steel Plate Shear Walls," *Structural Engineering Report No.215*, University of Alberta, Edmonton, AB, Canada.

Elgaaly, M., Caccese, V. and Du, C. (1993), "Postbuckling Behavior of Steel-Plate Shear Walls under Cyclic Loads," *Journal of Structural Engineering*, Vol. 119, No. 2.

Qu, B. and Bruneau, M. (2008), "Seismic Design of Boundary Frame Members of Steel Plate Shear Walls," *Technical Report MCEER-08-0012*, Multidisciplinary Center for Earthquake Engineering Research, Buffalo, NY.

Qu, B., Bruneau, M., Lin, C.H. and Tsai, K.C. (2008), "Testing of Full Scale Two-Story Steel Plate Shear Walls with RBS Connections and Composite Floor," *Journal of Structural Engineering*, Vol. 134, No. 3.

Qu, B. and Bruneau, M. (2010), "Capacity Design of Intermediate Horizontal Boundary Elements of Steel Plate Shear Walls," *Journal of Structural Engineering*, Vol. 135, No. 12.

Sabelli, R. and Bruneau, M. (2006), *Design Guide 20: Steel Plate Shear Walls,* American Institute of Steel Construction, Chicago, IL.

Thorburn, L.J., Kulak, G.L. and Montgomery, C.J. (1983), "Analysis of Steel Plate Shear Walls," *Structural Engineering Report No. 107*, Department of Civil Engineering, The University of Alberta, Edmonton, AB, Canada.

Tsai, K.C. and Lee, C.S. (2007), "Slender SPSW," *Technical Report NCREE-06-017*, National Center for Research on Earthquake Engineering. Taipei, Taiwan (in Chinese).

Vian, D. and Bruneau, M. (2005), "Steel Plate Shear Walls for Seismic Design and Retrofit of Building Structure," *Technical Report MCEER-05-0010*, Multidisciplinary Center for Earthquake Engineering Research, Buffalo, NY.

DISCUSSION

Design and Behavior of Multi-Orientation Fillet Weld Connections

Paper by LOGAN J. CALLELE, ROBERT G. DRIVER and GILBERT Y. GRONDIN
(Fourth Quarter 2009)

Discussion by ROBERT A. JAMES

The authors present a good discussion on the subject about how the angle of loading affects weld strength. However, there are two comments at the end of the article regarding the fusion area between the fillet weld and base metal that concern me.

The first statement is "Current design procedures limit the use of equations to predict fillet weld strength for any fillet weld orientation by requiring that the strength of the base metal at the fusion face also be checked." To the best of my knowledge, this check has never been a requirement in the AISC *Specification*. I believe this misconception started in the 1978 edition of the *Specification,* as published in the eighth edition of the steel manual. Table 1.5.3 stated "the allowable shear stress on the effective area of a fillet weld is 0.30 times the nominal tensile strength of weld metal, except shear stress on base metal shall not exceed 0.40 times the yield stress of base metal." Many people misinterpreted this mention of base metal to be a requirement that the shear stress along the leg of the weld be checked using the strength of the base metal. However, the base metal check was intended to be a reinforcement of the requirement of Section 1.5.1.2 to limit the shear stress in the *connected parts*, not the weld.

In the 1989 edition of the AISC ASD *Specification,* as published in the ninth edition of the steel manual, the wording to check base metal stress was not included in Table J2.5. Also, Figure C-J2.1 and the corresponding discussion provided a clear explanation to show where weld and base metal checks are to be performed. The weld check is at the throat of the weld.

I am concerned that the 2005 edition of the AISC *Specification,* as published in the thirteenth edition of the steel manual, may have re-introduced the confusion. Section J2.4 states "the strength of welds shall be the lower value of the base material and the weld metal strength." (I believe it would have been more accurate to say "the strength of *connections*" instead of "the strength of *welds.*") Fortunately, Figure C-J2.10 is provided, which also shows the appropriate locations for stress to be checked within the connection.

The second statement in the article is "Many test specimens exhibited a fracture surface that followed the fusion area between the fillet weld and the base metal." It has always been my understanding that unless the weld electrode is more than two strength categories greater than the matching one for the base metal, the welded joint will fail in the weld material. The heat-affected zone between the weld and base metal, due to mixing of the molten material during the welding process, attains superior strength properties to those of the base metal. Consequently, the shear stress along the weld metal-to-base metal interface need not be checked. Also, Table 5.2 in the referenced article by Deng, Grondin and Driver provides the fracture angle determined by other researchers. This shows that the weld failure occurs in the weld and not along the fusion area between the fillet weld leg and base metal.

Although the authors do reach a conclusion that it is not necessary to check the base metal strength on the fusion area, the discussion of the fusion area between the weld and base metal as a possible failure plane is contrary to my understanding of how welds perform. To think that a weld could fail on a fracture plane other than the theoretical throat does not have an impact on my confidence level in traditional weld design the way that the thought the failure plane could be along the leg of the weld does.

Robert A. James, P.E., Senior Civil Engineer, Bechtel Corporation, Spring City, TN. E-mail: rajames@bechtel.com

CLOSURE

Design and Behavior of Multi-Orientation Fillet Weld Connections

Paper by LOGAN J. CALLELE, ROBERT G. DRIVER and GILBERT Y. GRONDIN
Closure by LOGAN J. CALLELE, ROBERT G. DRIVER and GILBERT Y. GRONDIN

The authors thank Mr. James for his comments on our paper and agree that a check of the weld throat and of the shear plane in the connecting material is sufficient; the fusion zone does not need to be checked. The first comment, regarding whether or not there is a need to check the base metal capacity in fillet weld design, is largely a historical review of how this is dealt with in the AISC *Specification*. However, he seems to be in agreement with the paper that Equations J2-4 and J2-5 of the 2005 edition of the AISC *Specification* are sufficient to adequately design fillet welded connections made with matching electrodes and that Equation J2-2 is not a necessary part of the weld capacity check—although this is contrary to the apparent requirements of the AISC *Specification*, as well as the provisions of Canadian design standard S16-01.

The second point made in the discussion is about the fracture surface angle of a fillet weld loaded to rupture. It must be recognized that inconsistencies with pure theory are to be expected due to the nonhomogeneous nature and geometric irregularities of the weld material. In experimental research programs on the strength and behavior of fillet welds, a variety of fracture surface angles have been observed that include angles of 0 and 90 degrees. Moreover, the angle can change dramatically along the length of a fillet weld, even if the theoretical stress conditions are uniform. As such, the predicted fracture surface angle can only be quantified for a given angle of loading from a statistical perspective. Although it has been observed on some tested fillet weld connections with matching electrodes that the fracture surface does indeed follow the fusion surface (though this is statistically unlikely), Equations J2-4 and J2-5 of the AISC *Specification* still adequately predict the strength of these connections.

Logan Callele, P.Eng., Structural Engineer, Waiward Steel Fabricators Ltd., Edmonton, AB, Canada (corresponding author). E-mail: logan.callele@waiward.com

Robert G. Driver, Professor, Department of Civil and Environmental Engineering, University of Alberta, Edmonton, AB, Canada. E-mail: rdriver@ualberta.ca

Gilbert Y. Grondin, Professor, Department of Civil and Environmental Engineering, University of Alberta, Edmonton, AB, Canada. E-mail: ggrondin@ualberta.ca

Current Steel Structures Research

No. 25

REIDAR BJORHOVDE

This issue of the *Engineering Journal* focuses on a selection of current research projects at a number of Canadian universities. The descriptions will not discuss all of the current projects at the schools. Instead, selected studies give a representative picture of the research efforts and demonstrate the importance of the schools to the efforts of industry and the profession. The close relations between AISC and CISC, the Canadian Institute of Steel Construction, have provided significant benefits to researchers, designers and industry on both sides of the border. The standards for materials, design and fabrication of both countries reflect mutual accomplishments that have offered benefits to all.

The universities and many of their structural steel researchers are very well known in the world of steel construction: University of Toronto, University of Waterloo, University of Ottawa, Dalhousie University in Halifax and Carleton University in Ottawa. Some of the many projects at the University of Alberta were discussed in the "Current Steel Structures Research" paper that was published in the second quarter 2010 issue of the *Engineering Journal* (Bjorhovde, 2010). Some of the ongoing work at the University of British Columbia will be featured in a future paper. For example, a project directed by Professor Siegfried Stiemer is providing novel approaches to the performance considerations for hybrid structures. The work at École Polytechnique in Montreal, whose leading steel researcher is Professor Robert Tremblay, will also be discussed in a future paper. Professor Tremblay has played a significant role in the understanding and development of seismic design criteria for braced frames in Canada as well as the United States.

All of the projects presented in this paper are funded in full or in part by the Steel Structures Education Foundation (SSEF) of Canada.

In true forward-looking fashion, the researchers at the institutions that are featured here have been active for many years, as evidenced by their participation and leading roles in the design standards development efforts of Canada and the United States and many other countries. Large numbers of technical papers, reports and conference presentations have been published, contributing to a collection of studies that continue to offer practical solutions to complex problems for designers as well as fabricators and erectors.

References are provided throughout the paper, whenever such are available in the public domain. However, much of the work is still in progress, and in some cases reports or publications have not yet been prepared for public dissemination.

SOME CURRENT RESEARCH WORK AT THE UNIVERSITY OF TORONTO

Over the years, the University of Toronto has been a leader in many areas of structural engineering research. For steel construction, the principal contributors have been Professors Peter Birkemoe and Jeffrey Packer, with studies that have included innovative solutions to the strength, behavior and design of connections of various kinds, column strength and stability, and the behavior of structures subjected to high-energy loading conditions.

The famous study of Birkemoe and Gilmor on block shear (1978) defined a new and very important limit state; the subject has since been examined by a large number of researchers in various locales around the world. The recent work of Professor Packer on the strength and performance of certain cast steel connections has offered a novel solution to some of the complex problems associated with braced frames and the gusset plates that are the most typical for such frames. This was discussed in some detail in the "Current Steel Structures Research" paper that was published in the fourth quarter 2008 issue of the *Engineering Journal* (Bjorhovde, 2008).

Among the best known of the research work at the University of Toronto has been the extensive and long-term research efforts of Professor Packer on the strength and behavior of a great variety of connections for hollow structural sections. The results and recommendations have been adopted in numerous design specifications around the world, included in several editions of the AISC *Specification* (Packer et al., 2010).

Elliptical Hollow Structural Sections (EHSS): Studies have been under way for some time at the University of Toronto to develop member and connection characteristics for elliptical shapes. Professor Packer is the project director.

Reidar Bjorhovde, Dr.-Ing., Ph.D., P.E., Research Editor of the *Engineering Journal.* Tucson, AZ. Email: rbj@bjorhovde.com

Starting with round hollow structural sections (RHSS), square and rectangular sections (RHSS) were developed and, eventually, elliptical sections (EHSS). EHSS shapes have been produced in Europe since 1994; there is currently no producer of these sections in North America, although the material meets the 2007 requirements of ASTM A501 Grade B. Cross-sectional properties of a variety of sections have been developed, using an equivalent circular shape approach (Packer, 2009). Typical dimensions generally have major-to-minor axis ratios of 2:1.

Architecturally, the elliptical sections offer certain advantages, and originally they were used for the supporting framework for a number of glass roofs and façades. They would usually be placed such that the narrow view of the member would be visible through the glass. This was the preferred orientation for the architectural solution.

Stub column tests have shown that the failure mode of EHSS members is much more like plate buckling than cylinder buckling. Such results were used by the Toronto team to develop criteria for an equivalent RHSS rather than a CHSS cross section. Further evaluations will be made to provide improved strength data for design.

At this time, various EHSS-to-EHSS connections are being examined, through analyses and tests. An example is shown in Figure 1.

SOME CURRENT RESEARCH WORK AT THE UNIVERSITY OF WATERLOO

Steel-Precast Concrete Composite Girders with Non-conventional Shear Connectors: This project has been directed by Professors Scott Walbridge and Jeffrey West.

This project was undertaken in an effort to solve the issues associated with the use of precast deck panels for steel bridges, where the concrete deck has deteriorated sufficiently to warrant replacement, and also for certain temporary bridges. The original designs had been based on composite action; the solution required composite action between the precast panels and the steel girders. One study focused on the use of high-strength bolts as shear connectors (Iszauk and Bjorhovde, 2002); other solutions examined various other shear connection solutions (Thomann and Lebet, 2007).

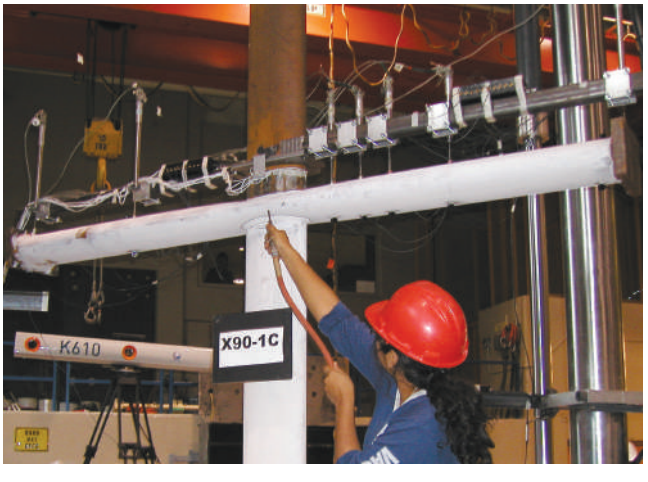

Fig. 1. Test of an elliptical HSS connection (courtesy of Professor J.A. Packer).

Two shear connection approaches were developed for the project, as follows:

1. Using post-installed shear connectors with bearing or slip-critical connections combined with various friction-enhanced surfaces (Kwon et al., 2010).
2. Using discrete stiffened bearing plates at the ends of the precast panels.

Both of these approaches were designed *not* to rely on field grouting to achieve the composite action.

For the first approach, small-scale push-out tests with various configurations of connector placement were used, along with finite element analyses. Design recommendations for this procedure are being developed. The second approach was specifically developed for various applications with remote location bridges, including varying discrete shear connector spacing and bridge dimensions. A finite element modeling procedure has been developed for this approach. Figures 2 and 3 illustrate the details of the shear connector systems.

Predicting the Effect of Post-Weld Treatment Applied under Load: This project has been directed by Professor Scott Walbridge.

Various techniques of post-weld treatment have been examined by a number of researchers, designers and fabricators with the goal of improving the fatigue life of welded bridge structures that are currently in service. One of the most important methods involves reducing the tensile residual stress that is found in the vicinity of the toe of fillet welds, or even to change this stress from tension to compression. This will reduce or arrest the growth of small fatigue cracks. The most common approach to reducing the tensile residual stress is to use peening of some sort, such as needle peening, hammer peening or ultrasonic peening.

A number of small-scale fatigue tests were run (where the specimens were first prestressed) to simulate the tensile stresses due to the dead load. The specimens were then needle peened. The propagation (depth) of the cracks was monitored by several techniques, including microhardness measurements. The results were then used to validate the assumptions used in the fracture mechanics analysis, based on linear elastic and strain-based models.

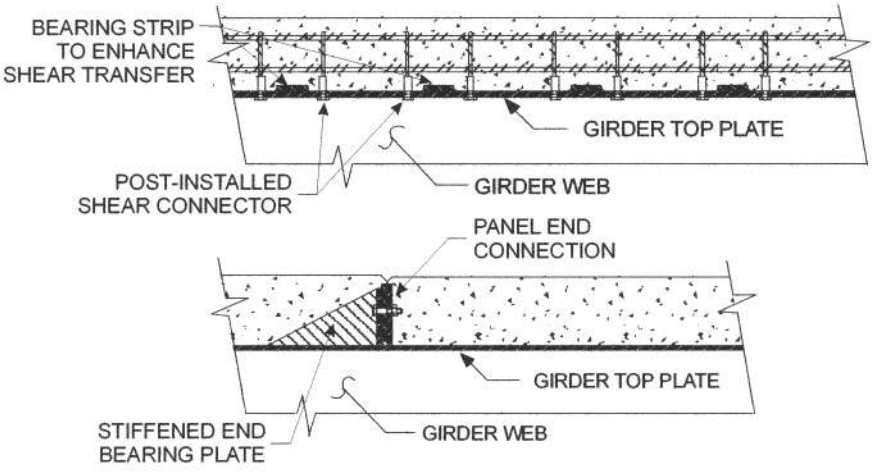

Fig. 2. Shear connection with post-installed shear connectors (top) and stiffened end bearing plate (bottom) (courtesy of Professor Scott Walbridge).

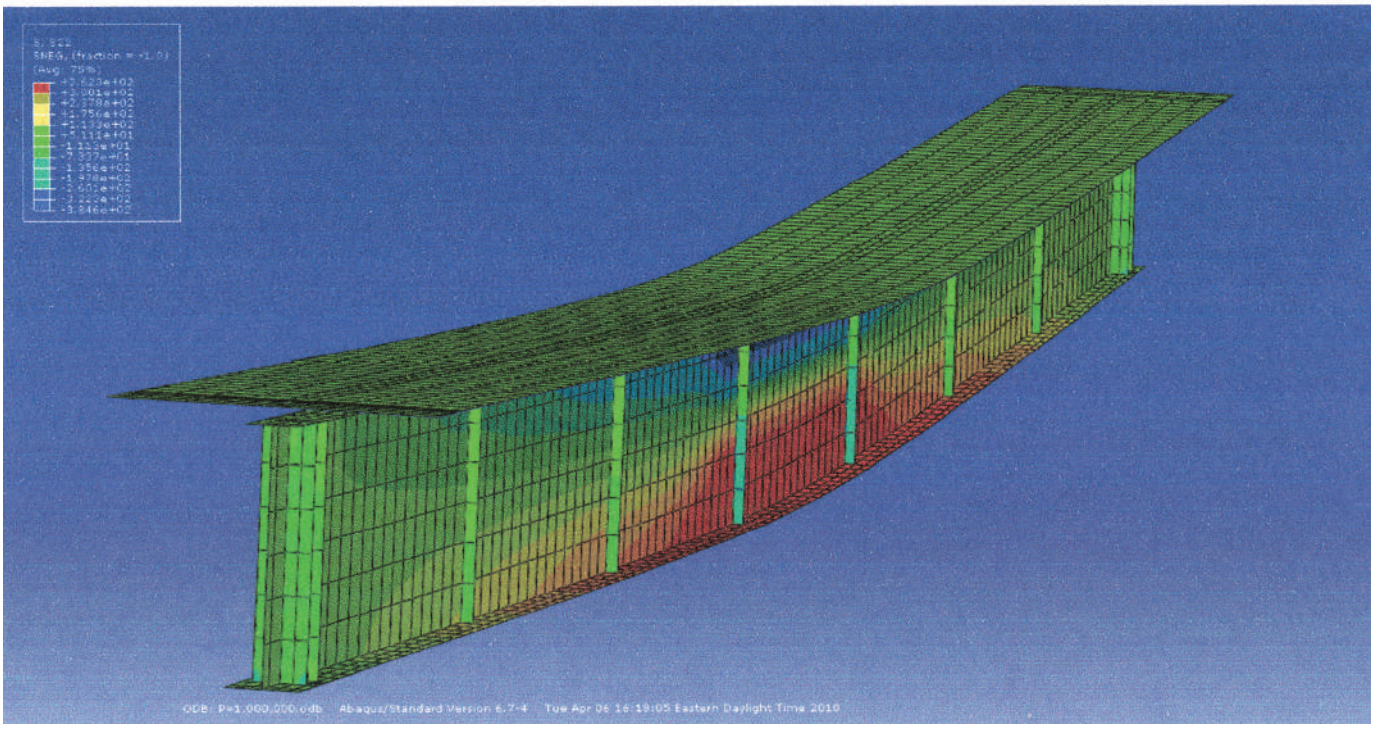

Fig. 3. Finite element stress image for girder with discrete shear connections (courtesy of Professor Scott Walbridge).

The following findings have been reported by the researchers (Ghahremani and Walbridge, 2010):

1. Needle peening can produce significant increases in the fatigue life of welds. For a given stress range, a category C detail will have a fatigue life equal to or greater than a category B detail when it has been normally peened. The fatigue life will be even larger than that of a category A detail when the peening has been applied under load.
2. Laboratory measurements of crack growth, microhardness and microstructure analysis show that the needle peening will have favorable effects up to a depth of 0.5 to 1.0 mm (0.02 to 0.04 in.) below the weld surface.
3. The fracture mechanics models provide very good data for the fatigue lives of untreated welds and treated welds for a variety of prestressing levels.

Some of the fatigue test results are illustrated in Figure 4, along with the requirements of the Canadian steel bridge design standard CSA-S6.

SOME CURRENT RESEARCH WORK AT THE UNIVERSITY OF OTTAWA

Full-Scale Testing of Gerber Frames: The project director for this study has been Professor Magdi Mohareb.

As illustrated in Figures 5 and 6, the project aims at determining the effects of the load distribution and the lateral support conditions for seven full-scale, so-called Gerber-type steel frames. This framing system is economical and very common for one-story commercial buildings in Canada. Specifically, the overhang of the roof girders (see Figure 5) is approximately 20 to 30% of the span, and the beams ("drop-in beams") for the main span are simply supported from the cantilevered overhangs (Kulak and Gilmor, 1998).

For the seven test specimens, the bracing conditions were as follows:

1. Four did not have any lateral bracing.
2. One specimen had open web steel joists at the tops of the columns as well as five uniformly spaced joists that were connected to the top flange of the beam.

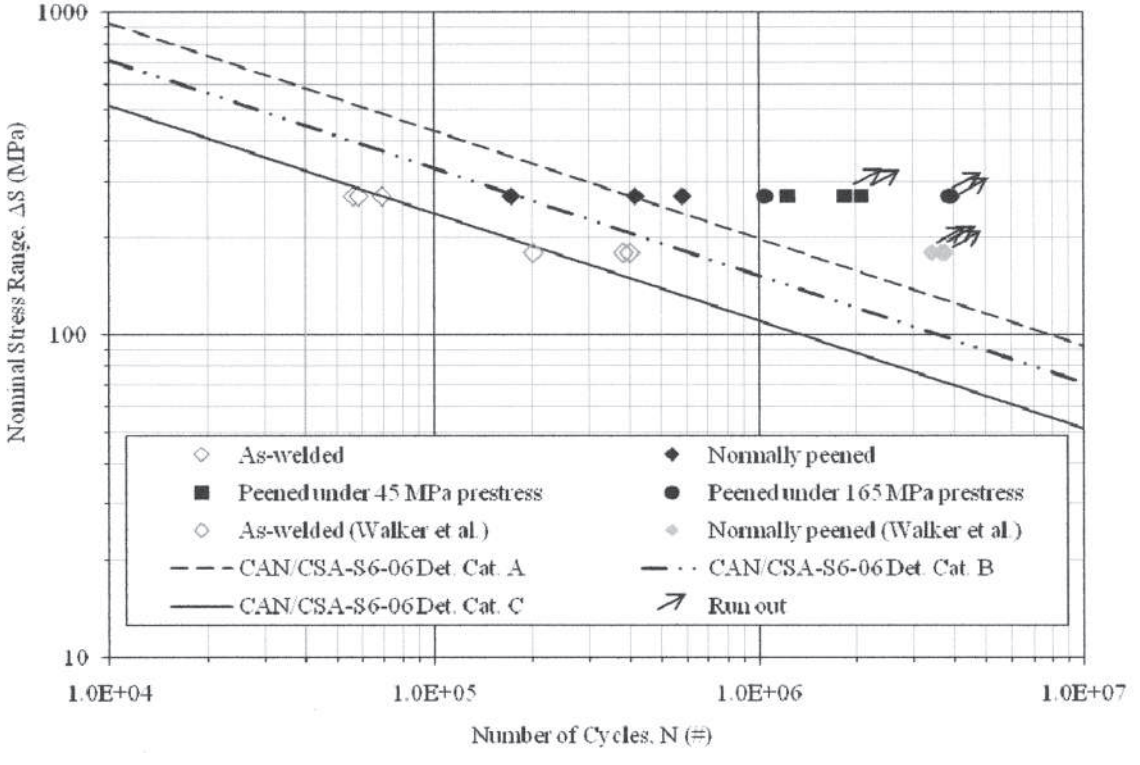

Fig. 4. Fatigue test results for peened welds and comparison with the criteria of CSA-S6 (courtesy of Professor Scott Walbridge).

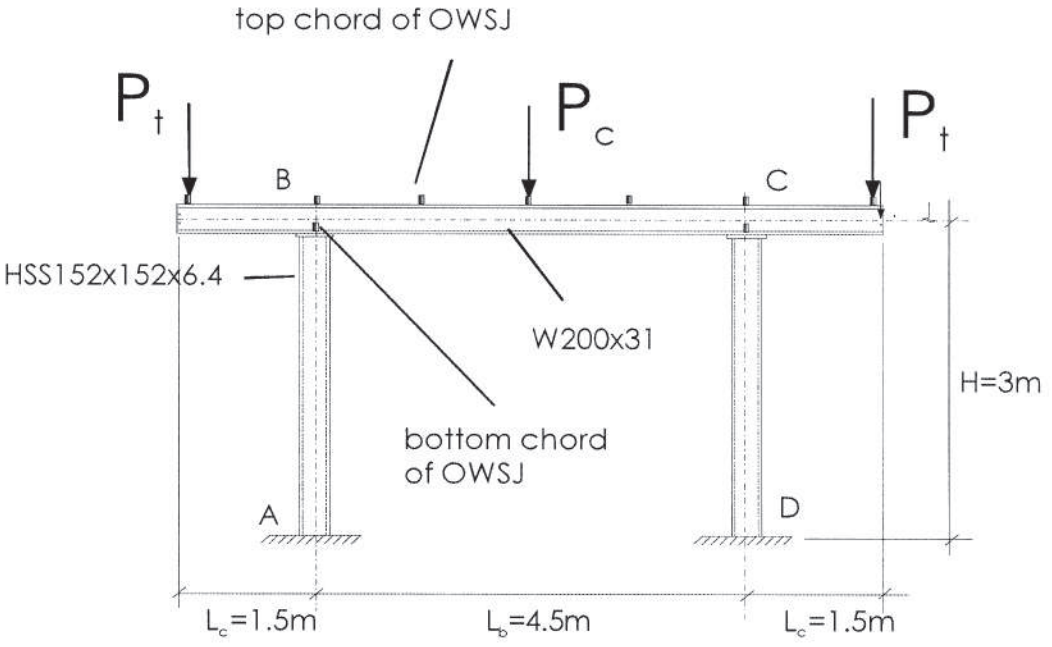

Fig. 5. Configuration of Gerber test frame specimen (courtesy of Professor Magdi Mohareb).

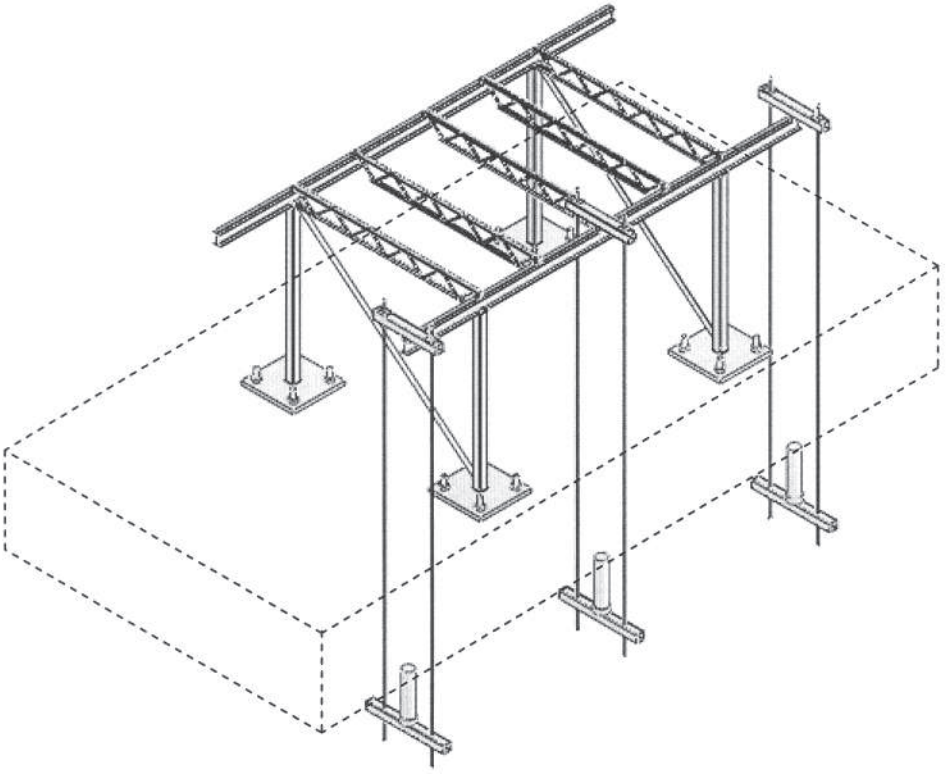

Fig. 6. Gerber test frames and load application system (courtesy of Professor Magdi Mohareb).

3. One specimen had open web steel joists at the tops of the columns (points B and C).
4. One specimen had columns laterally restrained at B and C.

The overhang tip load was P for frames 1, 2, 5, 6 and 7; 0 for frame 3; and 0.25P for frame 4. The beam midspan loads were P for all frames, except frame 2, for which it was 0.

In addition to the full-scale physical tests, finite element models were developed for the frames. At this time, six of the tests have been concluded; the test results and the predicted capacities agree to within 2 to 10%.

SOME CURRENT RESEARCH WORK AT DALHOUSIE UNIVERSITY, HALIFAX, NOVA SCOTIA

Behavior and Design of Steel Single-Angle Beam-Columns: This project has been directed by Professor Yi Liu.

In view of the fact that the current beam-column criteria for single angles is based on what was developed for doubly symmetric shapes, this study aims at providing requirements that reflect the unique characteristics of single-angle members. In particular, significant differences have been observed between tested capacities and the largely conservative strengths prescribed by the AISC and the CSA code values.

A total of 52 equal- and unequal-legged, single-angle columns were tested, using loads applied with various eccentricities. A finite element model was developed for a comprehensive parametric evaluation, taking into account practical design considerations. Following the initial evaluations, a new concept—in the form of a critical eccentricity—was developed and entered into the formulation of an improved design equation. This allowed for the determination of the various sources of the conservatism of the American and the Canadian single-angle criteria and also showed the somewhat unconservative design capacities for several cases.

Details of the proposed single-angle equation continue to be examined for eventual presentation to the specification committees. In the meantime, Figures 7a and 7b show the comparison between the finite element results and the current AISC criteria, as well as the comparison between the finite element results and the proposed single-angle equation. The horizontal axes denote the values of the normalized moment, M/M_y.

Strengthening of Steel Beams under Load: This project has been directed by Professor Yi Liu.

It is interesting to note that Professor Liu makes the observation that there is very little experimental and analytical research that addresses strengthening of beams while in service. Largely, that is correct, but there are certainly a number of important studies that deal with the subject (Nagaraja Rao and Tall, 1963; Ricker, 1988; Tide, 1990). Nevertheless, these issues are very important to designers, fabricators and contractors, and clear guidance needs to be offered. The key problems are related to the residual stresses that will be introduced during the strengthening operation, as well as the preload from the service operations of the structure.

The experimental segment of the research project used nine steel W12×19 beams with three types of reinforcing plates, as shown in Figure 8. The shapes were tested in flexure, while the reinforcing plates were welded to the beam at different preload levels. Three strengthening patterns and two beam lengths were used, and the residual stress distributions for each were measured. A numerical model was also developed. It was found that strengthening under load had a significant effect on beams that failed in lateral-torsional

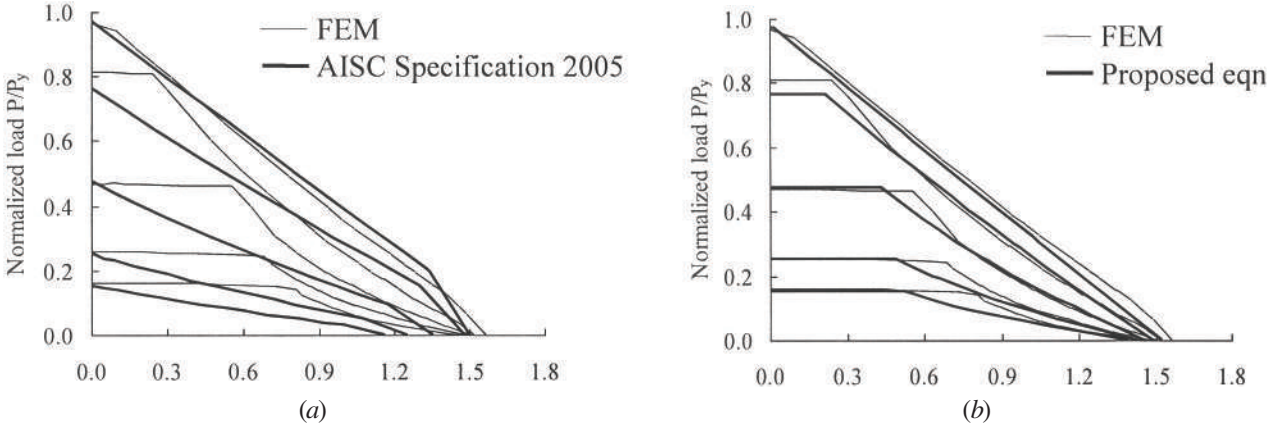

Fig. 7. Comparison of finite element predictions and the capacities predicted by (a) the AISC Specification *(2005) and (b) the proposed single-angle equation (courtesy of Professor Yi Liu).*

buckling. The effects can be offset by providing lateral restraints along the length of the beam, reducing the detrimental effect of the welding residual stress and the distortion that often accompanies the welding under such conditions.

SOME CURRENT RESEARCH WORK AT CARLETON UNIVERSITY, OTTAWA, ONTARIO

Structural Performance of HSS Steel Frame Assemblies with Moment Connections in Fire: This project has been directed by Professor G. Hadjisophocleous.

Recognizing the increasing use of hollow structural sections for columns and even beams in steel structures, the project aims to test a total of 10 beam-to-column connections in the new fire test laboratory of Carleton University. For several reasons, it was decided to use end-plate connections for the test specimens, examining the influence of the thickness of the end plate, the degree of axial restraint of the beam and the beam cross-sectional properties. Further, an extended end-plate connection that is expected to perform better under elevated temperatures will also be tested.

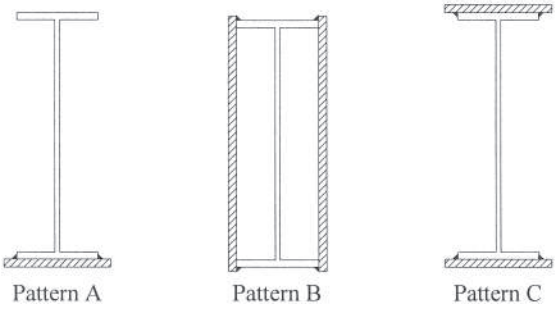

Fig. 8. Placement of reinforcing plates for W*12 × 19 beams to be tested under load (courtesy of Professor Yi Liu).*

Figure 9 shows the appearance of two of the connections after the fire test. As expected, the one with the thinner (½ in.) end plate responds significantly different than the one with the thicker (¾ in.) end plate. Specifically, for the thinner case the rotations are largely provided by the deformations of the plate. For the connection with the thicker end plate, the deformations are provided through deformations of the column, where it appears that a plastic hinge has formed. This may not be advantageous for the overall response of the structure, but the issues continue to be studied.

REFERENCES

Birkemoe, P.C. and Gilmor, M.I. (1978), "Behavior of Bearing-Critical Double-Angle Beam Connections," *Engineering Journal*, AISC, Vol. 15, 4th Quarter, pp. 109–115.

Bjorhovde, R. (2008), "Current Steel Structures Research," *Engineering Journal*, AISC, Vol. 45, 4th Quarter, pp. 287–292.

Bjorhovde, R. (2010), "Current Steel Structures Research," *Engineering Journal*, AISC, Vol. 47, 2nd Quarter, pp. 123–130.

Ghahremani, K. and Walbridge, S. (2010), "Predicting the Effect of Peening Treatments Applied under Load on the Fatigue Performance of Welds in Existing Steel Bridges," *Proceedings, 8th International Conference on Short and Medium Span Bridges*, Niagara Falls, Canada.

Iszauk, S.I. and Bjorhovde, R. (2002), "High Strength Bolts as Shear Connectors: Composite Steel Girders with Precast Bridge Deck," *Proceedings, FHWA Steel Bridge Conference*, Salt Lake City, UT, December 13–15.

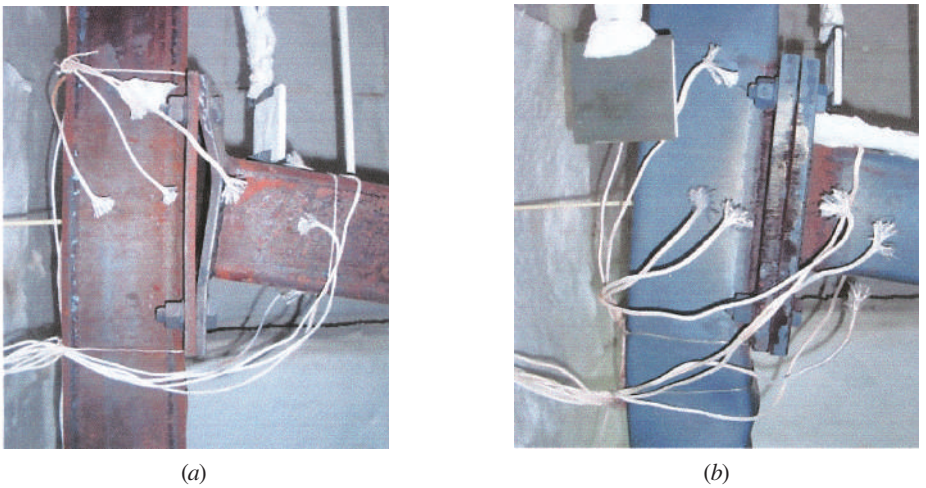

(*a*) (*b*)

*Fig. 9. Deformations of two HSS end-plate beam-to-column connections after fire tests: (a) test 1 end plate (*t = ½ *in.); (b) test 2 end plate (*t = ¾ *in.) (courtesy of Professor G. Hadjisophocleous).*

Kulak, G.L. and Gilmor, M.I. (1998), *Limit States Design in Structural Steel*, 6th ed., Canadian Institute of Steel Construction, Toronto, ON, Canada.

Kwon, G., Engelhardt, M.D. and Klingner, R.E. (2010), "Behavior of Post-Installed Shear Connectors under Static and Fatigue Loading," *Journal of Constructional Steel Research*, Vol. 66, No. 4, pp. 532–541.

Nagaraja Rao, N.R. and Tall, L. (1963), "Columns Reinforced under Load," *Welding Journal*, Vol. 42, April, p. 177-s.

Packer, J.A. (2009), "Elliptical Sections—Part Two: EHS Member Design," *Advantage Steel*, Canadian Institute of Steel Construction, Toronto, ON, Canada.

Packer, J.A., Sherman, D.R. and Lecce, M. (2010), *Design Guide No. 24, Hollow Structural Section Connections*, American Institute of Steel Construction, Chicago, IL.

Ricker, D.T. (1988), "Field Welding to Existing Steel Structures," *Engineering Journal,* AISC, Vol. 25, No. 1, pp. 1–16.

Tide, R.H.R. (1990), "Reinforcing Steel Members and the Effects of Welding," *Engineering Journal,* AISC, Vol. 27, No. 4, pp. 129–131.

Thomann, M. and Lebet, J.-P. (2007), "Design Methods for Connections by Adherence for Steel-Concrete Composite Bridges," *Structural Engineering International*, Vol. 1, pp. 86–93.

ACKNOWLEDGMENTS

Significant special assistance has been provided by ISSRA member David MacKinnon of the Steel Structures Education Foundation of Canada.